DEVELOPMENT OF MATHEMATICAL MODEL-ASSISTED MICRO/NANO-HIERARCHICAL STRUCTURES ON ETFE FILMS FOR SELF-CLEANING APPLICATION

A thesis submitted to the
UPES

For the award of
Doctor of Philosophy
in
Physics

BY
Jaishree

May 2025

SUPERVISOR
Dr. Manjeet Singh Goyat
Dr. Anupam Bhandari

School of Advanced Engineering
UPES
Dehradun-248007: Uttarakhand

DEVELOPMENT OF MATHEMATICAL MODEL-ASSISTED MICRO/NANO-HIERARCHICAL STRUCTURES ON ETFE FILMS FOR SELF-CLEANING APPLICATION

A Thesis Submitted to the
UPES

For the award of
Doctor of Philosophy
in
Physics
BY

Jaishree
(SAP ID: 500095526)
May 2025

Supervisor (s)
Dr. Manjeet Singh Goyat
Sr. Associate Professor
School of Advanced Engineering

Dr. Anupam Bhandari
Sr. Associate Professor
School of Advanced Engineering

Department of Applied Sciences (Physics)
School of Advanced Engineering
Dehradun-248007: Uttarakhand

DECLARATION

I declare that the thesis entitled **“Development of Mathematical Model-Assisted Micro/Nano-Hierarchical Structures on ETFE Films for Self-Cleaning Application”** has been prepared by me under the guidance of Dr. Manjeet Singh Goyat, Sr. Associate Professor of Physics and Dr. Anupam Bhandari, Sr. Associate Professor of Mathematics, UPES, Dehradun. No part of this thesis has formed the basis for the award of any degree or fellowship.

Jaishree Sharma
Junior Research Fellow
Department of Physics (Applied Science Cluster)
UPES - Energy Acres, Bidholi, Dehradun-248007,
Uttarakhand, India

Date: 7th October 2024

UPES
UNIVERSITY OF TOMORROW

Great Place To Work® Certified
FEB 2024-FEB 2025
INDIA

CERTIFICATE

I certify that Jaishree has prepared her thesis entitled **"Development of Mathematical Model-Assisted Micro/Nano-Hierarchical Structures on ETFE Films for Self-Cleaning Application"**, for the award of PhD degree of the UPES, under my guidance. She has carried out the work at the Department of Physics, UPES.

Internal Supervisor (s)

Dr. Manjeet Singh Goyat

Research Supervisor

Department of Physics

Dr. Anupam Bhandari

Research Co-supervisor

Department of Mathematics

School of Advanced Engineering

UPES - Energy Acres, Bidholi, Dehradun-248007,

Uttarakhand, India

Date: 7th October 2024

This dissertation is dedicated to my parents,

Mr. Surender Kumar and Mrs. Rajesh Kumari,

my husband Mr. Rahul Kaushik,

and my lovely niece Aaradhya Sharma.

ABSTRACT

Superhydrophobic surfaces, renowned for their water-repellent and self-cleaning properties, have gained widespread interest across various industries. These surfaces replicate micro- and nano-hierarchical structures found in nature, such as the lotus effect, to achieve superior water resistance. Their fabrication involves modifying surface chemistry and roughness through techniques like chemical etching, lithography, and deposition, often combined with low-energy coatings or functional groups. However, challenges such as durability, scalability, and cost remain key barriers to practical applications. Surface wettability is evaluated using Water Contact Angle (WCA) measurements, where higher angles indicate rougher surfaces and enhanced hydrophobicity. Despite advancements, a comprehensive theoretical model linking surface structures to contact angles is lacking. The existing Young's, Wenzel's, and Cassie–Baxter's wetting models require further refinement to improve predictions of non-wetting behavior. Developing precise mathematical models and scalable fabrication techniques is essential to overcoming these limitations. Mechanical engineering methods enable the direct creation of microstructures, enhancing surface durability without additional materials. In advanced materials research, self-cleaning properties are particularly valuable in aerospace, architecture, and optical applications. Ethylene tetrafluoroethylene (ETFE) films have emerged as promising candidates due to their optical transparency, mechanical strength, and chemical resistance. Using a single-point diamond turning technique, we fabricated a micro-textured ETFE surface that achieved a WCA of 141.2°, demonstrating excellent self-cleaning performance. This enhanced surface surpassed bare ETFE in maintaining cleanliness, making it suitable for architectural coatings, solar panels, and other outdoor applications.

This study focuses on the design and optimization of micro/nanostructures to enhance water repellency. A force-balanced mathematical model was developed to optimize rectangular pillared structures, considering surface roughness, contact angle, and droplet behavior. Experimental validation involved fabricating and characterizing micro-structures, where a rectangular pillared pattern was created on aluminum (Al) using a diamond turning machine. The model, supported by MATLAB simulations, predicted a WCA of 136.6°, whereas experimental results averaged 123.7° ± 3°, with deviations attributed to machining variables such as feed rate and cutting depth. Fabricated surfaces were analyzed using FESEM, CIC, and contact angle measurements to assess morphology and wettability. This research introduces a structured approach for developing self-cleaning surfaces, with the mathematical model serving as a predictive tool for optimizing hydrophobicity. The findings provide practical insights for engineering coatings, textiles, and optical devices, contributing to the advancement of surface science and durable self-cleaning technologies.

ACKNOWLEDGEMENTS

I am grateful to my supervisors, Dr. Manjeet Singh Goyat from the Department of Physics and Dr. Anupam Bhandari from the Department of Mathematics at the UPES, Dehradun, for their invaluable guidance, unwavering support, and constant encouragement throughout the entire research process. Their expertise, patience, and insightful feedback were crucial in shaping this thesis.

I also extend my gratitude to Dr. D.K. Avasthi, Dean R&D, and Dr. Pankaj Thakur, Associate Dean, R&D, who generously shared their knowledge and resources, enhancing the quality of this study. Their contributions significantly expanded the depth and breadth of my research. I would like to express my appreciation to Mr. Charu Pant, Senior Lab Superintendent, Central Instrumentation Centre, for his full assistance.

I am deeply thankful to Dr. Neha Khatri, a Principal Scientist at CSIO-CSIR, Chandigarh, for her help with the experimental work. Her moral support and collaboration have significantly enriched the outcomes of this study.

I am indebted to my father, Mr. Surender Kumar, and my mother, Mrs. Rajesh Kumari, for their unwavering love, encouragement, and understanding during this journey. Their patience and support have been my pillar of strength. I am especially grateful to my fiancé, Mr. Rahul Kaushik, for his constant encouragement and motivation. His constant moral support has made this journey more enjoyable and fulfilling.

Lastly, I would like to thank IIT Roorkee for providing characterization facilities,

Dated: 7th October 2024 **Jaishree**

TABLE OF CONTENTS

LIST OF FIGURES

LIST OF TABLES

LIST OF SYMBOLS

θ (°)	The angle between the centre point of the water droplet and the tangential point

l (μm)	Length of rectangular pillars
b (μm)	Width of rectangular pillars
p (μm)	Gap between pillars
rpm	Revolution per minute
rev	revolution
D	dimensional
ρ *(kg/m^3)*	Water density
g (m/s^2)	Acceleration due to gravity
r (mm)	The radius of the circle formed by water droplet
T (N/m)	Water surface tension
H (mm)	Total height of the drop
h (mm)	The distance measured perpendicularly from the drop's centre to its flat bottom contact line
y (mm)	The vertical height of the drop's highest point relative to its horizontal centre.
R_0 *(mm)*	The radius of the spherical drop
R_1 *(mm)*	The radius of the drop's projected contact circle with the surface
V (mm)	Drop height
φ	The angle formed by the tangent of the droop and the normal to the rectangular pillar

mm	Millimetre
nm	Nanometre
μm	micrometre
θ_{eq}	equilibrium contact angle in Young's model
γ_{SL}	interface surface tensions of solid–liquid
γ_{LV}	interface surface tensions of liquid–gas
γ_{SV}	interface surface tensions of solid–gas
θ_W	Wenzel contact angle
r_f	roughness factor
θ_{CB}	contact angle of the Cassie–Baxter model
F_S	interaction between the solid fraction and liquid droplet
θ_Y	Young's contact angle
$2R$	depth of the scratch
D	diameter of the abrasive particle
λ	distance between two consecutive scratches
R_{f-w}	Wenzel roughness factor
a	depth of scratches
R_{f-CB}	Cassie-Baxter roughness factor
L	Length of the scratches

B_0	Bond number
θ^*	static contact angle for a fixed volume
G	Gibbs free energy
ρ^*	Liquid density
V^*	Volume of liquid drop
d_s	superhydrophilic spot diameter
S	oblate spheroid droplet's surface area
H	oblate spheroid droplet's centroid
R	Radius of curvature
a^*	Half-width of micro-structure
b^*	Height of micro-structure
A_c	drop's cap area
A_p	drop's projection area
a_1	Cylinder top diameter
h_1	Cylinder pillar hight
L_1	Distance between the pillars
F	Potential drop radius
γ'	Surface tension of drop
f_w'	the projection area fraction of the wetted surface

r_f'	ratio of the roughness
φ'	ratio of the solid–liquid area to the projection area
θ_E'	equilibrium contact angle
E_{ac}	acoustic wave energy
ω	vibration frequency
A	Amplitude
E_b	Energy barrier
R_c^2	drop contact line radius
x	Diameter of particle
θ_g	geometric radius contact angle
S	2D volume of the droplet
S^*	dimensionless 2D volume of the droplet
q	Drop base radius
$R*$	dimensionless radius of the cylindrical drop
α^1	interfacial liquid–air space in the grooves
A^1	2D interfacial area
sl	Solid-liquid interface
L	Liquid-air interface
s	Solid- air interface

σ	Interfacial tension

LIST OF ABBREVIATIONS

3D	Three dimensional
AAO	Anodic aluminium oxide
AFM	Atomic force microscopy
Al	Aluminium
Ar	Argon
CAB	Cellulose acetate butyrate
CAGR	Compound annual growth rate
CAH	Contact angle hysteresis
CCI	Coherence correlation interferometry
CF_4	Tetrafluoromethane
COC	Cyclo-olefin copolymer
COP	Cyclo-olefin polymer
CVD	Chemical vapour deposition
DSA	Drop shape analyser
DOE	Diffractive optical element
ECTFE	Ethylene chlorotrifluoroethylene
ETFE	Ethylene tetrafluoroethylene

FAS	Fluorinated alkyl silane
FESEM	Field emission electron microscope
FEP	Fluorinated ethylene propylene
FTIR	Fourier transform infrared spectroscopy
HDPE	High-density polyethylene
HE	Hot embossing
HNL	Hierarchical nanoporous layer
IDT	Inter digitated transducer
LDPE	Low-density polyethylene
$LiNbO_3$	Lithium niobate
MEMS	Micro electromechanics
Ni	Nickel
PA	Polyamide
PAI	Polyamide-imide
PBI	Polybenzimidazole
PC	Polycarbonate
PCE	Power conversion efficiency
PCTFE	Polychlorotrifluoroethylene
PE	Polyethylene

PEEK	Polyether-ether ketone
PET	Polyethylene terephthalate
PI	Polyimide
PLA	Polylactic acid
PMMA	Polymethyl-methacrylate
POM	Polyoxymethylene
PP	Polypropylene
PS	Polystyrene
PTFE	Polytetrafluoroethylene
PU	Polyurethane
PUA	Polyurethane-acrylate
PV	Photovoltaic
PVDF	Polyvinylidene fluoride
PVC	Polyvinylchloride
R2P	Roll-to-plate
R2R	Roll-to-roll
SEM	Scanning electron microscope
SHC	Superhydrophobic coating
SHS	Superhydrophobic surface

Si	Silicon
Sio$_2$	Silicon dioxide
SPDT	Single point diamond turning
SS	Stainless steel
TiO_2	Titanium dioxide
TIPS	Thermally induced phase separation
TPU	Thermoplastic polyurethane
UK	United Kingdom
UV	Ultraviolet
WCA	Water contact angle
WEDM	Wire electrical discharge machining
XRD	X-ray diffraction

CHAPTER 1. INTRODUCTION

1.1. BACKGROUND

Renewable resources such as solar energy are gaining significant attention due to their minimal ecological impact. Solar energy is a reliable backup energy source and a sustainable approach to reducing carbon emissions from electricity generation. However, concerns have been raised regarding the performance degradation of solar panels under various conditions such as bad climatic conditions, soiling, and ultraviolet (UV) radiation exposure. To overcome such issues, European countries have already adopted ethylene tetrafluoroethylene (ETFE) coverings for solar panels as an alternative to glass coverings. ETFE coverings offer several advantages over glass, such as light weight, scratch-proof, optically more transparent, and possessing high tensile strength. However, still there is a scope to improve the performance of ETFE as such surfaces possess only partial self-cleaning properties with a maximum water contact angle of around 110°. However, both chemical and physical routes are available to convert hydrophobic surface to the superhydrophobic surface, but physical routes are more advantageous to modify the surface of ETFE without sacrificing its other important inherent properties. The transition of ETFE from hydrophobic to superhydrophobic surface can improve its self-cleaning properties. This will lead to enhanced power conversion efficiency (PCE) of the solar panels. Thus, the superhydrophobic, self-cleaning ETFE coverings for solar panels holds great potential for improving the performance and longevity of solar panels, reducing maintenance efforts, and facilitating the broader adoption of solar energy as a sustainable and clean power source.

1.2. STATEMENT OF THE PROBLEM

Advances in the fabrication of highly hydrophobic/superhydrophobic surfaces have been significant, as they involve the replication of hierarchical patterns using two main elements: materials with low surface energy and appropriate micro- and nanoscale structures. However, the durability of these surfaces poses a significant challenge for real-world applications, as those with low mechanical stability often underperform in practical settings. Optical industries have limited practical applications of self-cleaning surfaces due to the difficulty of achieving surface roughness and transparency simultaneously. Factors such as high cost, fragility, mechanical durability, and challenges in large-scale production contribute to the limited adoption of superhydrophobic surfaces. Moreover, the understanding of wetting behaviors on surfaces is limited, which complicates the fabrication of superhydrophobic surfaces. To overcome this challenge, the development of a mathematical model to optimize geometric patterns for enhanced surface wettability is necessary. This model will guide the design of large-scale arrayed micro-feature-based superhydrophobic surfaces, taking into account various geometric parameters. In the context of energy applications, conventional solar panels covered with glass experience efficiency losses due to dust accumulation and soiling. To maximize solar radiation transmission and enhance efficiency, solar panels require optical transparency. The worldwide solar power market is projected to reach a valuation of USD 3 billion by 2030, with a CAGR of around 7.89 percent during (2021-2031). Therefore, efforts are being made to enhance the efficiency of solar panels, and self-cleaning covers are being developed, which will undoubtedly benefit the environment. The development of superhydrophobic, self-cleaning ETFE coverings for solar panels has significant implications for the widespread adoption of solar energy. By addressing the performance limitations of solar panels, particularly in challenging environmental conditions, this research advances sustainable energy technologies and supports the transition toward a cleaner and more resilient energy landscape.

1.3.MOTIVATION FOR THE RESEARCH

The pursuit of developing self-cleaning surfaces has been a longstanding objective in the field of engineering and materials science. The aim is to develop more efficient and sustainable technologies. Among the various materials being investigated for self-cleaning applications, Ethylene Tetrafluoroethylene (ETFE) stands out due to its exceptional combination of properties, including high transparency, mechanical durability, and chemical resistance. ETFE is commercially available. It is expected that by 2028, the global market of the ETFE industry will touch on the valuation of USD 8 billion, and CAGR is expected to be around 7.89 percent during (2021-2027). It is cost-effective, recyclable, and long-lasting holding up to extreme climatic conditions. Flexibility, stain resistance, light weight, anti-aging ability, and other benefits of ETFE make it ideal to use in architectural membranes, photovoltaic modules, and biomedical devices. Traditional cleaning methods, such as manual washing or chemical treatments, are often labour-intensive, environmentally unfriendly, and economically costly. In recent years, micro/nano-hierarchical structures have emerged as promising candidates for imparting self-cleaning properties to surfaces. However, designing and optimizing these hierarchical structures pose significant challenges, requiring a comprehensive understanding of the underlying physical mechanisms governing wetting, adhesion, and surface interactions at the micro- and nanoscale. Mathematical modelling offers a powerful tool for solving these complex phenomena, enabling the systematic exploration of structure-property relationships and the design of novel surface architectures with tailored self-cleaning functionalities. This thesis aims to contribute to the development of mathematical models for predicting the wetting behavior and self-cleaning performance of micro/nano hierarchical structures on ETFE films. By combining theoretical analyses with experimental validation, the proposed models seek to provide insights into the key parameters influencing surface wettability and liquid adhesion. This thesis endeavours to bridge the gap between fundamental research and practical implementation, offering innovative solutions to real-world challenges.

1.4. OBJECTIVES

- To improve understanding of commercial polymer (ETFE) films for self-cleaning applications.
- To validate the new understanding by optimization of the geometrical patterns.
- To contribute in designing better hydrophobic surfaces on arrayed micro-features based on geometrical parameters.

1.5. SCHEME OF THE CHAPTERS

The chapter-wise summary of the thesis is given below:

Chapter 1 introduces the problem statement, background information, explains the motivations and necessity of the research objectives, and delineates the layout of the subsequent chapters, which focuses on the fabrication of hierarchical structures and the validation of these structures through wetting models.

Chapter 2 presents a comprehensive review of hot embossed superhydrophobic surfaces, including their development history, current advancements in polymer-based superhydrophobic surfaces, the mechanical and thermal durability of superhydrophobic surfaces, the advantages and limitations of the hot embossing technique, and its various applications and current challenges, along with future recommendations.

Chapter 3 provides an extensive literature review on the translational wetting behaviors of superhydrophobic surfaces, including the fundamental principles of theoretical wetting models, experimental and theoretical validation of superhydrophobic surfaces, and the discrepancies in transitional wetting regimes that involve the dynamics of droplet bouncing, kinetics, and the size of water droplets.

Chapter 4 provides the fabrication process of microstructures using single point diamond turning (SPDT) machining. It also includes comprehensive information on the materials used. Additionally, this chapter describes the characterization techniques employed to obtain data from the fabricated microstructures, including Field Emission Scanning Electron Microscopy (FESEM), Dynamic Scanning Analysis (DSA), Fourier Transform Infrared Spectroscopy (FTIR), and Coherence Correlation Interferometry (CCI).

Chapter 5 provides an in-depth description of the fabrication process for micro rectangular pillared arrayed surfaces using single point diamond turning machining. The mathematical model for this process was developed using the force balance equation system in MATLAB. The materials used for creating hydrophobic surfaces are also discussed in detail. The differences between theoretical and experimental findings are thoroughly examined. Additionally, characterization techniques such as CCI, FESEM, and DSA were employed. This chapter showcases how a single-step texturing process on aluminium can result in a WCA of 123.7° with a high-quality mirror finish.

Chapter 6 delves into the mechanical engineering methods used to create microstructures on the ETFE surface. Single point diamond turning machining was utilized to produce the smooth surface finish micro-structures. Prior to single-step texturing, the bare and micro-structured ETFE surface displayed water contact angles of 85.6°, while after texturing, the contact angle increased to 141°. These modified surfaces hold great promise for diverse industrial applications where self-cleaning properties are highly desirable.

Chapter 7 summarizes the results and prospective possibilities to fabricate better hydrophobic surfaces, as well as the verification of experimental and theoretical research through mathematical modelling.

CHAPTER 2. LITERATURE SURVEY: EXPERIMENTAL ASPECTS

2.1. THEORY OF SUPERHYDROPHOBIC SURFACES

Superhydrophobic coatings (SHCs) due to their self-cleaning characteristics are well known to society and industry. These coatings are used in multiple sectors including marines, automotive, optical devices, textiles, membranes for oil-water separation, drag reduction in microfluidics, sensors, energy sector, anti-corrosion coatings, batteries, anti-fouling coatings, and many more [1-4]. Superhydrophobic surfaces (SHSs) exhibit a high-water contact angle (WCA) of more than 150° and a contact angle hysteresis (CAH) of less than 10° (also known as roll-off angle and tilt angle) [5-8]. The idea of superhydrophobicity originated from the leaf of the lotus plant. The morphology of a lotus leaf has an inherent hierarchical structure with double-scale roughness. Lotus leaves exhibit an SHS, which is due to specific microstructures consisting of epicuticular wax [9-10]. Several researchers have identified wax as the formulation component of the self-cleaning surface [11]. Because the air trapped in between the two states of matter, that is, solid and liquid interfaces reduce the solid-liquid interaction in the lotus leaf, where the water adhesion is extremely low [12]. No water droplets adhere to the leaf's surface or wet it. Owing to this effect, the surface of the lotus leaf remains dry and clean all the time. The same is true for more viscous liquids like honey. This is related to the existence of micro-protrusions on hydrophobic coatings [13] (Fig. 2.1). This combination gives a rough surface that exhibits perfect water-repellent and self-cleaning properties as dirt particle tends to stick to the water molecule as it drops off the surface. These surfaces would have high WCA because of the low surface energy of the leaf, which leads to the formation of a spherical shape of a water droplet. This minimizes the area of contact between the leaf and the water droplet and eventually results in high contact angle. This effect is commonly known as the ‘lotus effect’ [14]. Inspired by the natural biological SHSs, which exhibit very good self-cleaning properties, artificial SHSs have been designed for real-life applications. Superhydrophobicity is the result of the combination of hierarchical low surface energy and micro-nano-sized level surface roughness of a solid substrate. However, for practical applications, long-lasting SHCs are challenging to deploy in industries because of their poor durability and weak mechanical properties.

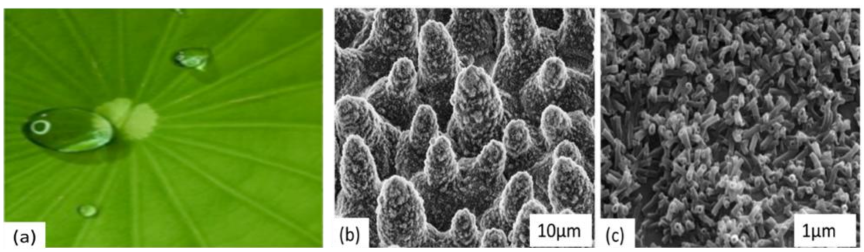

Fig. 2.1. (a) Digital camera image of a typical lotus leaf, (b) lotus leaf's microstructure, and (c) lotus leaf's nanostructures (scale bar (b and c): 10 and 1 mm). (Reprinted with permission from Ref. [13], Bielstein Journal of Nanotechnology, Copyright © 2011 Ensikat et al).

Different surface structural factors of a substrate may result in different wetting states. The wetting states are explained in past using various WCA prediction models. Young's equation was the first wetting model developed in 1805 to describe the wettability of smooth surfaces, as the surface con tact angle is the most important measure of surface hydrophobicity [15]. Later, various approaches were followed to balance the surface roughness and superhydrophobicity simultaneously. However, till date, there is no universal wetting model exists that can completely correlate the physical properties and surface wettability of a solid surface. The development of theoretical wetting models [16] with time is shown in Fig. 2.2. Surface wettability can be determined by the surface tension and viscosity [17]. The Cassie-Baxter model and the Wenzel model are two fundamental models for defining the conditions of a water droplet on rough surfaces. The Cassie-Baxter model describes heterogeneous wetting, while the Wenzel model describes homogeneous contact between the droplet and the rough surface [18]. The steady and transient behavior of a droplet of liquid on a surface is used to determine wettability [19]. Because single scale roughness has some limitations when predicting super hydrophobicity, so to improve the contact area between liquid and air, dual-scale surface roughness is beneficial [20,21]. Therefore, it is desirable to develop a theoretical model based on different geometrical parameters to describe the wetting behavior of the surface completely.

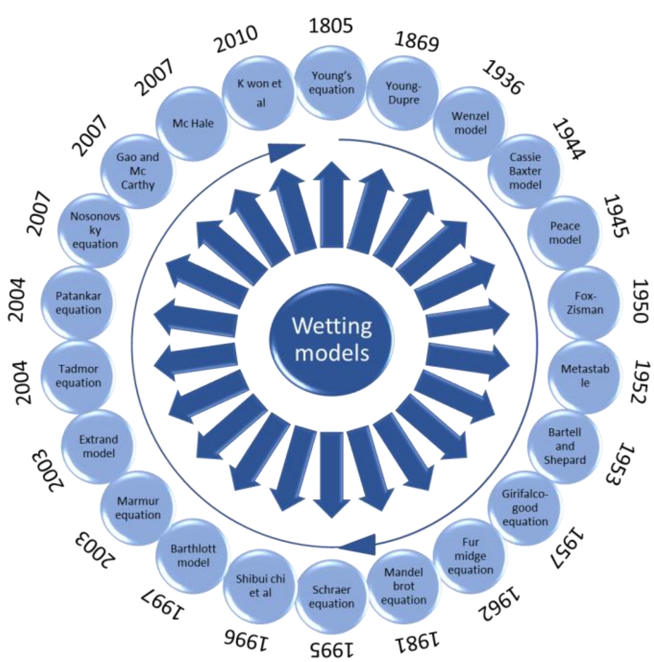

Fig. 2.2. Timeline of key developments of wetting models from 1805 to 2010. (Reproduced with permission from Ref. [16], The Journal of Physical Chemistry B, Copyright © 2020 American Chemical Society).

Furthermore, the surface texturing via micro and nano manufacturing procedures has gained a lot of interest in creating artificial SHSs of better quality [22]. Therefore, there is a great scope for fabricating artificial SHSs [23]. In general, the fabrication of an SHS is governed by two main parameters such as (1) the creation of rough nano hierarchical structure on a hydrophobic substrate or (2) treating the substrate with a low surface energy material [24,25]. A variety of techniques can be used to produce artificial SHSs like diffusive photolithography, colloidal lithography-plasma texturing, reactive-ion etching, laser ablation, and dry anisotropic etching [26,27]. Most of the processes either involve a large number of steps that makes them slow or limited to small-size samples that makes them expensive and prone to error. Additionally, limited techniques are suitable for creating patterns on polymeric substrates. However, the hot embossing (HE) technique can overcome all the abovementioned problems because it is the most promising industrial scalable process [28] to replicate the micron-scale structures on a polymer substrate. It is a low-cost and relatively fast replication method for creating high-quality micropatterns with excellent reproduction ability. HE is a relatively rapid process and hence shows great potential for industrial processes [29,30]. The HE has tremendous applications in various fields such as holography, thin film solar cells, biochips, nanophotonic metamaterials, optical waveguides, organic light-emitting diodes, microfluidics, as well as others [31,32]. Polycarbonate (PC), cyclic olefin copolymer (COC) [33], polymethyl methacrylate (PMMA), and ethylene tetrafluoro ethylene (ETFE) are the most commonly utilized thermoplastics for HE. However, there are hardly any reports available in the literature on the challenges of HE as many challenges exists in developing complex three-dimensional (3D) structures such as removing the tool that may damage micro-nano level features at high temperatures. Patterned structures can be developed on a polymer substrate by optimizing the temperature and pressure of the HE technique. Such structured polymers have much-desired applications in micro-fluid chips for drug delivery or protein crystallization, optics (films for photovoltaic (PV) arrays), micro electro mechanics (MEMs), etc. In this review article, we are addressing the recent progress in the development of SHCs by HE technique. Additionally, the current challenges and possible advancements, as well as the creation and implementation of the HE technology, are also examined. In this article, various kinds of micro-nano-aided hierarchical structures that provide the best WCA have been covered. Additional applications of polymeric SHSs are covered, such as optical instruments, where clear vision is very important. Because achieving the perfect balance between transparent surfaces and superhydrophobicity is still a challenging task.

2.2. Various approaches to the fabrication of superhydrophobic surfaces

Over the past few years, SHSs have been developed using a variety of metal components, polymeric materials, silane pre cursors, siloxane-based materials, and other substances, such as glass, nanofibers, silica wafers, membranes, papers, textile fabrics, sponges, foams, and aerogels [34-36]. Because of the time consuming and costly production procedures, the SHSs are limited to small-scale use [37]. Both the 'bottom-up' and 'top down' approaches [38] are useful in the production of topographical structures on SHSs as depicted in Fig. 2.3.

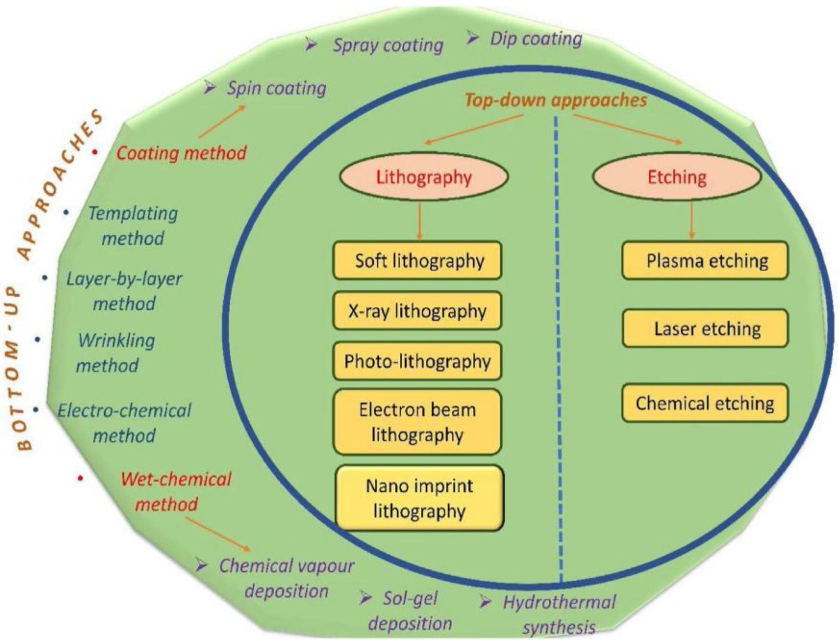

Fig. 2.3. Schematic drawing of top-down and bottom-up approaches for creation of SHSs.

To construct hierarchical designs, top-down approaches are excellent in controlling the air fraction at nanoscales. SHSs with a WCA nearabout 180^0 can be generated even from hydrophilic materials if a nanoscale surface with an extremely low air fraction can be created. The bottom-up method is ideal for creating SHSs with a very low air percentage [39]. HE is a well-known technology for micro-nano structuring thermoplastic polymers with a resolution of 5-10 nm. It is an economical technique that involves imprinting a millimetre to a nano meter-scale stamped design onto a polymer at a suitable temperature and pressure [32]. Holography, biomedical applications, optical waveguides, thin-films solar cells, organic light emitting diodes, nanophotonic metamaterials, microfluidics and biochips [40-41] are just a few of the uses of HE [42]. The top-down approach is primarily concerned with etching techniques [43]. This process involves copying patterns from a master mold and then applying them to a replica [9]. The HE is classified into three categories such as plate-to-plate (P2P), roll-to-plate (R2P), and roll-to-roll (R2R). Table 2.1 indicates a summary of classifications of the HE depending on various factors like accuracy, operational tool, fabrication technique, and processing efficiency. There is a clear distinction between three different types of HE techniques. The P2P HE is easier to use since it provides great accuracy when copying the structures into the substrate, but the main disadvantage is that it is not as efficient as other techniques. In the case of R2P HE, the processing cycle is simple to use and provides high accuracy in terms of the size, height, and shape of replicated structures. The more sophisticated variant of the HE approach is R2R. Although the process of embossing the polymer is fairly tough as compared to planar, HE, it yields highly precise structures [44].

Table 2.1. A summary of classification of hot embossing (HE) techniques.

Based factors	P2P hot embossing	R2P hot embossing	R2R hot embossing
Operational tool	Very easy	Easy	Moderate
Method for fabrication	Discontinuous	Continuous	Continuous
Processing efficiency	Low	Moderate	High
Accuracy	High	High	High

The HE technique involves four key steps such as (i) heating the polymer film to molding temperature, (ii) isothermal molding, (iii) maintaining the constant force while allowing the molded polymer sheet to cool down to room temperature, and

(iv) removing the component by withdrawing the mold [45]. Patil et al. [46] developed a P2P setup for the HE technique. On a polystyrene film, this configuration was utilized to make nanogrooves and pillar structures. The produced structures that increase the value of surface roughness were found responsible for the surface transition from hydrophilic to hydrophobic. The availability of nanostructures on the polymer surface leads to an increase in contact angle on structured surfaces. The size of the structures also influenced the wettability of the surface. The HE is a simplistic physical surface shaping technique that can permanently change the wettability surface transitioning from hydrophilic to hydrophobic or superhydrophobic depending on the nanostructures grown. Liu et al. [47] presented an innovative HE approaches for fabricating nanostructure arrays on transparent glasses, which involves carefully managing process parameters and including an ultrasonic vibration-assisted demolding process. Different types of nanostructures are shown in Fig. 2.4. Nano structures come in a variety of shapes and sizes, and by altering the geometry of an existing pattern, the topography changes resulted in improved results. It is possible to fill the polymer with multiscale microstructure patterns by using a single step HE approaches to successfully produce microstructural patterns at multiple scales onto the surface of the polymer substrate. These findings show that the polymer HE processes may be used to build a variety of effective and flexible microstructure pattern devices using an in-homogeneity heating approach.

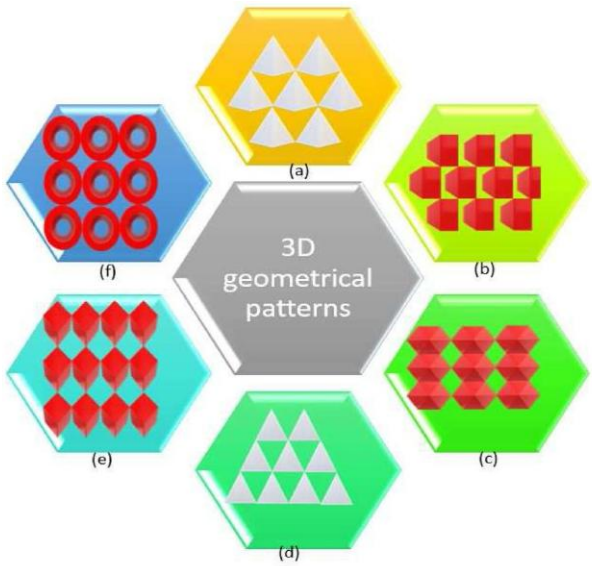

Fig. 2.4. Different types of 3D geometrical patterns that could be utilized to promote the creation of hierarchical surfaces (a) triangular pyramidal, (b) 3D rectangular, (c) hexagonal prism, (d) triangular planar, (e) diamond morphological structure, and (f) cylindrical geometry.

2.3. Progress in polymer-based superhydrophobic coatings (SHCs)

Researchers and manufacturers have employed a variety of polymer films to create SHCs that are strong, stable, and long lasting. Shape-memory polymers have recently been used to create mechanochemically robust and self-healing SHSs [48]. Thermoplastic polymers are broadly categorized into amorphous polymers and semi-crystalline polymers. Each category is further subdivided into three types of polymers based on their thermal stability standard, technical, and high performance. Because an amorphous polymer is more transparent than a semi-crystalline polymer, therefore, it is more commonly used in optical applications [49]. Table 2.2 depicts the classification of polymers as well as their applications in various fields [50]. Using the appropriate polymers for a given application might be aided by this differentiation based on these terminologies.

Table 2.2. Classification of various polymers based on thermal and mechanical properties.

Polymers	Examples	Thermal resistance	Mechani-cal strength	Applications
Standard polymers	Polystyrene (PS), polyvinylchloride (PVC), polypropylene (PP), high-density polyethylene (HDPE), low-density polyethylene (LDPE), polymethyl methacrylate (PMMA), cellulose acetate butyrate (CAB)	Low	Low	Packaging films, containers, clothing
Engineering polymers	Polyoxymethylene (POM), polycarbonate (PC), polyamide (PA),	Low	Low	Car bumpers,

	polyethylene terephthalate (PET), thermoplastic polyurethane (TPU)			motorcycle helmets, skin boots
High-performance polymers	Polyvinylidene fluoride (PVDF), polytetrafluoroethylene (PTFE), polychlorotrifluoroethylene (PCTFE), ethylene chlorotrifluoroethylene (ECTFE),	High	High	Oil and gas industry, circuit board, surface coatings
Ultra-performance polymers	polyether-ether ketone (PEEK), fluorinated ethylene propylene (FEP) Polyimide (PI), polyamide-imide (PAI), polybenzimidazole (PBI)	Very high	Very high	

Fig. 2.5 shows a bar chart of research trends in polymeric SHCs derived from the Web of Science. According to the data, polymeric SHCs are in high demand between 2018 and 2020 for a variety of reasons. Polymeric SHSs can be directly produced using templates in a compression or injection mold cavity. Additionally, employing HE, micro-nanostructures can be created on before existing polymer materials like sheets or films to create superhydrophobic polymer surfaces.

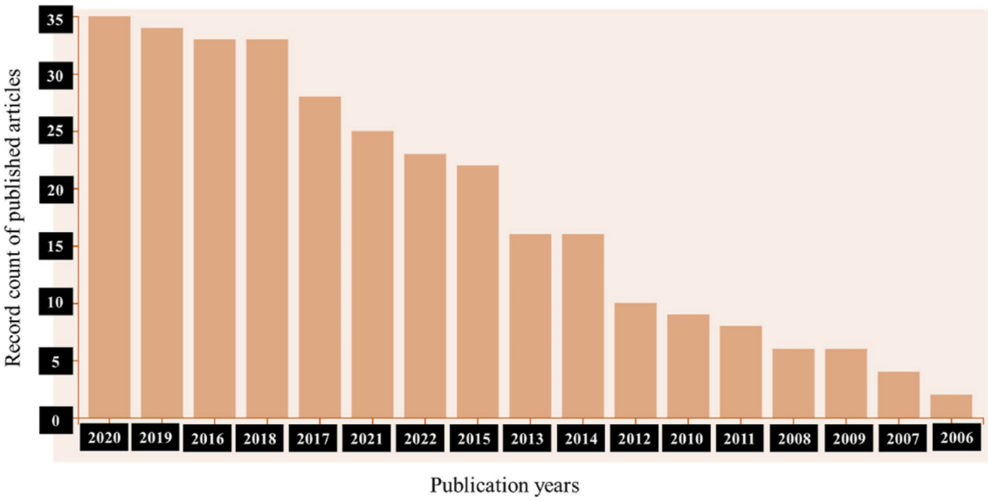

Fig. 2.5. The number of research papers published on polymeric superhydrophobic coatings (SHCs) demonstrating that the use of polymers as the base material is becoming more popular due to their numerous applications (Produced from Web of Science).

Even though various polymeric surfaces have been developed, none of them satisfies the physical understanding of the water drops onto the substrate's surface. In the current situation, a novel approach is required to understand the mechanism of generation of superhydrophobicity on polymer films for real-life applications. However, one of the biggest drawbacks of using superhydrophobic materials is their long-term endurance. Barbero et al. [51] revealed that nanostructure arrays with a high-density possessing feature sizes as small as 12 nm may be embossed using ethylene tetrafluoroethylene (ETFE) molds. The tests were carried out at 145-160^{0}C, 7 bar, and for 3.5 min. The developed nanostructures were then characterized by atomic force microscopy (AFM) and scanning electron microscope (SEM), and because of the stamp's flexibility and minimal stickiness, they showed no adhesion to the polymer substrate. Fig. 2.6 shows a schematic diagram of embossing and an illustration of the optical properties of the PMMA sheets that were prepared by the ETFE mold. The ETFE fluoromolds have been shown with SEM images of various microstructures. Fig. 2.6(a) is displaying the SEM images of the embossed microstructure on PMMA from the ETFE fluoromolds at 160^{0}C. The AFM scan of the topographical structures shows a height of 160 nm, which is used to emboss the lines as shown in Fig. 2.6(b). About 4 mm PMMA pillars were embossed for 2 min at 145^{0}C and 44 bar with an ETFE fluoromolds as shown in Fig. 2.6(c). At 135^{0}C and 4.7 bar for 5 min,11 mm broad and 11.5 mm deep holes were engraved in PMMA as shown in Fig. 2.6(d). Microstructures are shown on Teflon AF 1600 in Fig. 2.6(e) and after imprinting the structures ETFE mold as shown in Fig. 2.6(f). Because ETFE stamps are so flexible, they can be used many times. However, the coating's durability has not been tested, which could be important in practical applications.

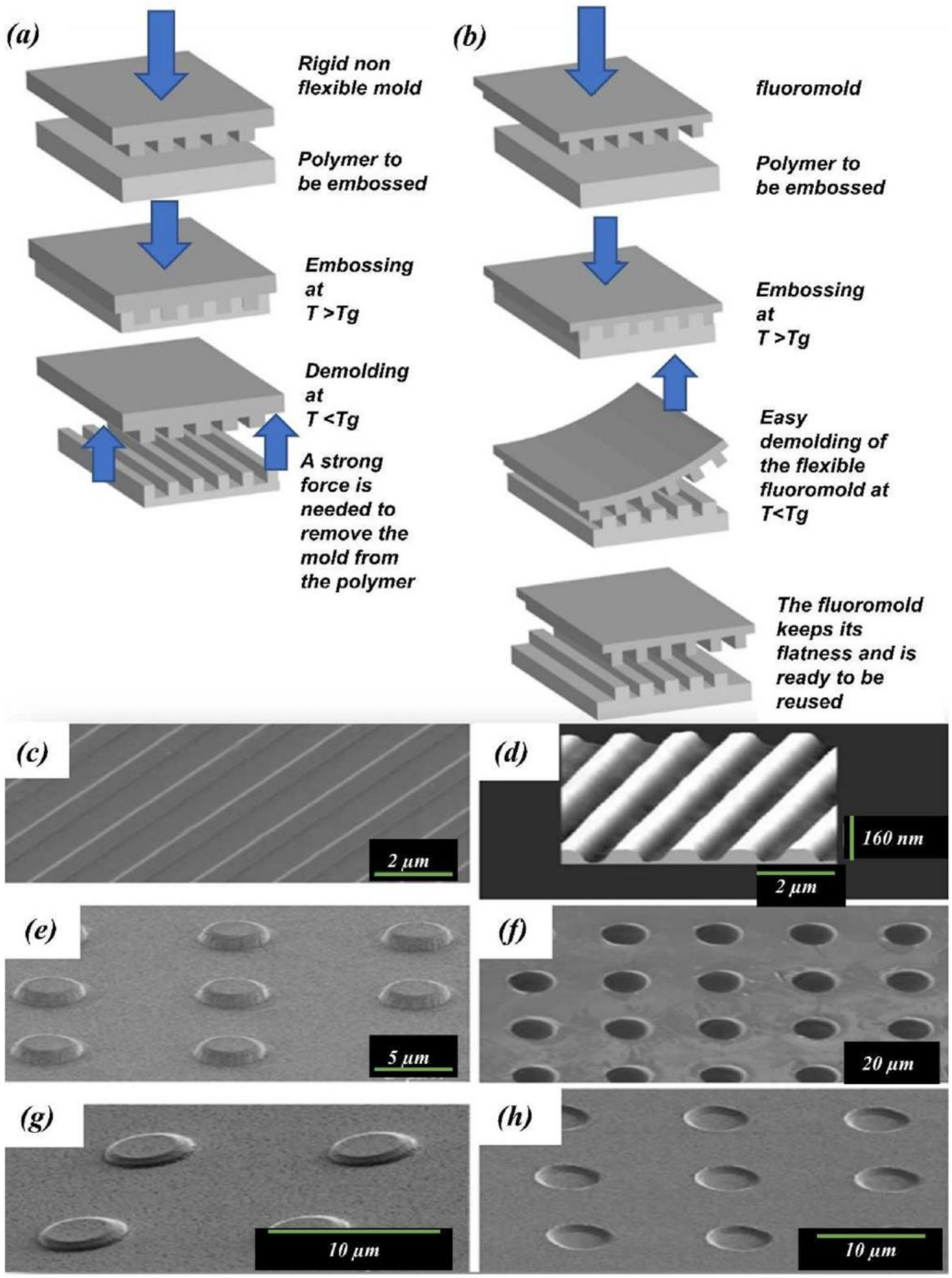

Fig. 2.6. Schematic of embossing using (a) rigid mold, (b) using fluoromolds, (c) embossed microstructures from ethylene

tetrafluoroethylene (ETFE) mold, (d) atomic force microscopy (AFM) image of the height of the microstructures, (e) 4 mm pillars embossed on the polymethyl methacrylate (PMMA) sheets, (f) 11 mm broad and 11.5 mm deep holes engraved in PMMA sheet, (g) microstructures on amorphous fluoropolymer (Teflon AF) 1600, and (h) ETFE film after imprinting the microstructures (Reprinted with permission from Ref. [51], Journal of Membrane Science, © 2020 Elsevier B.V.).

Shivaprakash et al. [52] presented a simple and innovative R2R embossing technique for an SHS comprised of well-ordered micro pillar formations on a polyamide (PA) film that demonstrates a high-water repellence. Fig. 2.7(a) depicts a schematic diagram for the tool fabrication process of micro-pillar arrays, and Fig. 2.7(b) gives an illustration of the R2R embossing process. The procedure has been carried out at two different temperatures, such as 150-155^{0}C and 190-195^{0}C. It was discovered that in the first case, rolling speed and pressure affected the height of the micro-pillars, whereas in the second case, rolling speed and pressure were insensitive to the height of the micro-pillars. Fig. 2.8(a) shows FESEM images (1-6) of embossed micro-pillar structures on (PA) polyamide sheet at 150-155^{0}C, and Fig. 2.8(b) shows the FESEM images (7-12) of embossed micro-pillar structures onpolyamidesheetat190-195^{0}C. However, more research is needed to optimize different geometrical parameters regarding stabilizing the SHCs, and durability tests must also be performed to determine the coating's life.

-+

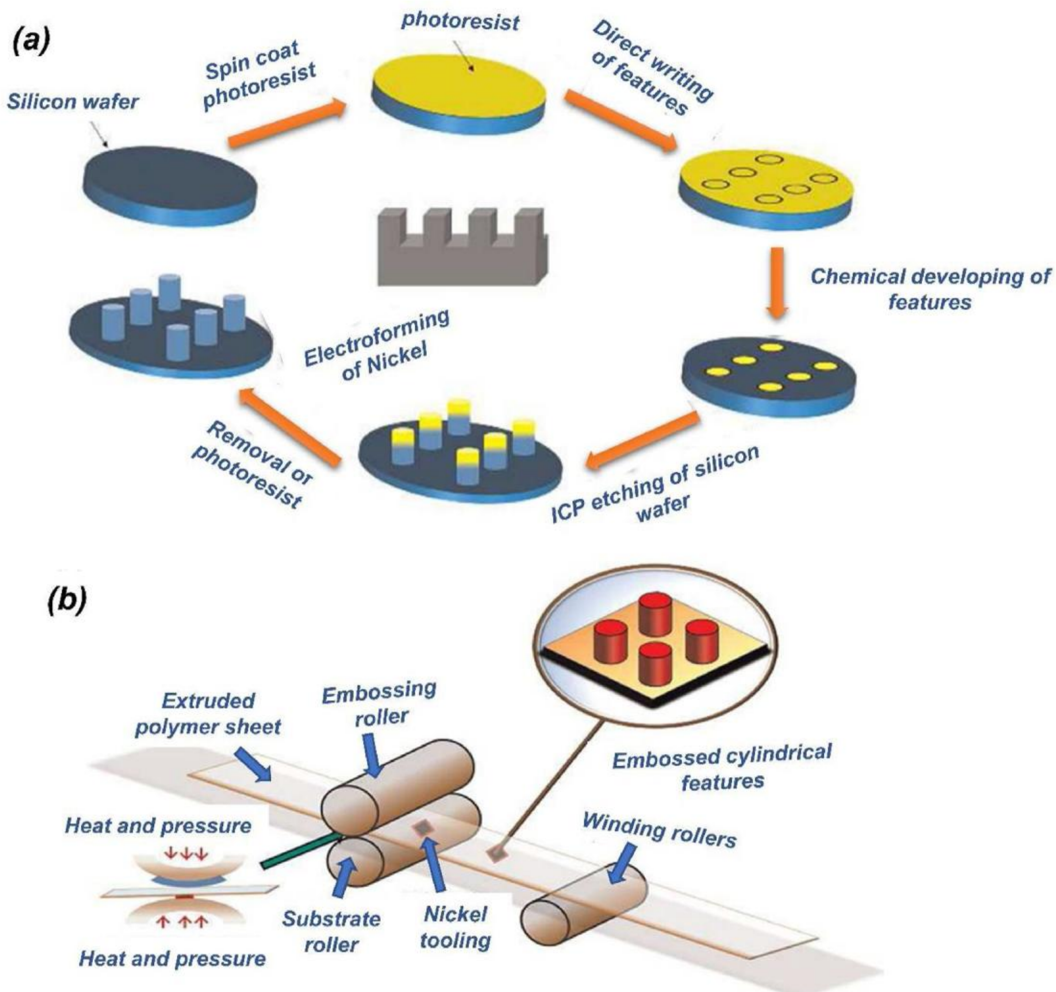

Fig. 2.7. (a) Schematic diagram for the tool fabrication process of micro-pillar arrays and (b) depictions of roll-to-roll (R2R) embossing (Reprinted with permission from Ref. [52], Copyright under De Gruyter, International Polymer Processing).

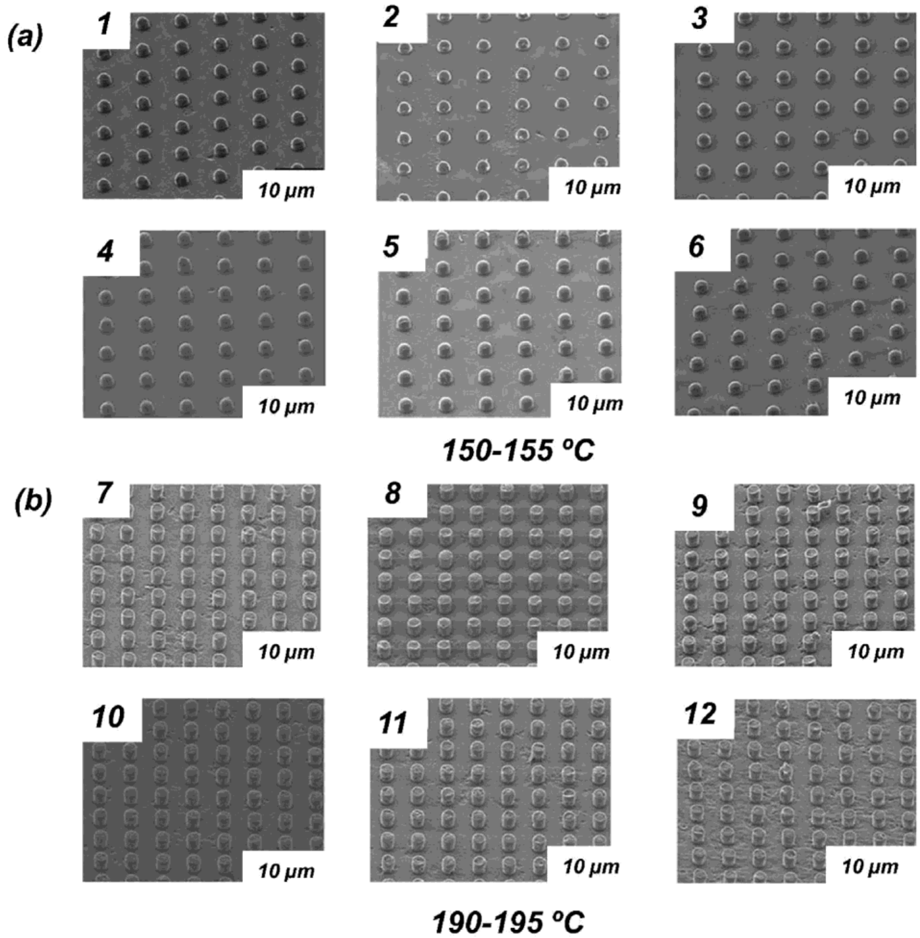

Fig. 2.8. (a) FESEM images (1-6) of embossed micro-pillar structures on polyamide (PA) sheet at 150-155°C and (b) FESEM images (7-12) of embossed micro-pillar structures on PA sheet at 190-195°C (Reprinted with permission from Ref. [52], Copyright under De Gruyter, International Polymer Processing).

Sun et al. [53] demonstrated the preparation of biomimetic hierarchical roughness using the P2P technique. A schematic diagram for the development and expansion method for the special bio mimetic topographical structures is indicated in Fig. 2.9(a). However, Fig. 2.9(b) depicts the SEM scan of the stainless-steel micro-platforms with a mesh no. of 300 at micro scale and nanoscale. To replicate the microstructures at the bottom, a polyethylene and ethylene-vinyl acetate (PE/EVA) substrate was used, and at the top, a stainless-steel substrate was used, as well as two pieces of PC substrate on the sides for support, at an optimum temperature of 94^{0}C and pressure of 6 MPa. However, this method only consumed 20 s to finish the job, but the new coating's long-term durability was not tested.

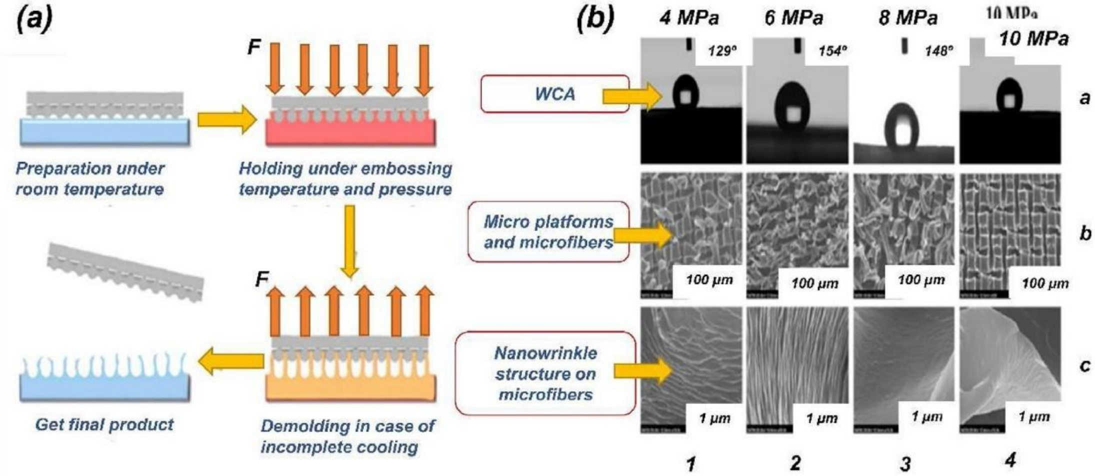

Fig. 2.9. (a) Development and expansion process of the special biomimetic hierarchical structures used in plate-to-plate technique, (b) water contact angle (WCA) and surface morphologies at different processing parameters at microscale on micro-platforms and microfibers and nanoscale on nano wrinkle structures on microfibers (Reprinted with permission from Ref. [53], ACS Omega, Copyright © 2019 American Chemical Society).

In another report, Roslizar et al. [54] fabricated the micro- structures on fluorinated ethylene propylene (FEP) films for the application of PV modules. It was observed that the embossing force has a major influence on the morphology of the microstructures, as texturing increases with increasing embossing force. Fig. 2.10(a) depicts the surface morphology of nickel shim possessing different-sized micro-textures and (b) magnified view of the surface features of nickel shim. SEM pictures of microstructured FEP samples produced at 280 °C with varying stresses, (h) a random microstructured FEP sample with multiscale micro-texturing on FEP film. Fig. 10(i,j) depicts the WCA of 156° with a contact angle hysteresis (CAH) of 8° at an optimum temperature of 280°C and pressure of 5 kN. Fig. 10(k) shows a comparison of the self-cleaning performance after adding soiled samples, and Fig. 2.10(l) shows that self-cleaning performance after water was deposited on the surface of the FEP film, and a comparison was made between un-textured and textured film. For the advancement of superhydrophobic cover film, it is critical to improve the optical transmittance of the glass cover on the surface of PV modules. Such work can be quite beneficial for optical applications.

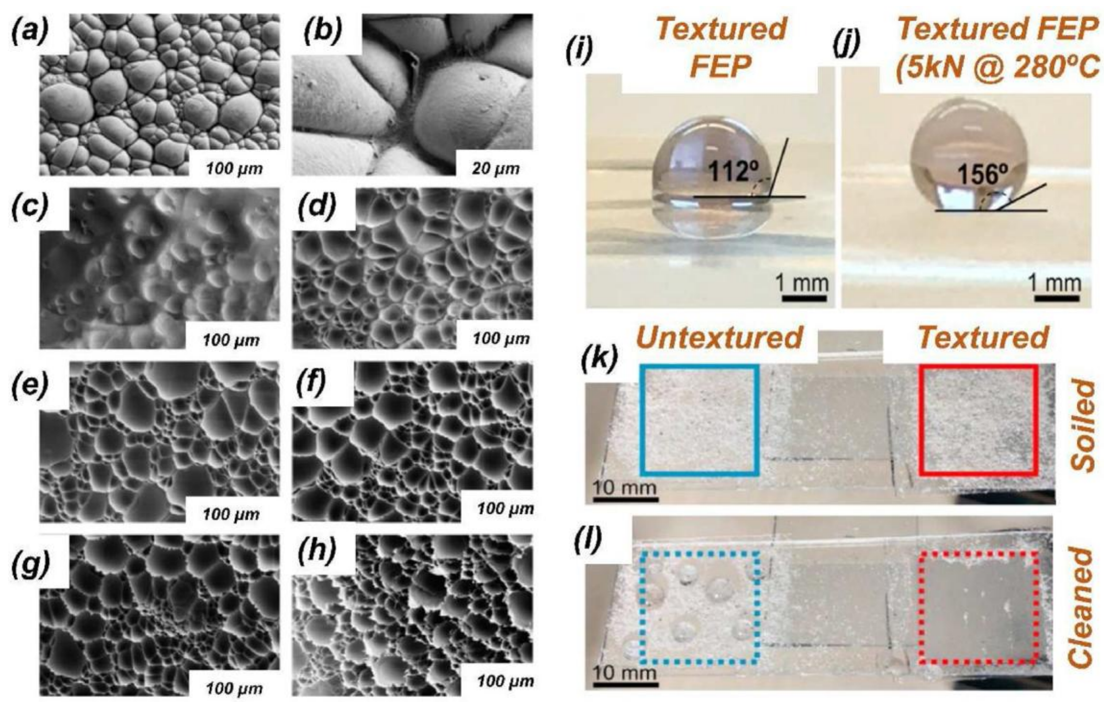

Fig. 2.10. SEM pictures showing (a) nickel shim with micro-textures and (b) a magnified view of the surface of a nickel shim. The SEM images of micro structured FEP samples were produced at 280°C with differing forces. (h) Fluorinated ethylene propylene (FEP) sample with multiscale micro-texturing, (i) water contact angle of plain surface, (j) water contact angle (WCA) of modified, (k) self-clean demonstrating of textured and un-textured FEP, and (l) the self-cleaning performance was evaluated using water droplets (Reprinted with permission from Ref. [54], Solar Energy Materials and Solar Cells, Copyright © 2018 Elsevier B.V.).

Gao et al. [44] noted that micro-powder HE was used to replicate hierarchical structures on polytetrafluoroethylene (PTFE) films at a reasonable cost. To replicate, a micro pyramid-array mold was used, and Fig. 2.11 depicts the SEM scans of micro structured pyramid-array on PTFE films fabricated using powders with varying particle sizes (a) 8.2 mm, (b) 20 mm, and (c) 50 mm. They demonstrated the durability and hydrophobicity of the textured film through a series of tests as shown in Fig. 2.11(d). Fig. 2.12 depicts the results of various evaluations and found that after completing all the tasks, the WCA remained unchanged, indicating that the film is extremely durable. Although the impact of pressure, temperature, and particle size on the micropattern formation quality was thoroughly discussed. A mathematical model that can provide us the specific details about surface morphology and its dependence on the geometrical patterns is still needed to apply such results for practical applications.

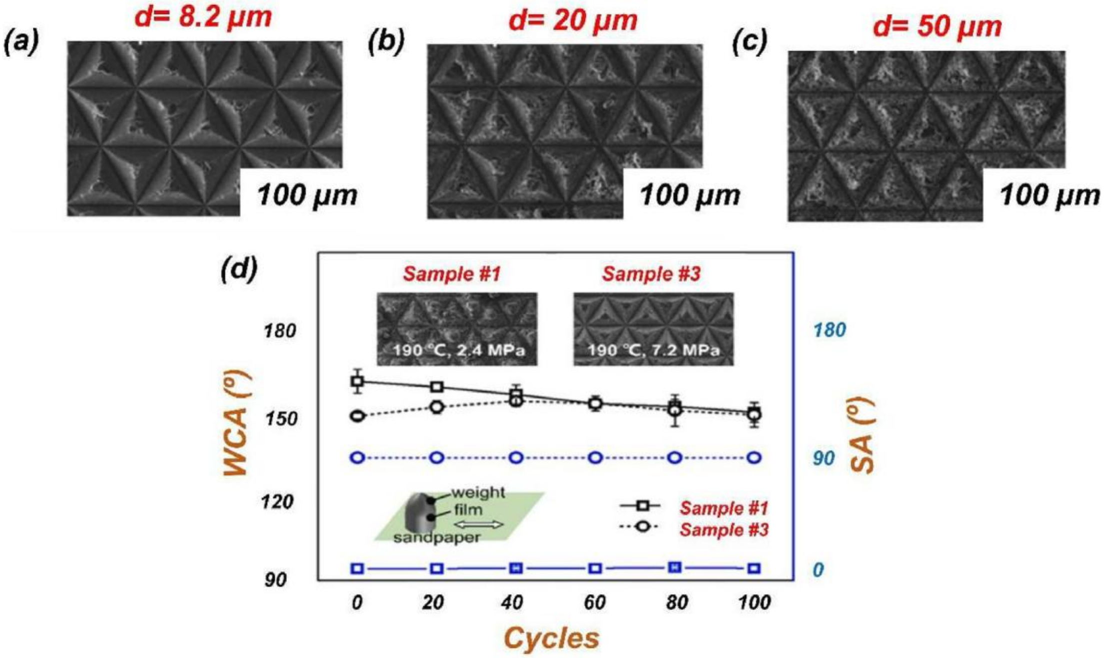

Fig. 2.11. Micro pyramid-array polytetrafluoroethylene (PTFE) films are made with powders of various particle sizes (SEM pictures). (a) 8.2 mm, (b) 20 mm, (c) 50 mm, and (d) mechanical robustness of the sample measured water contact angle (WCA) and contact angle hysteresis (CAH) every 20 cycles when carrying tests for wear resistance (Reprinted with permission from Ref. [44], Journal of Materials Processing Technology, © 2021 Published by Elsevier B.V.).

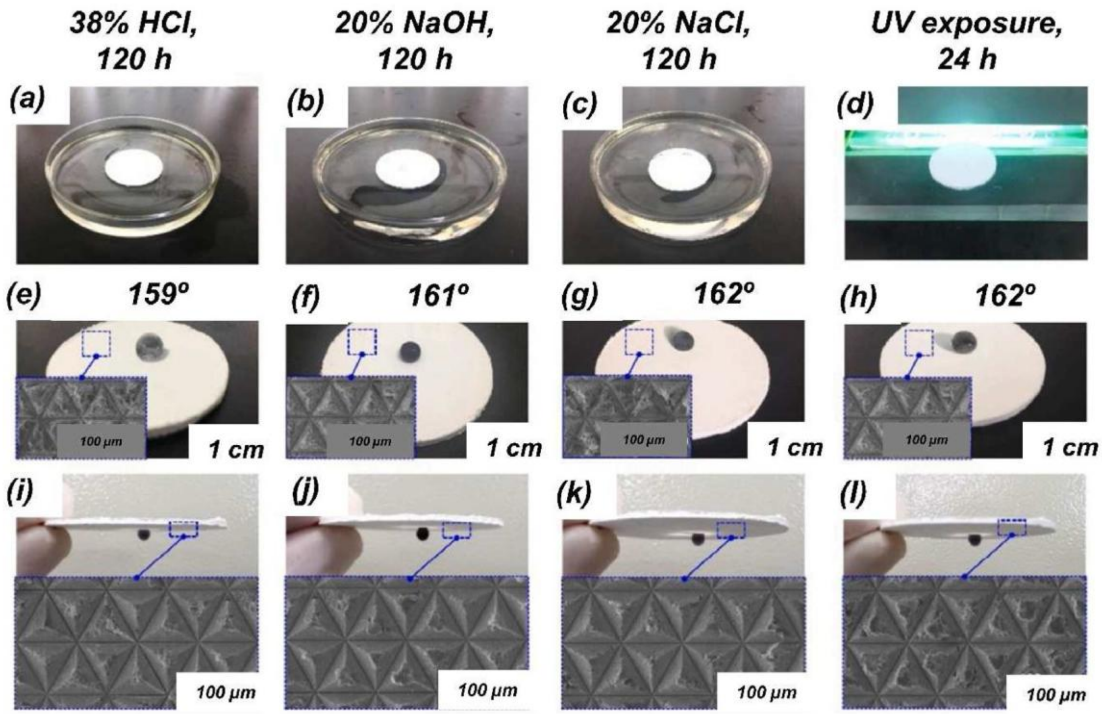

Fig. 2.12. Durability in opposition to (a) strong acid, (b) alkali, (c) salt solutions, and (d) ultraviolet (UV) radiation demonstrating the robustness of superhydrophobic property (from WCA) (Reprinted with permission from Ref. [44], Journal of Materials Processing Technology, © 2021 Published by Elsevier B.V.).

In another study, Barz et al. [6], fabricated conical microstructures on Polyurethane (PU) film using a simplistic method of HE. Fig. 2.13 depicts the SEM pictures of the fabricated superhydrophobic conical microstructures (a,b) and (c,d) imprinted on a PU film. The wetting behavior and optical properties were evaluated, and it was determined that these surfaces have a high degree of super- hydrophobicity. To increase the WCA, more plasma etching is required. Fig. 2.13 shows the droplets of water on various surfaces of PU film (e) flat PU without coating, (f) fluorocarbon plasma polymer coated with micro-textures, (g) uncoated PU film, (h) micro- structured coating on a fluorocarbon plasma polymer. Although extensive research was performed to determine the durability of SHSs, it is clear that exposure to ultraviolet (UV) radiation and water weathering causes the degradation of such surfaces over time. This demonstrates that the plasma coating's longevity needs to be increased.

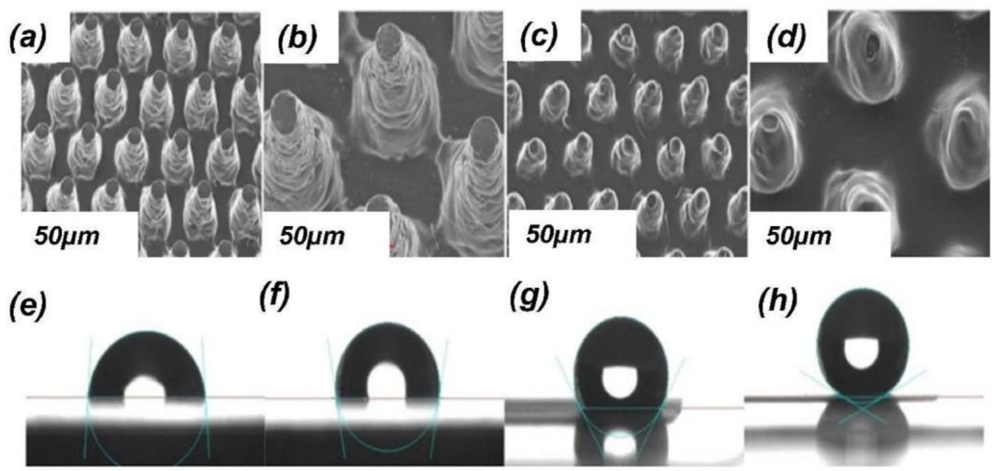

Fig. 2.13. SEM pictures of the micro structured superhydrophobic surface (a,b) and (c,d) imprinted on a PU film, water drops on differently functionalized PU film surfaces (e) uncoated flat PU, (f) flat PU coated with a fluorocarbon plasma polymer, (g) microstructure without coating, and (h) fluorocarbon plasma polymer coated with microstructures (Reprinted with permission from Ref. [6], Plasma Processes and Polymers, Copyright under Wiley Online Library).

Li et al. [55] reported the fabrication of micro-meshes and micro-groves on polyethylene (PE) films for achieving super-hydrophobicity. Fig. 2.14 depicts a procedure of manufacturing the micro structured high-density polyethylene (HDPE) films. Fig. 2.15 shows the surface morphologies of the template (a) and micro- structures on HDPE film surface (b, c), images of micro structured high-density polyethylene (HDPE) film (d) before, (e, f) during, and (g) after drowning in blue ink dyed water, (h) wetting state, and (i) WCA on bare HDPE film; (j) wetting state and (k) WCA on micro structured HDPE film. The WCA of 151.8° and CAH of >90° were demonstrated, and after a series of durability tests, it was determined that the film is robust for any practical application. However, a particular application-oriented work was not performed to test the reliability of obtained results.

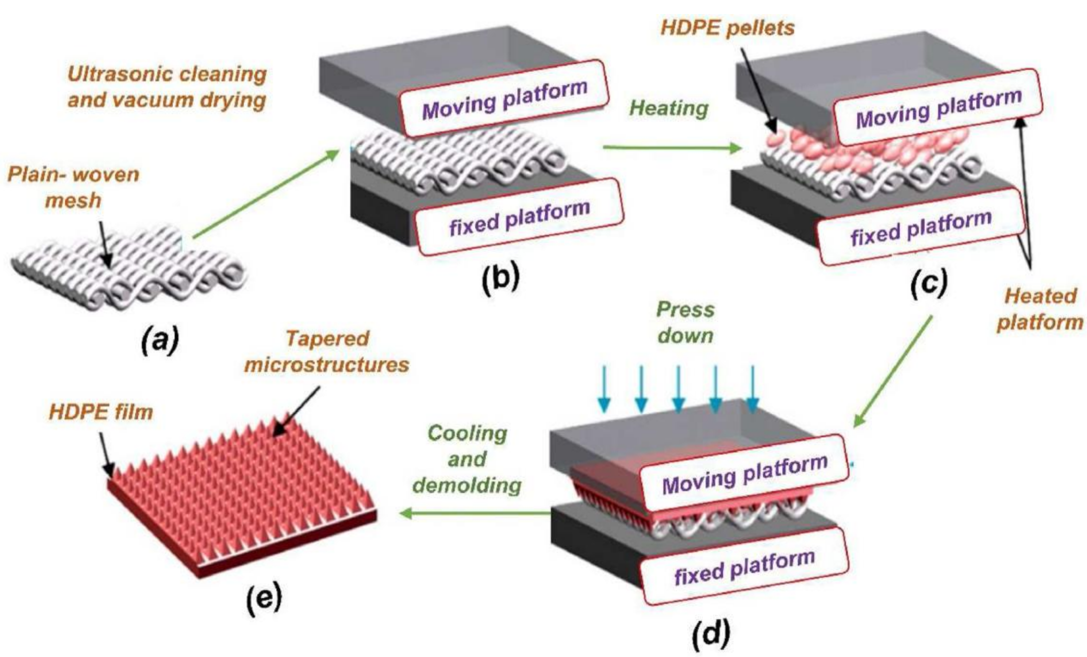

Fig. 2.14. Schematic process for manufacturing of micro structured HDPE films (Reprinted with permission from Ref. [55], Journal of Bionic Engineering copyright © 2022 Springer Nature Switzerland).

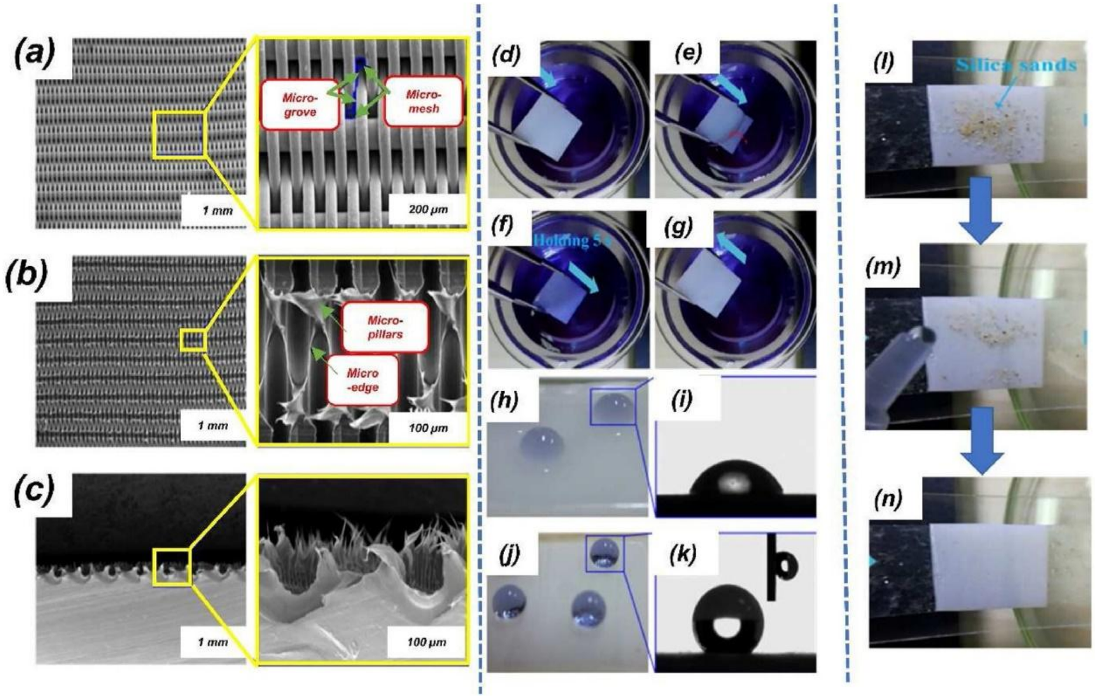

Fig. 2.15. Surface morphologies of the template (a) and microstructures on high-density polyethylene (HDPE) film surface (b, c), micro structured HDPE film (d) before, (e, f) during, and (g) after drowning in blue ink dyed water, (h) wetting state, and (i) water contact angle (WCA) on bare HDPE film; (j) wetting state and (k) WCA on micro structured HDPE film (Reprinted with permission from Ref. [55], Journal of Bionic Engineering copyright © 2022 Springer Nature Switzerland) (For interpretation of the references to color in this figure legend, the reader is referred to the Web version of this article).

Table 2.3 summarizes the properties of unmodified polymers in terms of thickness, porosity, melting point, and WCA. This table makes it simple to determine which polymer film will work best for achieving superhydrophobicity. We can accurately estimate the surface's character by knowing the WCA of the plain surfaces. As shown in the table, PVDF, ETFE, and PTFE are all hydrophobic in nature, making them ideal for improving surface quality in terms of roughness and wettability. This makes the fabrication process simpler, and by understanding these characteristics, durable SHSs can be produced with ease.

Table 2.3. Characteristics of various polymer films.

Material	**WCA**	**Thickness**	**Melting point**	**Porosity**
Polyvinylidene fluoride (PVDF)	145° ± 2°	125 mm	163.49°	62%
Ethylene tetrafluoroethylene (ETFE)	106°	200 mm	225-270°	40-75%
Polymethyl methacrylate (PMMA)	68°	200 mm	160°	52-61%
Polytetrafluoroethylene (PTFE)	106.94°	200-400 mm	317-337°	50-70%
Polylactic acid (PLA)	75-85°	0.600 mm	150-160°	14-7%

In another study, Sun et al. [56] fabricated PVDF microporous membranes by employing rolling embossing with immersion precipitation as depicted in Fig. 2.16. The obtained WCA after texturing was 151.2°, and the CAH was 5.4°, which resembled a lotus leaf's surface. SEM, X-ray diffraction (XRD), pore size, AFM, porosity, WCA, and mechanical stability were used to analyse the developed membranes. AFM scans of PVDF film with varying roughness values are included in Fig. 2.17(a). After 50 friction cycles, the micro- nano hierarchical structure remained stable in aspects of the mechanical strength of the embossed membrane surface. PVDF membranes having a micro-nano hierarchical structure out- performed standard PVDF membranes in terms of performance and anti-fouling ability. Such membranes exhibit a great potential in membrane distillation operations. The developed method proved easy, cost-effective, and repeatable, allowing for long-term continuous production of superhydrophobic PVDF microporous membranes. By combining thermally induced phase separation (TIPS) with rolling embossing, PVDF membranes with micron/ submicron geometrical features were prepared. Initially, the WCA of PVDF membranes was only 98.7°, and after generating roughness by embossing, the high WCA of 154.8° and CAH of 1.9° were achieved [57]. In terms of energy and environmental-related applications, PVDF is widely used [58]. Fig. 2.17(b) depicts WCA and CAH before and after abrasion testing, indicating the coating's mechanical durability.

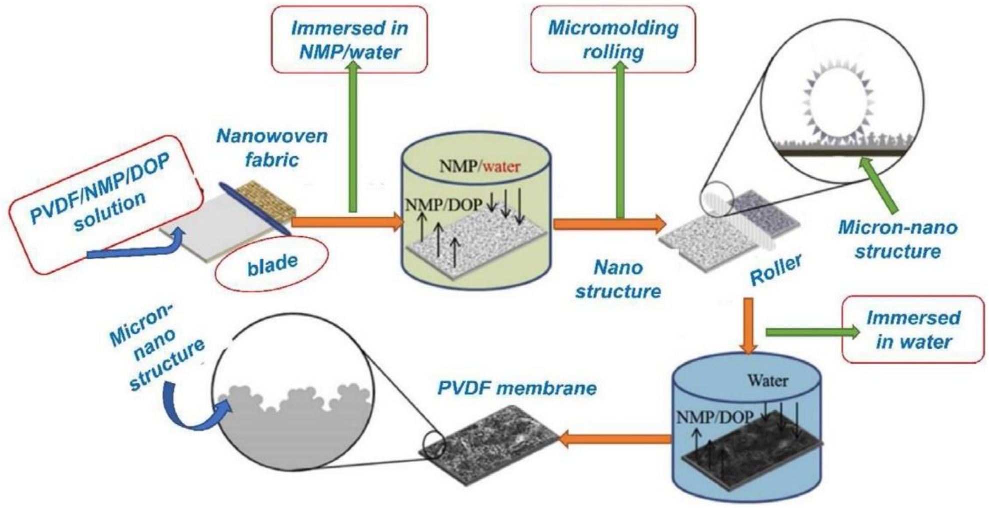

Fig. 2.16. The schematic diagram for the formation of micro-nano hierarchical structure in polyvinylidene fluoride (PVDF) microporous membranes (Reprinted with permission from Ref. [56], Journal of Membrane Science, Copyright © 2020 Elsevier B.V.).

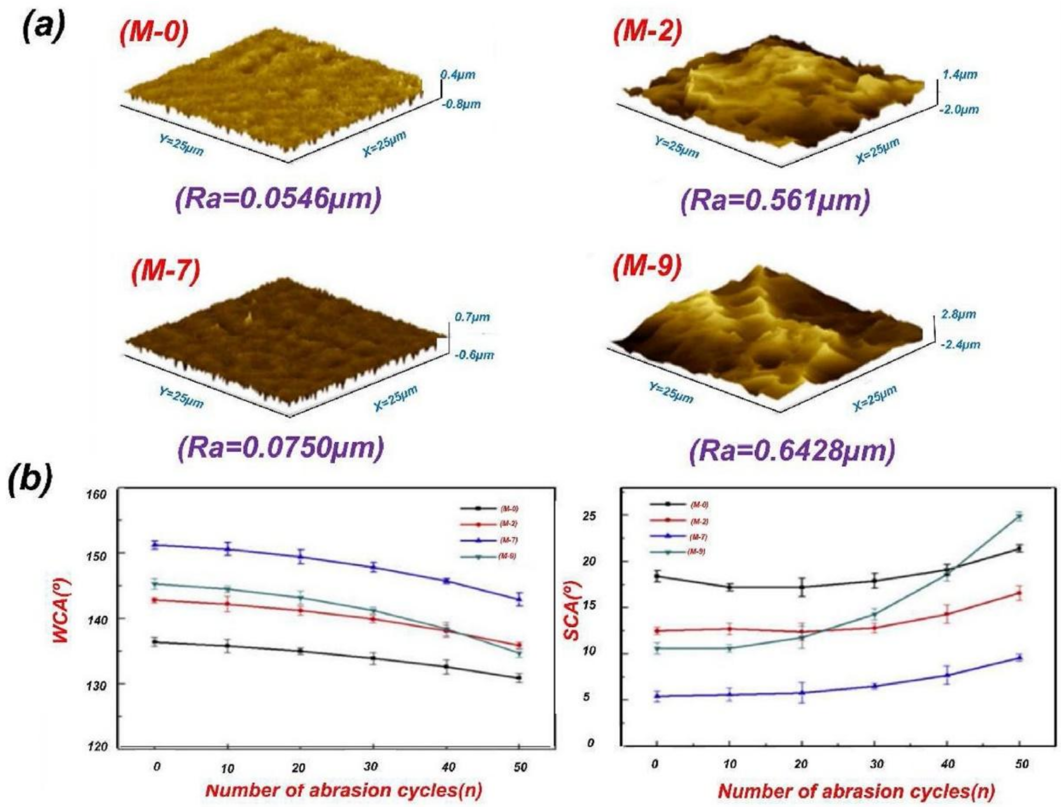

Fig. 2.17. (a) AFM pictures of PVDF film with different roughness values, and (b) water contact angle (WCA) and contact angle hysteresis (CAH) after abrasion testing (Reprinted with permission from Ref. [56], Journal of Membrane Science, Copyright © 2020 Elsevier B.V.).

Liu et al. [59] stated that by making a 3D array of micro-dimple mold and then replicating the features onto the polymer poly methyl methacrylate (PMMA), a 3D microlens array can be created. By using the position prediction model, a self-aligned multiball pattern was produced. The 3D array of micro-dimple embossing process is somewhat identical to traditional embossing. Instead of using a fabricated mold with a 3D microlens array, the shape of their spherical crowns is replicated by compressing a layer of cemented tungsten carbide balls self-aligned on the metallic glass surface. The reported method is economical and novel manufacturing approach for making 3D microlens arrays quickly. Further, the optical transmission was tested and found out that the process described in the study has numerous applications, including ultra-high-definition imaging and machine vision. Additionally, the 3D microlens array position prediction model was established by providing a clear physical interpretation of the patterns. However, there was no discussion of the 3D microlens array's longevity. PMMA has tensile and impacts strengths that are 7-18 times greater than ordinary glass, and its transmittance is 92%, which is also greater than glass [60]. In another study, Palacios-cuesta et al. [61] used polydimethylsiloxane (PDMS) stamps to replicate the micro-grooves onto the copolymer of polymethyl methacrylate-*co*-acrylic acid (PMMA-*co*-PAA) by HE method. An optimum temperature of 180 °C and a pressure of 15 bars were used in this method. However, in water vapor conditions, a decrease in WCA was observed, and the films prepared were truly unstable because the surface morphology was completely disrupted. Fig. 2.18(a) depicts an SEM image of circular microstructures prepared using a PDMS mold with a 2 mm spacing with a diameter of ~ 540 nm. Fig. 2.18(b) shows an SEM image of a line microstructure with approximately 25 mm lateral dimensions, whereas an SEM image of hexagonal microstructures with an approximate spacing of 3 mm between the hexagons has been indicated in Fig. 2.18(c). A relationship could be developed for a better physical understanding by optimizing the various micropattern parameters and may contribute to practical applications. The micropattern's durability was also not covered in their study. Moon et al. [62] imprinted the hierarchical patterns on poly- tetrafluoroethylene (PTFE) films by using the HE technique from a die and obtained a microfibril network upon the surface of patterned PTFE. The WCA of conventional PTFE films and patterned PTFE films are obtained as 111.9° and >150°. Hierarchical patterns were created using a wire electrical discharge machining (WEDM) and then transferred to PTFE films using a HE processes. However, it has been reported that when patterns are transferred onto polymer films, the polymers are torn out due to discharge creators, which can affect superhydrophobicity and durability. However, it was discovered that PTFE was impacted by higher temperatures when tested at a temperature of 280°C compared to PC polymer, which was tested at a temperature of 200 °C. This demonstrates that changing the processing parameter affects superhydrophobicity. This type of surface will be very useful due to various advantages such as resistance to light, UV radiation, weathering, chemical resistance, and low-temperature resistance [59]. In another study, Toosi et al. [63] used HE to imprint nanostructures onto the surfaces of three polymers: high-density polyethylene (HDPE), polylactic acid (PLA), and medical-grade polyvinyl chloride (PVC). For the replication, they used a femtosecond laser ablated stainless-steel mold. The replication of paraboloidal, tripled roughness, and cauliflower-shaped micropatterns was successful.

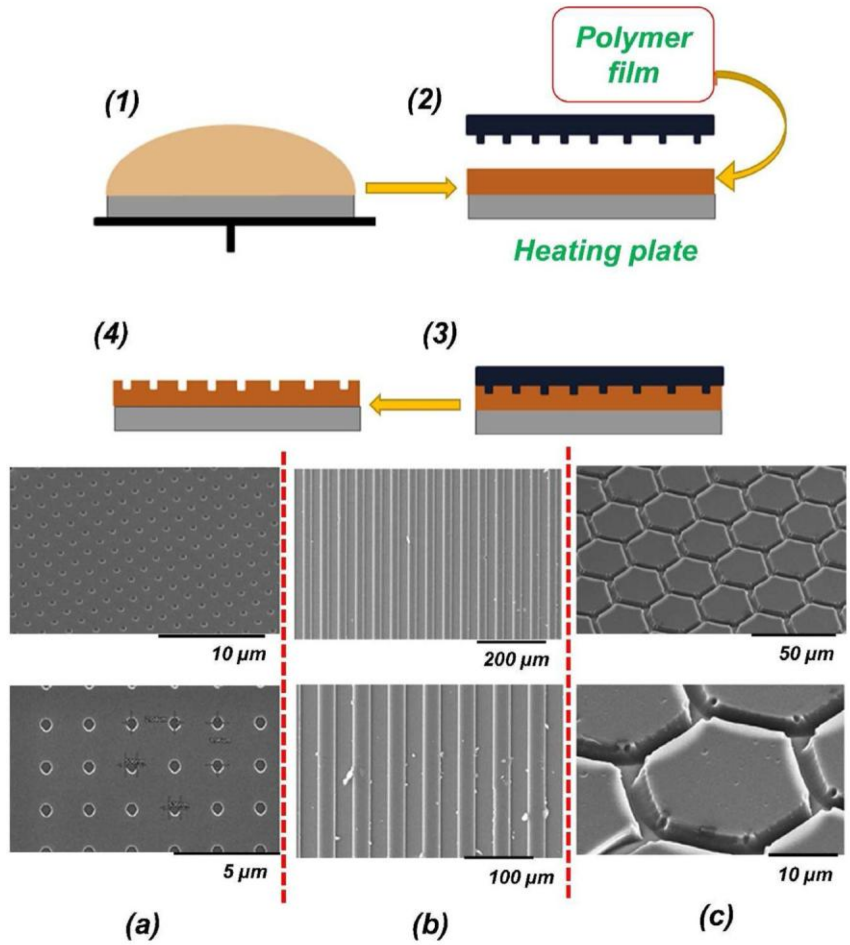

Fig. 2.18. (1-4) Schematic diagram for producing microstructures via hot embossing (HE) and SEM images defining microstructures (a) circular, (b) lining, and (c) hexagonal prepared via HE using polydimethylsiloxane (PDMS) stamps (Reprinted with permission from Ref. [61], European Polymer Journal, Copyright © 2014 Elsevier Ltd.).

The flowchart for HE technique to replicate hierarchical patterns is depicted in Fig. 2.19. Surface morphology and wetting states were investigated, and it was discovered that WCA of pattern HDPE and PLA was greater than 160°, while CAH was less than 5°. However, in the case of medical-grade PVC, they report a WCA of 148° and a high CAH greater than 90°. Fig. 2.20(a) depicts the SEM image for the patterned PLA for various patterns at different scale. 3D pictures of imprinted HDPE substrates with paraboloidal, tripled roughness, and cauliflower structures are shown in Fig. 2.20(b). However, Fig. 2.20(c) displays SEM images of imprinted medical PVC with paraboloidal, tripled roughness, and cauliflower patterns. Despite the fact that the fabrication part was completed, the mechanical durability of patterned surfaces was not demonstrated.

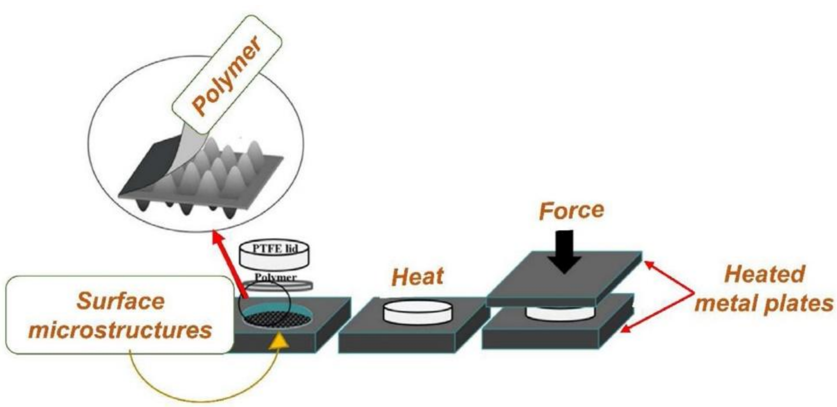

Fig. 2.19. Flowchart for replication of hierarchical patterns onto polymers (Reprinted with permission from Ref. [63], Applied Surface Science, © 2016 Elsevier B.V.).

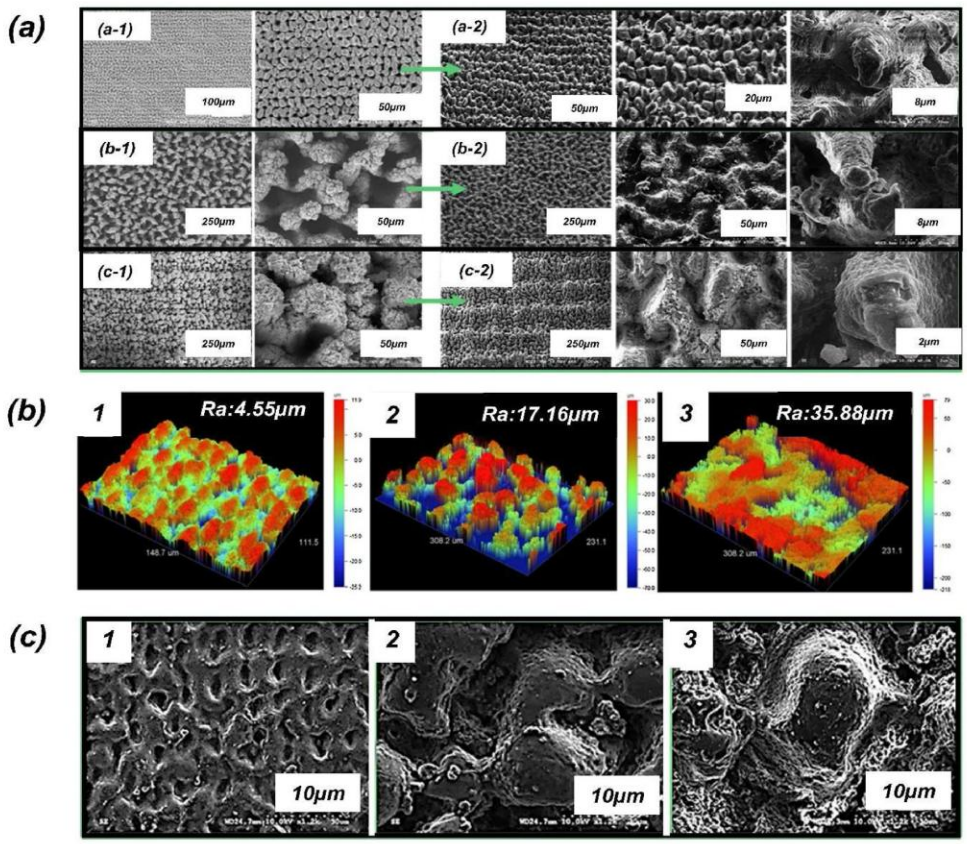

Fig. 2.20. (a) SEM image for the patterned polylactic acid (PLA) for paraboloidal, tripled roughness, and cauliflower pattern at a different scale, (b) 3D pictures of imprinted high- density polyethylene (HDPE) substrates with paraboloidal, tripled roughness, and cauliflower structures, and (c) SEM images of imprinted medical PVC with paraboloidal, tripled roughness, and cauliflower patterns (Reprinted with permission from Ref. [3], Applied Surface Science, © 2016 Elsevier B.V.).

Gong et al. [64] employ a highly efficient HE method to create hexagonal micro-nanoarray structures upon the surface of poly- tetrafluoroethylene

(PTFE) film with dimensions of (25 mm × 25 mm × 1 mm) to create large arrayed SHSs. Fig. 2.21(a) shows the surface morphology for the hexagonal microstructures. The observed WCA was 154.6°, and the CAH was 5.5° (which was similar to the lotus leaf surface) after optimizing the HE parameters, such as time, temperature, and pressure. In the HE processes, a temperature of 130°C and an optimum pressure in the range of 55-85 MPa were used. The surface morphology of the embossed film was characterized using SEM showing the WCA varies with the pressure. For example, the WCA for 66 MPa is 136.6°, whereas the WCA angle for 85 MPa is 153.4°. The thermal stability of the PTFE film was tested over a wide temperature range of 60-430°C by placing it in a tube furnace for 2 h. It was found that polytetrafluoroethylene (PTFE) holds the properties of thermal stability until 340°C as shown in Fig. 2.21(c) indicating that it has great durability and longevity.

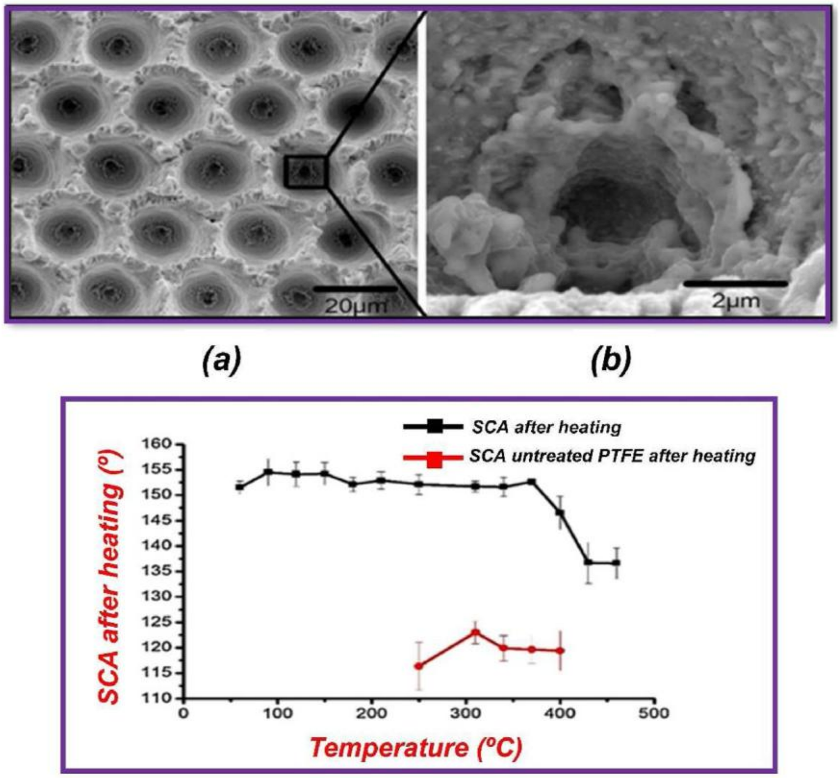

(c)

Fig. 2.21. Surface morphology for hexagonal microstructures at the scale of (a) 20 mm and (b) 2 mm, (c) WCA after heating for 2 h in a tube furnace (Reprinted with permission from Ref. [64], Applied Surface Science, Copyright © 2015 Elsevier B.V.).

Fig. 2.22 depicts the SEM images of microstructures of patterned PTFE film at different temperatures. Because it is thermally stable, it can be used in optical applications and can play a significant role in optical devices.

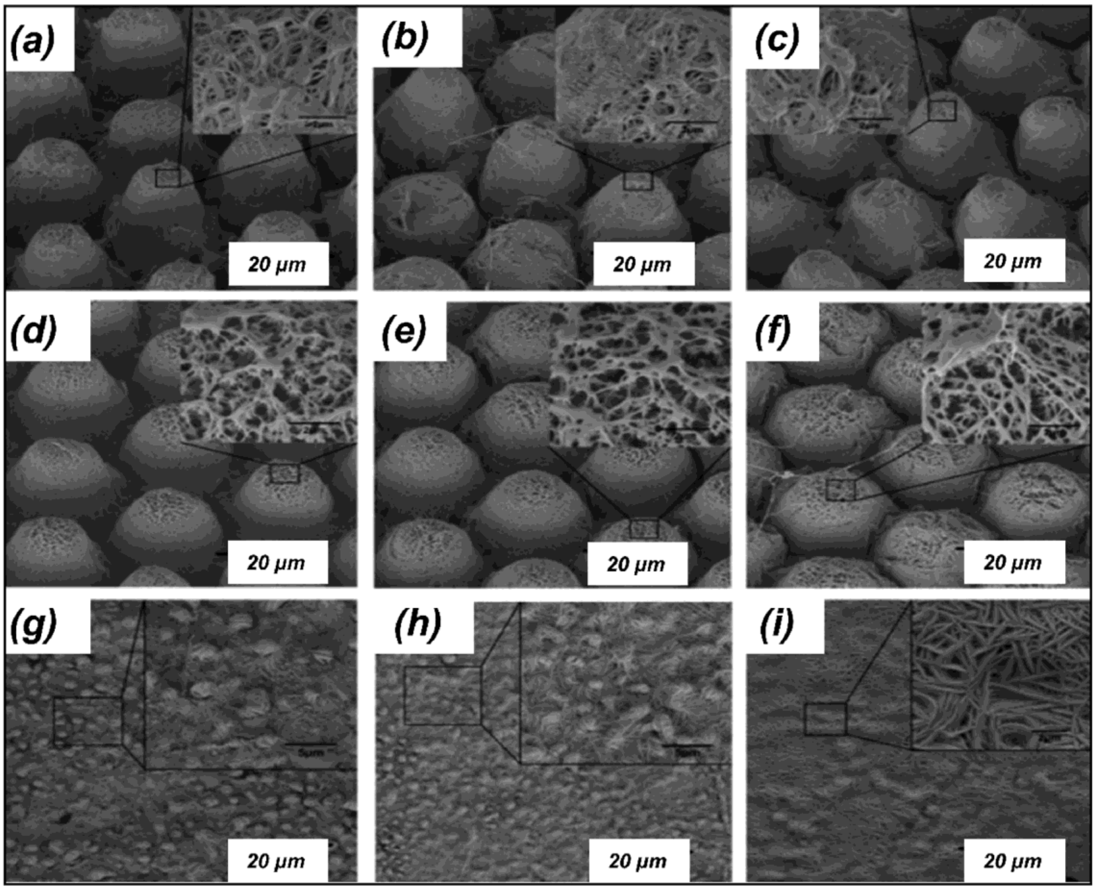

Fig. 2.22. Microstructures of patterned polytetrafluoroethylene (PTFE) after 2 h in a tube furnace at various temperatures of (a) 60 °C, (b) 120 °C, (c) 180 °C, (d) 250 °C, (e) 310 °C, (f) 340 °C, (g) 370 °C, (h) 400 °C, and (i) 430 °C (Reprinted with permission from Ref. [64], Applied Surface Science, Copyright © 2015 Elsevier B.V.).

In another study, Chen et al. [65] developed an innovative and efficient method for producing superhydrophobic biodegradable polylactic acid (PLA) films by integrating casting-thermal stretching and surface treatment as indicated in Fig. 2.23. These PLA films are self-cleaning and mechanically strong, with a long shelf life. After surface treatment, they analyzed the tensile characteristics of PLA, PLA-S, and the relevant materials and demonstrated that the sur- face modification did not affect the mechanical properties of the oriented PLA film obtained via stretching. Fig. 2.23 depicts a detailed description. This demonstrates that the superhydrophobic PLA film possesses outstanding heat, water, and acid resistance, extending the service life of the product. The PLA films are the most promising and eco-friendly [66] and also possess several distinct properties that make them an excellent choice for biomedical applications [67]. As a result, it is necessary to work on applications so that the developed coatings can be used at an industry scale. Fig. 2.24 displays the self-cleaning behavior of film, as the film continued to be clean despite being exposed to numerous particles and solutions, such as tea, coffee, and milk. This leads to the superior mechanical qualities, which can be used for diverse applications.

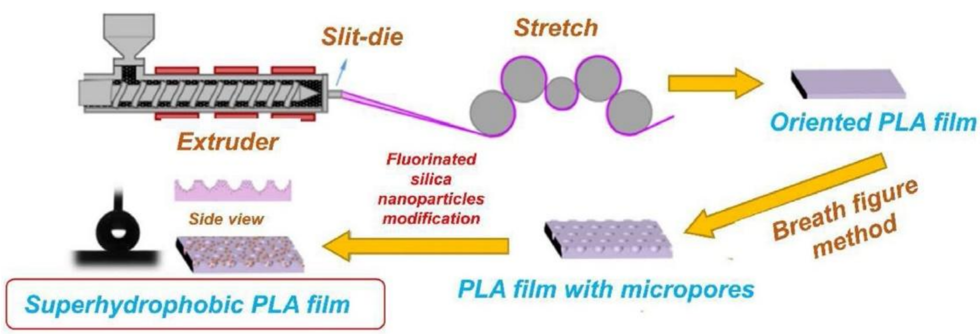

Fig. 2.23. (1) Schematic diagram to fabricate superhydrophobic PLA film (Reprinted with permission from Ref. [65], Copyright © 2021, American Chemical Society).

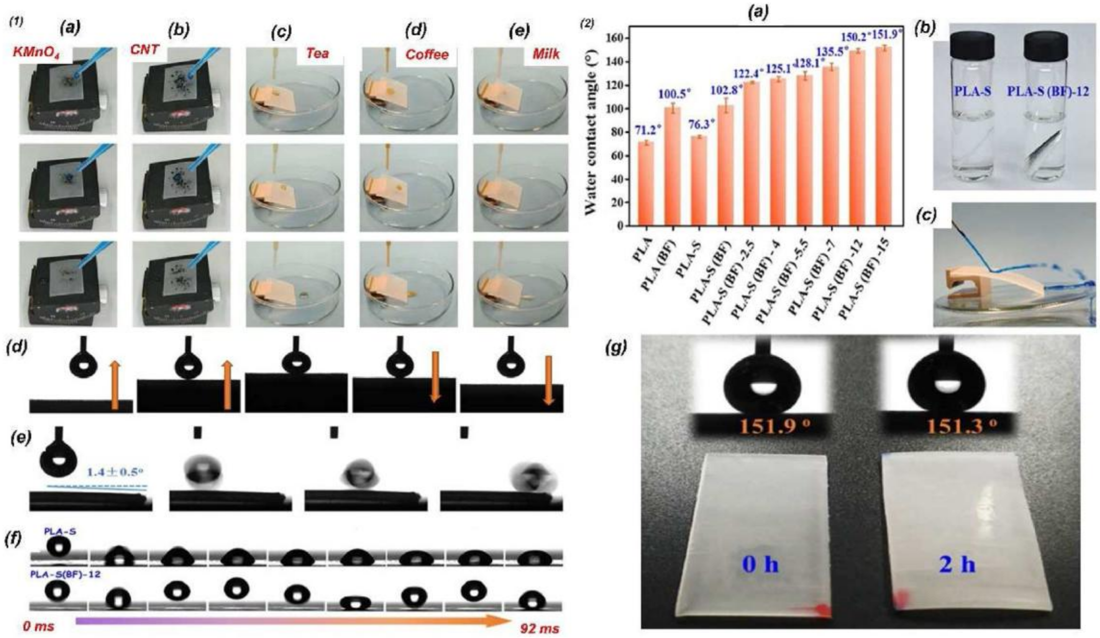

Fig. 2.24. (1)-(a) $KMnO_4$ and (b) carbon nanotubes (CNTs) were used as solid contaminants for self-cleaning. In the self-cleaning experiment, liquid pollutants such as milk, tea, and coffee were employed, (2)-(a) WCA of PLA films before and following surface modification. (b) Water-immersed PLA-S and PLA-S(BF)-12 samples. (c) Water jet rebounding off the PLA-S(BF)-12 film's surface (d) adhesive surface of the PLA-S(BF)-12 sheet is poor (e) with a slight tilt angle, a water droplet rolls on the PLA-S(BF)-12 film, (f) droplet attaching and bouncing actions to PLA-S and PLA-S(BF)-12 films once released from 0.5 cm height (Reprinted with permission from Ref. [65], Copyright © 2021, American Chemical Society).

In another work, Lee et al. [68] prepared SHSs for food packaging application. Both HE and UV embossing techniques were used to create cylindrical micro-pillars. Using the same nickel mold, cylindrical micro-pillars were transferred onto both UV-curable polyurethane-acrylate (PUA) (thermoset) and PP (thermoplastic) and also on pillar-shaped packaging material. The resulting WCA demonstrated the oleophilic characteristic of the embossed surface. The fabricated cylindrical pattern loses its property very quickly because the layer of edible oil remains for a very short duration, demonstrating that superhydrophobicity degrades. There is a great need to investigate the mechanical durability of these surfaces.

In summary:

(a) Combining the new methodology with HE technique for finding more precise structures should progress the research.

(b) Many SH surfaces have WCA >150°, but when these are exposed directly to the water jet test or sunlight, these sur- faces gradually lose their superhydrophobicity.

(c) Before being employed in real-world applications, the developed SHS needs to be further thoroughly examined in terms of stability.

(d) The pillared-shaped hierarchical structures have received the most attention, so there is a lot of scope for determining different shapes, including cylindrical, pyramidal, triangular, lens-shaped, and many more, to explore the effects of superhydrophobicity.

(e) ETFE polymers can be used for a wide range of applications in optical devices because of their hydrophobic and high transparency.

Based on the WCA and sliding abilities, conventional surfaces are compared to patterned surfaces in Table 2.4. Here, we can say that the maximum WCA of 167° has been obtained for cyclo-olefin polymer (COP) polymers via using the HE technique. The hierarchical micro-nanostructures were duplicated in COP with the use of an intermediate fluorinated polymer mold, which allows the COP substrate to be separated from the mold during HE [69]. The replication of nanopillars with a diameter of 250 nm becomes difficult. The nanopillars in ZF14-188 foil have deformed, and they are no longer evenly parallel to the surface. The local distortion of the fluorinated ethylene propylene (FEP) mold during the demolding process is most likely to blame for the deformed shape of the nanopillars. It could be improved by adjusting embossing parameters, such as the demolding temperature. Square nanopillars as tiny as 150 nm and a circular cylinder with a diameter of 100 nm were well duplicated. Nowadays, industries are looking for durable self-cleaning materials such as ethylene tetra-fluoroethylene (ETFE) for solar cell panels because the transparency of a substrate is essential for industrial applications [70]. As a result of this, it is vital to enhance the durability of the coating.

Table 2.4. Summary of various materials adopted to synthesize superhydrophobic surfaces (SHSs) based on Hot embossing (HE) technique.

Assisting used technique	Stamps	Substrate/ Base material	WCA (°) of substrate	CAH (°) of substrate	Shape of hierarchical structures	Area of stamps	Scalability	WCA (°) of textured surface	CAH (°) of textured surface	Ref.
Soft lithography technique	Epoxy	Polydimethylsiloxane (PDMS) film	87°	17°	Epoxy coating	10 × 20 cm^2	Thickness-50 mm	154°	5°	71
Hot embossing method	Brass mold	Polymethylmethacrylate (PMMA)	65° ± 4°	–	V-grooves	–	Period-200 mm	159° ± 4°	–	72
Hot embossing method	H13 mold steel template	Polytetrafluoroethylene (PTFE)	110.7° ±2.3°	–	Regular array of micro holes	25mm × 25mm × 1 mm	Depth-100 mm Diameter-24 mm	154.6°	5.5°	64
Hot imprinting	Dies with hierarchical	PTFE	111.9°	–	Patterned die	10mm × 10mm × 4 mm	Height-30 mm Radius-0.21 mm	158.5°	1.3°	62

process	patterns						Pitches-800, 640, 480 mm			
Hot imprinting	Dies with hierarchical	Polycarbonate (PC)	81.3°	-	Patterned die	10mm × 10mm × 4 mm	Radius-0.21 mm	157.8°	-	62
process	patterns	polymers					Pitches-800, 640, 480 mm			
Plasma etching	CF_4/Ar plasma etching	PMMA films	83°±2°	28°± 6°	Pillars	Area-175 mm	Width-400 nm	158° ± 1°	4° ± 1°	73
							Height-400 nm Pitch-1mm			
Plasma etching	CF_4/Ar plasma etching	Polyethylene	75° ± 6°	27°± 1°	Pillars	Area-150 mm	Width-400 nm	158 ± 2°	3° ± 1°	73

		terephthalate (PET) films					Height-400 nm			
							Pitch-1mm			
Plasma etching	CF_4/Ar plasma etching	Fluorinated ethylene	110° ± 2°	23°± 4°	Pillars	Area-125 mm	Width-400 nm	162° ± 1°	2°± 1°	73
		propylene (FEP) films					Height-400 nm			
							Pitch-1 mm			
Hot embossing	Ni shim	FEP films	112° ± 3°	31 ± 1°	Random micro-texture	30mm × 30 mm	–	156 ± 1°	8° ± 3°	54
Hot pressing	Al template	Polyether-ether ketone	73°	–	Prepreg surface	–	–	151.8°± 2°	4°±1°	74
process		(PEEK) composites								
Injection molding	anodic aluminum oxide	Fluorinated alkyl silane	118.9°	–	Hair-like nanopillars	25mm × 25 mm	Depth-5 mm	151.9°	–	75
process		(FAS-17) films					Pitch-450 nm			

	(AAO) template									
Hot embossing technique	Ni stamp patterned with a 2D array of square	Polytetrafluoroethylene (PTFE) films	102-104°	–	Chessboard-like structures	10mm × 10 mm	Length-2mm Width-2 mm Height-1.5 mm	145.5°	–	76
Hot embossing technique	Laser-engraved hard chrome stamp	PTFE films	102-104°	–	Chessboard-like structures	10mm × 10 mm	Length-2mm Width-2 mm Height-1.5 mm	112.6°	–	76
Hot embossing technique	Ni stamp patterned with a chessboard-like pattern	PTFE films	102-104°	–	Chessboard-like structures	10mm × 10 mm	Length-2mm Width-2 mm Height-1.5 mm	105.7°	–	76
		High-density polyethylene	–	–	Microfibrils	–		>160°	<5°	63

Hot embossing	Laser ablated SS						Pitch-18-50 mm			
technique	template	(HDPE)					Height-17-120 mm	>160°	<5°	
Hot embossing	Laser ablated SS	Polylactic acid (PLA)	–	–	Microfibrils	–				63
							Pitch-18-50 mm			
technique	template		80°				Height-17-120 mm	>160°	<5°	
Hot embossing	Laser ablated SS	Medical-PVC (polyvinyl		-	Microfibrils	–				63
							Pitch-18-50 mm			
technique	template	chloride)	79.9°				Height-17-120 mm	167°	2.5°	
Hot embossing	Si wafer	Cyclo-olefin polymer		–	Round pillars	Diameter-6,8 inches				69
							Diameter-15 mm;			

technique		(COP) (Zenor 1060R)					depth-20 mm			
Hot embossing	Si wafer	COP (ZF14-188)	87.6°	–	Round pillars	Diameter-6,8 inches	Diameter -20 mm; Depth-30 mm Diameter -15 mm;	154°	–	69
technique							depth-20 mm			
Injection molding	Micro-pillar arrays	Polypropylene (PP)	100°	–	Hair-like nanopillars	25mm × 25 mm	Diameter -20 mm; Depth-30 mm Depth-5 mm	152°	–	75
method							Pitch-450 nm			
Injection molding method	Micro-pillar arrays	Polycarbonate (PC)	80.3°	–	Hair-like nanopillars	25mm × 25 mm	Depth-5 mm, Pitch-450 nm	150°	–	75

2.4. The durability of surface-modified superhydrophobic surfaces (SHSs)

Wear tests, ball-on-disk sliding tests, linear and circular abrasions, water jet tests, and rubbing with cotton, cloth, sandpaper, or synthetic leather under various weights have all been documented in the literature to test the durability of SHSs for real-world applications [23].

2.4.1. Mechanical durability

Hardness, adhesion, flexibility, and impact resistance are most desired mechanical properties of SHSs [36]. On a Zr-based bulk metallic glass, an electrochemical method was used to build an SHS. It was observed that after surface modification, the obtained WCA was 154° ± 2°, and the CAH was 4° ± 2°. Further, to determine the mechanical durability of the modified surface, a sandpaper friction test was performed to check the abrasion resistance of the sample surface. The sample's abrasion resistance was determined using 2000 mesh sandpaper and 5 KPa load. The results obtained after some friction cycles were as follows: for 30 cycles of friction, the WCA was 150°, and for 70 friction cycles, the WCA was 135° ± 6°. It was clear that superhydrophobicity goes on decreasing with the increase of friction cycles, which created durability issues [72]. As a result, durability is a big concern for SHSs before their use in real-world applications. Gao et al. [44] fabricated hierarchical micro structured polytetrafluoroethylene (PTFE) films by using the micro-powder HE technique and obtained a maximum WCA of 164°, as well as CAH, which was 5.3°. For practical implementations, an abrasion test on homemade equipment was performed to investigate the mechanical durability. The sample was made to move vertically with 1000 g weight. On 1000 mesh sandpaper, approximately 100 cycles were performed.

The results were recorded after every 20 cycles. Almost every friction cycle produced the same results. The obtained WCA was greater than 150°, indicating that superhydrophobicity distortion was negligible. Thus, such kind of modified surface can be used practically in harsh conditions. Gong & He et al. [73] used polydimethylsiloxane (PDMS) film to create SHCs with a WCA of 156.4° and a CAH of less than 7°. The mechanical durability of the textured surface was investigated using a sand abrasion test. With 10 g of sand grains, a WCA of almost 156.5° was formed; with 30 g of a sand grain, a WCA of almost 155.6° was formed; and with 50 g of a sand grain, a WCA of almost 154.2° was formed. It was concluded that after a regular hitting of sand for 30 s, the microstructures were not destroyed, and the superhydrophobicity was also maintained. To test the coating's durability, approximately 5000 water drops were dripped from 50 cm above the coating for 2 h, and it was determined that the modified surface did not change and exhibited a WCA of 154.6°. Barz et al. [6] imprinted microstructures on polyurethane (PU) films by using a HE technique with a high pressure of 150 bar to achieve superhydrophobicity. Additional research was conducted on the durability aspects. Mechanical durability was tested using sand tricking with sand grains sized approximately 0.4-0.8 mm, and almost no change was observed in terms of WCA of the coating. In another study, Wu et al. [77] created a SHC using a CeO_2/PMMA/PVDF composite. The mechanical durability of this coating was tested using a sand abrasion method, and it had been discovered that there was a complete distortion of the superhydrophobicity as the WCA decreased from 152° to 103°. Fig. 2.25 depicts the surface morphology of CeO_2/PMMA/PVDF (composite coating) and carbon-reinforced CeO_2/PMMA/PVDF composite coatings after the sand abrasion test. However, after chopped carbon fibers were reinforced into this composite, it was discovered that the contact angle was greater than 140°, which shows superhydrophobicity was still distorted in this case as well. Fig. 2.26(a) depicts the WCA after carbon reinforcement into the composite and shows that there is only a minor influence on the hydrophobicity. A schematic of the chopped carbon fiber is illustrated in Fig. 2.26(b). As a result, the coating's durability must be improved.

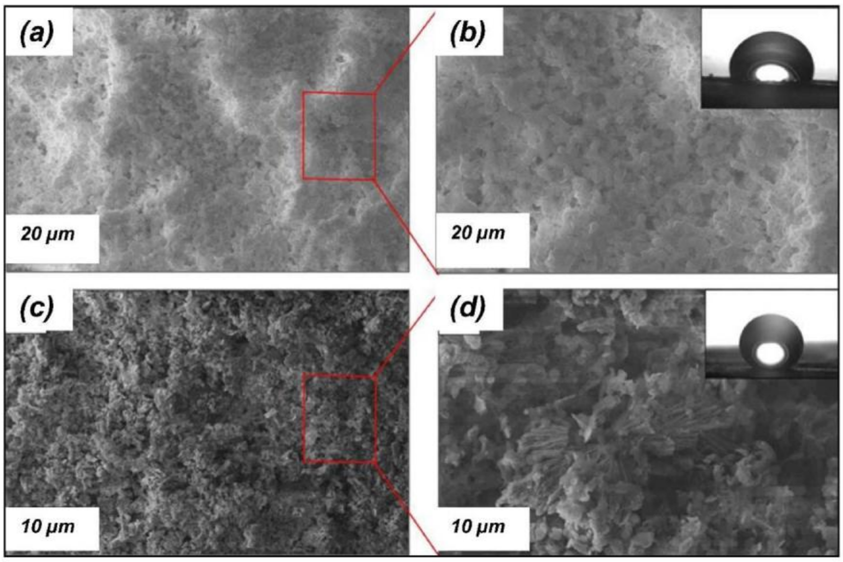

Fig. 2.25. SEM images after abrasion test (a, b) CeO_2/PMMA/PVDF coating, (c,d) carbon-reinforced CeO2/PMMA/PVDF coating (Reprinted with permission from Ref. [77], copyright © 2016, the Authors, Published by Atlantis Press).

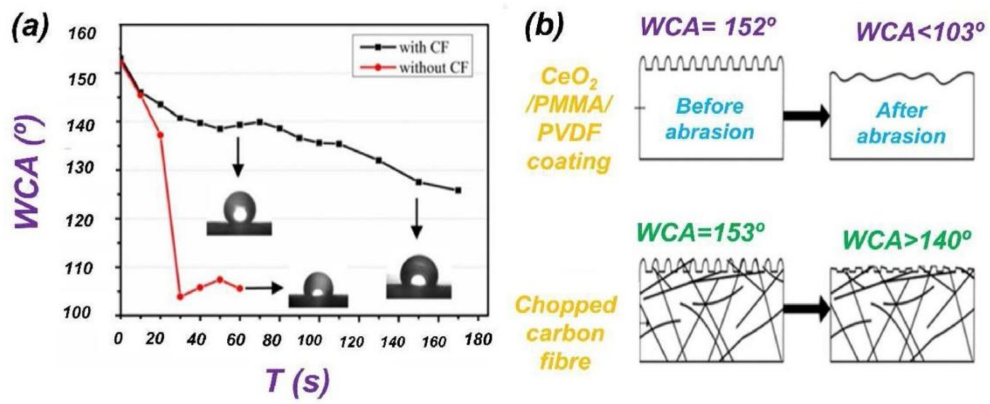

Fig. 2.26. (a) Water contact angle (WCA) after sand abrasion test describing the loss of superhydrophobicity, and (b) schematic of the chopped carbon fiber before abrasion and after abrasion (Reprinted with permission from Ref. [77], copyright © 2016, the Authors, Published by Atlantis Press).

2.4.2. Thermal stability

There are a large number of review papers available that cover the mechanical and chemical stability of embossed polymeric surfaces, but only a few describe thermal stability. For scientific research and applications, thermal properties should be considered, as they have a substantial impact on the micro- nanostructures of the embossed films. Gong et al. [64] discussed the thermal stability of embossed polytetrafluoroethylene (PTFE) films after keeping the embossed film in a tube furnace for 2 h and discovered that superhydrophobicity can last until the temperature reaches 340 °C. The WCA was evaluated at temperatures ranging from 100 °C to 340 °C. They discovered that with the rise in the temperature, the relative WCA decreased. The WCA at 100 °C was 154.3°, and at 340 °C, it was 152.6°, indicating that there is a little variation in WCA. Thus, the fabricated SHSs are good for heat resistance applications.

In another work, the ETFE-PANI/fCNTs-6 (composite coating's) thermal stability was tested using a thermal gravimetric tool, and it was discovered that the ethylene tetrafluoroethylene (ETFE) coating loses its anti-wettability characteristic after 500 °C. A graphical representation of the relationship between WCA and temperature is shown in Fig. 2.27, indicating that the coating becomes unstable after 460 °C when exposed to different temperatures for 2 h [78]. ETFE fluoromolds demonstrated the best combination of mechanical strength and thermal stability for imprinting at high temperatures and pressures. The researchers claimed that the ETFE mold could withstand the pressure of up to 55 bar. ETFE films have been utilized in a variety of industries to cover PVs due to their high light trans- mission coefficient of 85-95%. ETFE is well known for preventing water and vapor penetration.

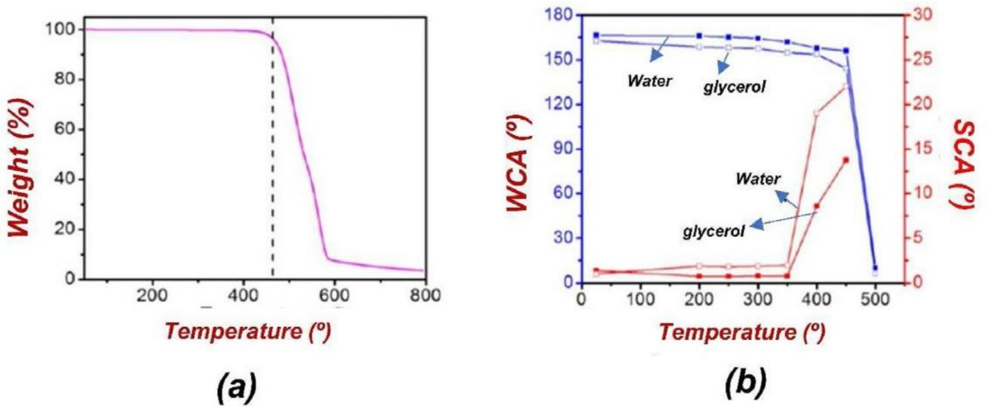

Fig. 2.27. (a) The TG thermogram and (b) wettability of an ETFE coating with a 6% content of PANI/fCNTs (Reprinted with permission from Ref. [78], Copyright © 2016, American Chemical Society).

In summary:

(a) The majority of research articles primarily focus on the manufacturing of SH surfaces. Only limited research articles addressed the issues of life and durability of the SH surfaces.

(b) There are multiple techniques available to evaluate the mechanical strength of modified surfaces; however, there are restrictions when it comes to thermal stability.
(c) Because of the lack of data on the thermal stability of modified SH surfaces, there is a tremendous opportunity to advance this field in near future.

2.5. Advantages of HE technique

The HE process is simple to use and produces high levels of precision. In comparison with other processes, HE technique produces significantly lower stresses in the material during embossing and has a substantially smaller operational temperature range [79]. The main benefit of adopting the HE approach is that it is widely applicable for various industries [80]. HE has excellent biocompatibility and adaptability in processing [81]. One of the best things about employing the HE approach is that polymers have shorter processing time since the glass transition temperature is lower than the melting temperature. As a result, the viscosity of the polymer is reduced, enabling substrates to readily construct the necessary hierarchical structures. This technique typically takes 4-15 min to complete the operation [44]. Fig. 2.28 is a schematic illustration of the potential merits and de-merits of the HE-assisted approach.

In summary:

(a) Although this approach is simple to use, the equipment must be protected from excessive heat.
(b) The most important factor is the holding period in between embossing and demolding stage. The surface quality of the hierarchical structures improves with increased holding time.

2.6. Limitations of HE technique:

The HE approach has several constraints such as the alignment of the re-entrant structures around the array of micro-nanoholes, which restricts the accurate replication of re-entrant structures [82]. Directly creating nanostructures on the surfaces of polymers is quite challenging. The other major drawback of the HE-assisted approach is the deformation of the photoresist-based structures due to a lack of proper parameter selection, which can include the wrong temperature, pressure, and many other factors. In the HE approaches, materials having rough surfaces are regarded as problematic during demolding. Because some polymers are stiff and have high melting temperatures, embossing them is exceedingly challenging. In case of generating complex structures using conventional machines, it is difficult to construct microstructures directly on the roller in the case of roller HE [49,83]. The main issue in HE is to find the ideal level of processing parameters to ensure the complete filling of the cavity on the embossing tool with the work material to obtain the maximum precision [29, 84, 87].

In summary:

(a) Replication of 3D complex re-entrant structures is challenging via HE-assisted approach.
(b) Directly generating nanostructures on the polymer surface is challenging.
(c) By combining hierarchical structures (dual micro-nanoscale assisted) with rough surfaces, there is a lot of potential for the future for producing superhydrophobicity directly on the surface of materials.

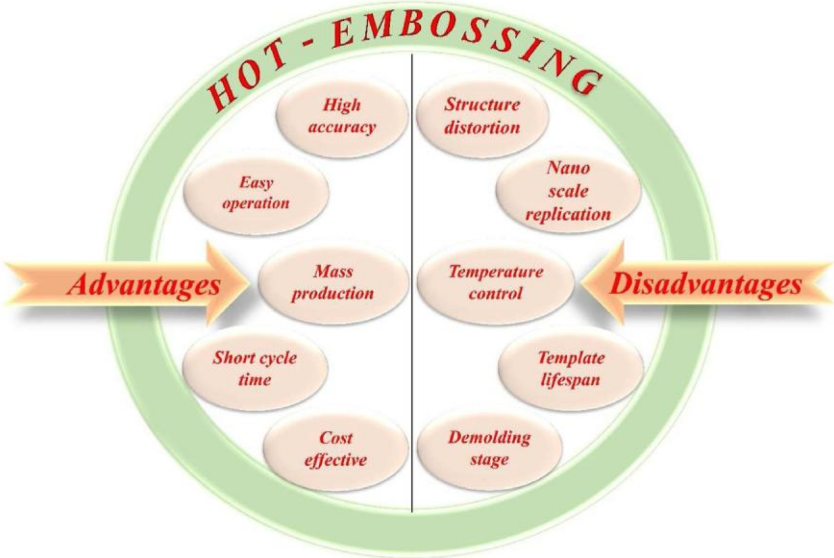

Fig. 2.28. Schematic illustration indicating the merits and de-merits of the HE approaches.

2.7. Applications of polymeric superhydrophobic surfaces (SHSs)

Polymeric materials-based devices manufactured by HE has a significant role in many fields due to the specified micro-nanostructures that provide a variety of unique features. There are also a number of reviews available for specific application [39] areas, including anti-frosting property [86, 87], energy emerging fields [88], self-cleaning [11, 89-91], anti-corrosion [92-94], anti-icing [95-96], oil-water separation [97-99], drag reduction [100-102], anti-fogging [103-105], biomedical application, etc. [106-108]. Fig. 2.29 shows the potential application of polymeric based SHSs that includes various areas like automotive, medical devices, aerospace, marine, solar panels, and microfluidics. Other environmental factors have significant influences on the superhydrophobicity [109]. For optical properties of PV devices, one of the major issues on the surface of a solar panel is dust accumulation, which reduces the efficiency of solar cells. During the day, dust builds on the solar panel's surface, and at night, dew forms, resulting in the development of mud when the dust and dew combine. As a result, a self-cleaning surface is required to maintain the efficiency of solar panels because if dew falls on a surface where dust has accumulated, it will roll off the surface if the surface is superhydrophobic. Roslizar et al. [54] demonstrated a fabrication process using HE for creating different micro-textures on a fluorinated ethylene propylene (FEP) film that is incredibly transmissive and photostable for the application on PV modules. A 127 mm thickness FEP film was textured using HE, yielding a WCA of 156° ± 1° and a CAH of 8° ± 3°. The influence of HE forces and temperature on wetting properties was investigated using WCA and CAH. Furthermore, FEP films are more expensive than other polymer films, even though they have more benefits. However, the same could be said about other polymer films for different applications. Vullers et al. [110] manufactured superhydrophobic transparent coatings for optoelectronic devices. A hybrid of hot-pulling and HE techniques was employed to fabricate the nanofur surfaces fabricated from optical grade PC film. After surface modification, a WCA of 166° ± 6° was observed, which when coated on PV devices resulted in more than 85% transmission, yielding a notable increase in optical device efficiency. In addition, Patil et al. [111] performed bacterial tests on the embossed polystyrene film, and it was discovered that grooves with a width of 0.5 mm (dimensions smaller than the size of bacteria) significantly reduced bacterial adhesion which has a great potential for the application of anti-biofouling as the surface prevents attachment of bacterial components. Ferrari et al. [112] studied the self-cleaning capability of SH surfaces while simulating the influence of continuous water droplets and dust particles and pollution agents such as acid rain. Using a simple spray method, a SH coating with WCA >170° that contains a silica and fluoropolymer blend was prepared. As a result, the developed SH coating's exhibited high transmittance. This kind of technology can be employed for commercial optical devices like solar panels, automotive, medical devices, and other things. Minegishi et al. [34] created a porous layer of PDMS on the top of silicate glass to create hierarchical nanoporous layer (HNL) using a simple chemical vapor deposition (CVD) method. The PDMS-treated clean glass has a WCA of roughly 140°. These kinds of coating techniques can be used in optical devices to improve light transmittance and anti-reflectivity.

In summary:

(a) There are numerous techniques available for manufacturing SH surfaces, but the appropriate technique should be used as per the requirement of the targeted application.

(b) There are reviews available in the field of anti-icing and anti-corrosion applications, but only a few provide clarity regarding the production of polymers-based SH surfaces via HE technique for optical devices, such as Fresnel lenses, microlens array, and many others.

(c) The main issue with SH surfaces is their durability and longevity, which presents a significant production problem at industry scale.

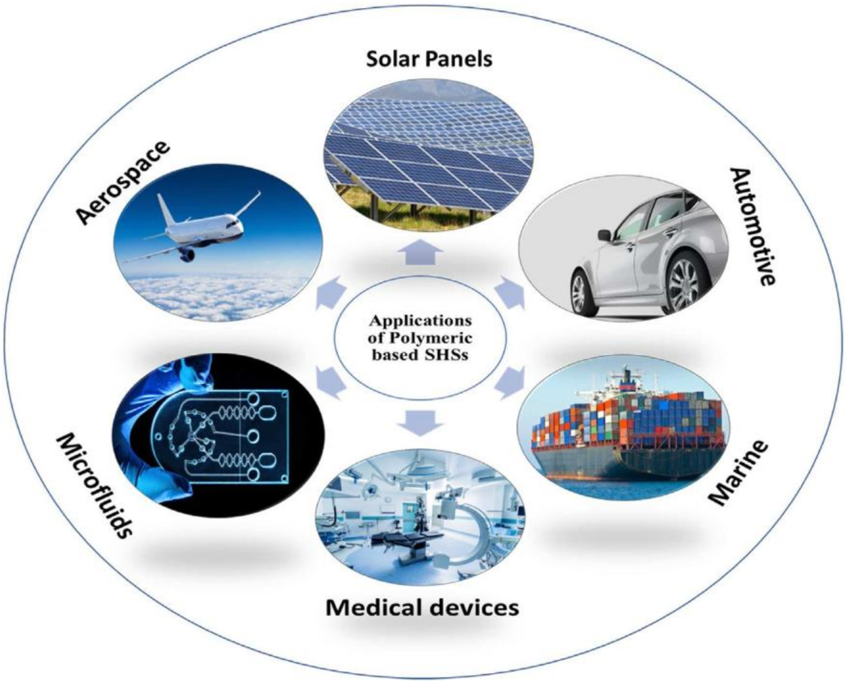

Fig. 2.29. Potential applications of polymeric-based superhydrophobic surfaces (SHSs) [39].

2.8. Current challenges and future recommendations

Researchers have made significant efforts to investigate several fabrication techniques for achieving highly precise nanorough- ness on the surfaces to achieve superhydrophobicity [113]. There are still issues that can be resolved, such as the evaluations of long-term environmental consequences and large-scale production at an affordable price [114]. The key issue is to choose the right materials for individual applications and strike a balance between embossing and de-embossing by manipulating the coating's micro-nanofeature. Finally, an issue develops when the study approach reaches the application stage; therefore, the solution is to address the aforementioned challenges to cover the application stage as well. Deformation and distortion of microstructures occur during the de-embossing step of a HE process when a flexible mold is used. As a result, different polymers/ substrates require varied rolling pressures, temperatures, and speeds. The stiffness and viscosity of the thermoplastic polymer

substrate significantly reduced after a temperature rise of greater than 140° during the HE processes, owing to deformation in the polymer chains. There are also obstacles to transferring hierarchical microstructures and nanostructures patterns onto a polymer substrate on a large scale for real-world applications. As a result, future research should concentrate on the manufacturing of large-scale area stamps that may be employed in real-world applications.

2.8.1. UV-light irradiation resistance

Jafari et al. [115] reported the problem with 3D printing of SHSs. Most of the materials used in high-precision 3D printers do not have very low surface tension. The procedure is dangerous for complex geometries because the coating must not fill nanoscale asperities. Abrasion or loss of adherence to the substrate can also cause the coating to deteriorate. Many research articles on super- hydrophobicity and anti-reflective coatings have been published. There is also some study on superhydrophobic anti-reflective solar panel materials that can be found. However, they have not addressed the durability of the coatings which is a major concern from a commercial point of view. If we talk in terms of applications of fabricated coatings, solar panels that have been soiled reduce the conversion efficiency to about 50% by reflecting light [116]. Therefore, this area has the potential to boost the popularity of polymer films with advanced solar panel technologies for which hierarchical patterns can be fabricated via HE technique without any distortion in the topographical structures. As a result, research should be proposed to improve the superhydrophobicity and durability without compromising transparency in polymers for solar panel application to increase the longevity and stability of super- hydrophobic covering in solar panels because a polymer-based coating is modified with low-energy materials can reduce dust deposition significantly. Oliveira et al. [117] mentioned four strategies, water-blowing method, air-blowing method, robotic method, and ultrasonic vibration method to expel dust contaminants from the surface of a solar panel. However, such type of techniques demands the use of a power system to clean the surface of the solar panel, which is not cost-effective. Therefore, fabricating robust hierarchical micro-nanostructures is a crucial challenge in terms of future aspects for real-world application. Apart from soiling, reflectivity and coating durability are additional significant factors to consider that have a substantial impact on solar energy conversion efficiency. As a result, self-cleaning solar panels are very important nowadays. The poor influence of reflection and soiling on solar panel power conversion efficiency (PCE) leads us to cover them with antireflective and SHCs, as previously stated. Even on top of coatings, the problem of chemical and mechanical durability in severe environments limits their practical application. The followings are a few reasons for this behavior: (1) nanoparticle assembly is the major fabrication process which results in poor adherence to the substrate [118]; (2) acid/alkali environment, increased scratching, high temperature, abrasion, and UV-light irradiation cause decline in WCA due to topographical structure destruction [48].

2.8.2. Fabricating topographical structures

Previously, hierarchical micro-nanoparticles have little adherence to the substrate and can easily peel away from it after being mechanically or chemically destroyed. As a result, fabricating durable superhydrophobic topographic structures is very essential. However, these extremely complicated operations take a long time to complete. Furthermore, the most difficult technique for pattern replication is lithography, but due to its complicated procedure, its implementation on an industrial scale is extremely difficult [119]. Chen et al. [120] created a self-healing SHS with polystyrene (PS), fluorinated silicondioxide (SiO_2) nanoparticles, low surface energy agents, titaniumdioxide (TiO_2) nanoparticles, and among other materials. When mechanical abrasion destroyed the micro-nanostructures, photocatalysis of TiO_2 nanoparticles under UV- light irradiation was used to renew the roughness and retain superhydrophobicity. Shape-memory polymers are also capable of fabricating mechanochemically durable and self-healing SHSs. As a result, improving steadiness, longevity, and physical/chemical properties is crucial [121]. For PV panel applications, transparency and superhydrophobicity of polymer films are competitive, and they are further affected when durability comes into picture. As a result, maintaining the antireflective and superhydrophobic properties of the films for longer periods is critical for their practical uses. By using HE with some other techniques, a balance between super-hydrophobicity and transparency can be formed which can resolve the primary problems and thus open up new pathways to explore. We believe that the investigation of the role of topographical structures on the superhydrophobicity of SHSs has a long way to go. Researchers need to create more simpler and powerful tools for producing SHSs useful for practical applications.

In summary:

(a) There is a need for in-depth investigation that focuses on polymer-assisted complex re-entrant structures utilizing the HE technique.

(b) An ideal study should comprise the physical understanding that establishes the correlation between micro-nano protrusions and the water droplet to understand basic wettability phenomenon.

(c) For a better understanding of superhydrophobicity, extensive research should be conducted that takes both the surface roughness and transparency variables into consideration.

2.9. Summary

In this study, we provided an overview of superhydrophobicity based on the HE technique. This review focuses on the most commonly used polymers in surface templating topography using the HE method. A basic explanation of the processes and the various geometrical micro-nano shapes that can be used in a variety of situations are covered. A comparison of the WCA and CAH of various polymers used for surface modification is also provided. Finally, the difficulties and prospects for the future are concluded. However, to address the demands of real-world applications, the proposed theory-based wetting models must be improved for a better physical understanding of the superhydrophobicity mechanism as theoretical analysis and system performance are not well established. Future research should focus on low-cost methods for creating better SHSs based on geometrical parameters on large- scale arrayed micro-features. Polymer-based SHSs must be improved in terms of mechanical, thermal, and chemical durability, which is essential for many applications.

CHAPTER 3. LITERATURE SURVEY: THEORETICAL ASPECTS

3.1. THEORY OF WETTING SURFACES AND MODELS

Superhydrophobic surfaces exhibit low contact angle hysteresis (CAH) with values below 10° and water contact angle (WCA) greater than 150° [122-127]. The superhydrophobicity can be obtained through the combination of micro/nano hierarchical structures on a surface [128-129]. The naturally acquired superhydrophobic characteristics are attributed to the combination of micro/nano hierarchical rough patterns and the surface energy as low as 26 mJ/m^2. A surface with low energy is crucial for achieving superhydrophobicity, so that a water droplet on such surface becomes spherical to minimize its energy and create a desirable liquid–air interface. The surface roughness equally plays an important role in achieving superhydrophobicity [130]. The wettability of a surface can be easily accessed by measuring the WCA [131-132]. The WCA on a surface demonstrates the wet ting regime of that surface. Usually, a droplet of water results in a high contact angle (CA) for surfaces of uniform roughness and a low CA for smooth surfaces [133-137]. The CA is also influenced by the size, weight, and height of the droplet falling on the substrate. The understanding of the impact of surface texturing and structural characteristics on superhydrophobicity is incomplete despite the implementation of multiple techniques to manufacture artificial superhydrophobic surfaces. Initially, three wetting models such as Young's, Wenzel, and Cassie–Baxter were developed to explain the surface wetting behavior [138-140]. Over the time, different wetting states were studied by different structural elements and contact angle prediction models. The wetting state connects structural factors to the wettability conditions [141]. The Young's equation is a fundamental and elementary wetting model that was proposed in 1805. This model explains the thermodynamic equilibrium between the liquid, vapor, and solid phases by assuming homogeneous solid sur face conditions and the creation of contact lines by each of the three interfaces to minimize the surface area [142]. Additionally, the surface is assumed to be fully rigid, ideal, and flat during the development of Young's equation. Two examples of surfaces that deviate from the ideal state are considered here: rough and smooth surfaces that are still considered real (finitely rigid). The Young's equation for a balanced droplet in the horizontal direction is demonstrated as shown in Fig. 3.1 (1) using the mechanical equilibrium condition Eq. (3.1).

$$\cos\theta_{eq} = \frac{\gamma_{SV} - \gamma_{SL}}{\gamma_{LV}} \tag{3.1}$$

where θ_{eq} is the equilibrium contact angle in Young's model [143-145], which is also known as the intrinsic angle of a solid surface. According to Fig. 1, γ_{SL} , γ_{LV} and γ_{SV} represent the interface surface tensions of solid–liquid, liquid–gas, and solid–gas, respectively.

Most surfaces were rough, which limits the use of Young's model in assessing wetting qualities. The surface roughness and other factors have a significant impact on wetting [146-147]. The Wenzel model [148] was introduced in 1936 and is based on the assumption that liquid droplets are uniformly in contact with the surface and can enter the micro-/nanogrooves of the textured surface, as shown in Fig. 3.1 (2). The surface composition is assumed to be uniform. The Wenzel equation is mathematically represented as

$$r_f(\gamma_{SV} - \gamma_{SL}) = \gamma_{LV}\cos\theta_W \tag{3.2}$$

where θ_W is the Wenzel contact angle, which establishes that the contact angle is influenced by the surface roughness and is represented by Eq. (3.2). Component r_f is assigned to the roughness factor in this instance because the Wenzel model shows a correlation between the contact angle and surface roughness. Consequently, the improved Wenzel equation is given by Eq. (3.3):

$$\cos\theta_w = r\cos\theta_y \tag{3.3}$$

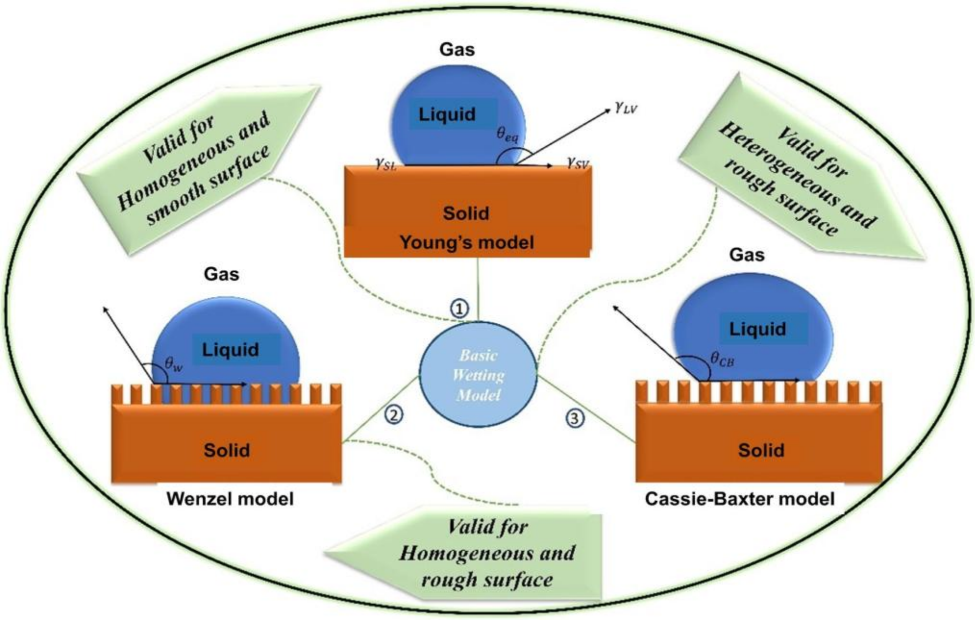

Fig. 3.1. Schematic illustration of contact angle at equilibrium on a surface with three phases: solid–liquid, solid–gas, and liquid–gas.

The physical relevance of this model lies in its ability to represent wetting conditions on a uniform interface using the WCA, which is determined on a rough surface. The homogenous state of any surface is the only scenario for which the Wenzel model is appropriate. Consequently, the Cassie–Baxter model [149], which is perfect for the heterogeneous condition of any surface, has been developed. The prototype for this design was significantly improved in 1944, as demonstrated by Eq. (3.4).

$$\cos\theta_{CB} = F_S(1 + \cos\theta_Y) - 1 \tag{3.4}$$

where θ_{CB} indicates the contact angle of the Cassie–Baxter model, F_S indicates the interaction between the solid fraction and liquid droplet, and Y is the Young's contact angle. The reason why the liquid does not make complete contact with the surface in this state is due to the presence of air pockets underneath, as demonstrated in Fig. 3.1 (3). A drop of liquid cannot penetrate these air pockets because the dimensions of the micro-structure are smaller than that of the droplet [150]. It is evident from the three main wettability models that a low surface energy and rough surfaces are crucial for the generation of superhydrophobic surfaces. Artificial superhydrophobic surfaces have the potential to revolutionize various industries by providing solutions to long-standing challenges. For instance, self-cleaning sur faces can greatly reduce the need for manual cleaning and maintenance in industries such as automotive, aerospace, and architecture, leading to cost savings and increased efficiency. Anti-icing surfaces can improve safety in transportation by preventing ice accumulation on aircraft wings, road signs, and power lines. Additionally, drag reduction and anti-corrosion properties can enhance the performance and longevity of marine vessels and infrastructure. By exploring the theoretical concepts of wetting regimes, this review contributes to the development of more effective and versa tile superhydrophobic surfaces that can have a wide-scale impact. Although significant progress has been made in the three basic wetting models, there is a need of further research on the development of surface properties of a non-wetting surface. The literature lacks a physical theory to explain the connection between the hierarchical structures of surfaces and the

CA. The wetting models must be continuously revised and improved. This review is much needed for determining the WCA on micro-/nanotextured surfaces using both fundamental and innovative approaches in a static configuration. The most recent developments in the wetting transitional regimes for various surfaces are discussed in this review. Additionally, droplet dynamics on advanced functional surfaces has been investigated using theoretical and experimental approaches followed by the researchers.

3.2. Wetting model depending on various factors.

Behera et al. [151] presented a model for the wetting of abraded composite materials. This model explains the relationship between contact angle, micro-structure, and corrosion and could be utilized to develop materials with corrosion-resistant micro-structures and higher contact angles. The researchers assumed that the matrix roughness component was identical to that of the complete composite. The symmetrical arrangement of sandpaper with sand particles caused semi-circular parallel scratches on the sur face of sample. These scratches facilitated the determination of the theoretical roughness factor for the composite due to abrasion. Figure 3.2a indicates that 2R represents the depth of the scratch, and D signifies the diameter of the abrasive particle, which is also the distance between two consecutive scratches λ. Figure 3.2b illustrates the impact of droplet volume on the apparent contact angle of ductile iron samples. In Fig. 3.2c, theoretical models for contact angle are presented as a function of increasing graphite volume, including (a) the Wenzel model and (b) the Cassie–Baxter model. To determine the Wenzel roughness factor R_{f-w}, Eq. (3.5) can be used, which is based on the length L of the scratches.

$$R_{f-w} = \frac{true\ area}{projected\ area} = \frac{(2a+\frac{\alpha D}{2})L}{DL} = \frac{2a}{D} + \frac{\alpha}{2} \quad (3.5)$$

where the diameter of abrasive particles is represented by *D*, while the geometrical parameters that are influenced by the depth of scratches are denoted by 'a' and 'α.' Furthermore, the Cassie–Baxter model is explained in terms of the abrasion-related roughness factor in Eq. (3.6). When the top part of the surface was in contact with water, the projected and true contact areas were equal.

$$R_{f-CB} = \frac{true\ area}{projected\ area} = 1 \tag{3.6}$$

The authors investigated whether the phase fractions of the micro-structures influence the corrosion characteristics or not. Experimental evidence has confirmed that pearlite is more prone to corrosion compared to both graphite and ferrite and an increased amount of pearlite within the micro-structure can have adverse effects on the corrosion resistance of material. The relationship between corrosion, contact angle, and micro-structures offers insights for the development of materials featuring corrosion-resistant micro-structures and enhanced contact angles. They found that the graphite fraction in ductile iron can increase the contact angle due to the lower energy surface of ductile iron compared to the matrix. Despite the changes in droplet size and contact angle, the ductile iron system adhered to the Wenzel wetting regime.

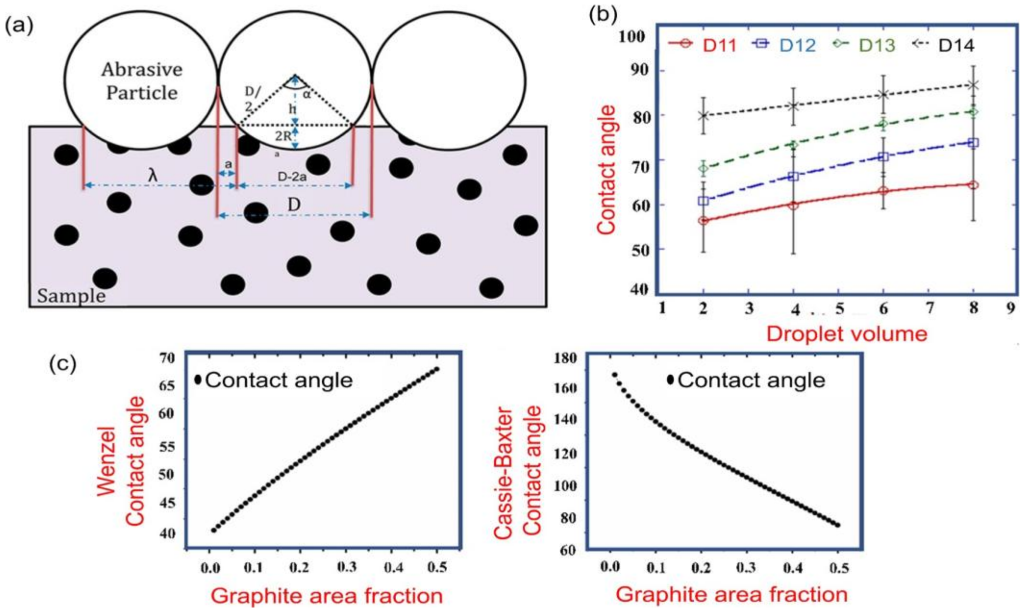

Fig. 3.2 (a) Diagram of the abraded surface, (b) effect of droplet volume on sample, and (c) theoretical representation of the contact angle with increasing graphite concentration: for Wenzel and Cassie–Baxter models (reprinted with permission from the American Chemical Society, Copyright © 2019, Langmuir [151].

In another study, Majhy et al. [152] provided analytical modeling and a theoretical understanding of the wetting stability and dynamic behavior of water droplets resting on superhydrophilic spots of horizontal superhydrophilic–superhydrophobic surfaces. The procedure for creating the superhydrophilic–superhydrophobic surface is outlined in Fig. 3.3. The physical evolution of the contact angle and diameter of the droplet were investigated. The researchers analyzed the moisture absorption of a droplet by placing a 0° superhydrophilic patch surrounded by superhydrophobic regions on their superhydrophilic–superhydrophobic composite surface. Figure 3.4 (1) depicts the pictorial flow of liquid into micro/nanoscopic grooves on a superhydrophilic surface, leading to the rapid dispersion of the contact line. As shown in Fig. 3.4 (1, a), different droplet sizes and shapes can be observed on a superhydrophilic spot with varying Bond number (B_0) values. For instance, a small droplet assumes a spherical cap shape as shown in Fig. 3.4 (1, b), while a droplet with $B_0 < B_{0_{cr}}$ has an oblate spheroid shape as shown in Fig. 3.4 (1,c). In Fig. 3.4 (1, d), various forces acting on a liquid mass close to the contact line are illustrated. Conversely, a large droplet with $B_0 > B_{0_{cr}}$ has an oblate spheroid shape as shown in Fig. 3.4 (1, e). The results revealed that the contact line pinning and gravity forces controlled the stability of the droplet. Figure 3.4 (2) presents experimental images of droplets with varying volumes on the superhydrophilic–superhydrophobic surface, providing visual representations of the contact line diameter and contact angle. The surface inclination angle, liquid characteristics, and drop let volume are collectively expressed in Eq. (3.7) based on the Bond number (B_0), which determines the final configuration when the superhydrophilic spot size is fixed.

$$B_0 = \frac{\rho^* g V^*}{\gamma_{LV} \pi d_s \cos\theta^*} \tag{3.7}$$

where V^* and θ^* denote the volume of the droplet and static contact angle for a fixed volume, respectively; γ_{LV} and ρ^* represent the surface tension and liquid density, respectively, whereas d_s and g are the superhydrophilic spot diameter and gravitational constant. Gibbs free energy (G) can be expressed by Eq. (3.8) when the surface and gravitational energies are considered.

$$G = \gamma_{LV} S + \pi (R \sin\theta^*)^2 (\gamma_{SL} - \gamma_{SV}) + \rho^* g H V^* \tag{3.8}$$

where the oblate spheroid droplet has a surface area, *S*, and centroid, *H*, and γ_{SL}, γ_{SV} , and γ_{LV} denote the surface tension values at the solid–liquid, solid–air, and liquid–air interfaces, respectively. R is the radius of curvature. To satisfy the minimum energy conditions, the term *dG =0* tends to zero because *G* is only a function of θ^*. Equation (3.9) is used to measure the droplet diameter at droplet volume $B_{0_{cr}}$

$$\frac{4\rho^* g(1-\cos\theta^*)}{\sin\theta^*} = D[\frac{2\pi\gamma_{LV}k_1}{\cos\theta^* sin^2\theta^*} + \pi(\gamma_{SV} - \gamma_{SL})] \tag{3.9}$$

Here, $k_1 = 1 - \frac{cos^3\theta^*}{2\sqrt{1+cos^3\theta^*}} ln \frac{1+\sqrt{1+cos^3\theta^*}}{1-\sqrt{1+cos^3\theta^*}}$

According to the spot diameter ds and Bond number (B_0), three separate regimes were identified: spherical cap, oblate spheroid (fixed d_s with varying θ^*), and oblate spheroid (varying d_s with fixed θ^*). The regulation of contact angle, drop let curvature, and diameter can be adjusted independently according to the wetting regime, which may be beneficial for the fabrication of micro-lenses. Furthermore, it is expected that the results of this study will encourage the development of droplet micro-fluidic-based biological applications on accessible surfaces.

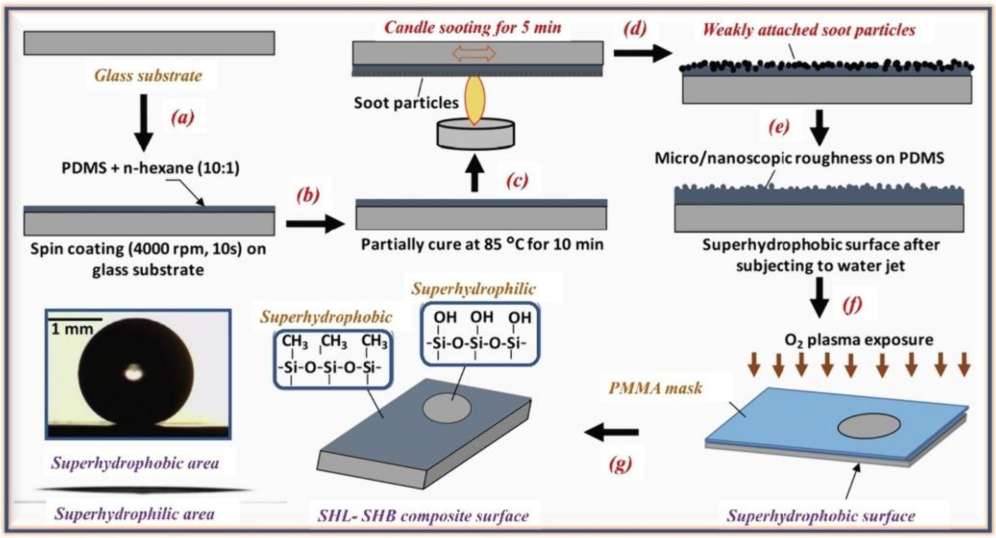

Fig. 3.3 Pictorial representation of the fabrication process of superhydrophilic–superhydrophobic (SHL–SHB) surfaces (reprinted with permission from the Journal of Colloid and Interface Science, Copyright © 2020, Elsevier [152]).

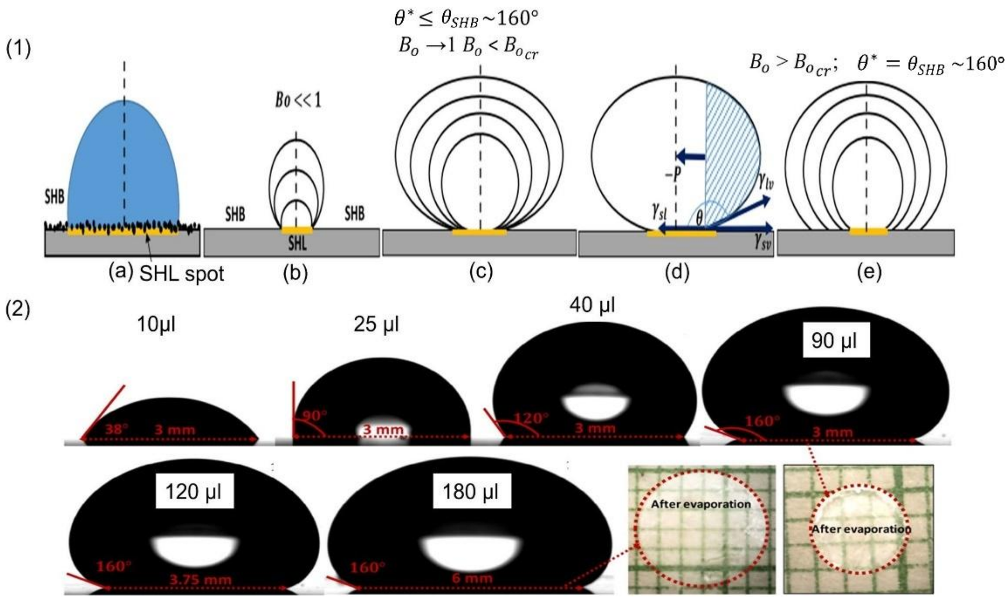

Fig. 3.4 (1) (a) Schematic illustration of a capillary movement of liquid into superhydrophilic surface with extremely small grooves; (b) a spherical droplet on the superhydrophilic spot with $B_0 \ll 1$; (c) a droplet of medium size with $B_0 \to 1$ and $B_0 < B_{0_{cr}}$); (d) oblate-shaped spheroid; and (e) a large oblate-shaped

spheroid droplet with (i.e., $B_0 > B_{0_{cr}}$). (2) Experimental pictures of droplets on the superhydrophilic–superhydrophobic surface with varying volumes (reprinted with permission from the Journal of Colloid and Interface Science, Copyright © 2020, Elsevier [152])

In another theory, Starinskiy et al. [153] investigated the transition of wetting regimes from superhydrophilic sur faces to hydrophobic surfaces. They performed a nanosecond laser treatment followed by the deposition of a fluoropolymer. The experimental setup is shown in Fig. 3.5a. The wettability of the silicon surface was controlled by varying the water contact angle, which ranged from 0° to 170°. Using the Cassie–Baxter and Wenzel theories, they examined the wettability characteristics of the developed fluoropolymer–silicon combination. For laser-treated smooth surfaces, the essential thickness of the fluoropolymer is 35 nm. A typical micro-structure in the cross-sectional SEM image with height 'b^*' and half-width on silicon with a laser-treated surface is shown in Fig. 3.5b. The regular and closely packed cones on the laser-treated surface that were submerged in water were their peaks, while the surrounding gaps were air pockets. The liquid configuration of the Cassie–Baxter state on this surface is shown schematically in Fig. 3.5c. The Cassie–Baxter equation for this situation is given by Eq. (3.10).

$$\cos\theta_w = \frac{\pi l w \cos\theta_Y}{4a^{*2}} + \frac{a^{*2} - \frac{\pi a^{*2}}{4}}{a^{*2}} \cos\theta_{CB} - \frac{\pi(a^* + w)(\sqrt{a^{*2} + b^{*2}} - 1)}{4a^{*2}} \quad (3.10)$$

Here, $\frac{w}{l} = \frac{a^*}{\sqrt{a^{*2} + b^{*2}}}$ is defined as proportionality constant, where 'a^*' is the half-width, 'b^*' is the height of a micro-structure, 'r_f' is the roughness value, θ_Y represents the contact angle of a smooth surface, θ_{CB} denotes the Cassie state, and θ_w denotes the Wenzel state. The following are the boundary conditions when the wet surface approaches the patterned surface:

$$w \rightarrow a^*, l \rightarrow \sqrt{a^{*2} + b^{*2}}\ and\ \theta_{CB} \rightarrow \theta_Y$$

Therefore, the Cassie–Baxter wetting regime transforms into Wenzel wetting regime, as shown in Eq. (3.11):

$$\cos\theta_w = \frac{\pi a^* \sqrt{a^{*2}+b^{*2}+4a^{*2}-\pi a^{*2}}}{4a^{*2}} \cos\theta_Y \qquad (3.11)$$

The Wenzel hypothesis was found accurate for all reported apparent contact angles of the laser-modified surface in the presence of a fluoropolymer coating. As shown in Fig. 3.5d, the water contact angle varies with the fluoropolymer deposition. Further, as shown in Fig. 3.5e, the cosine value of the contact angle depends on the thickness of the fluoropolymer. Therefore, a mathematical model is needed that can correlate with the geometrical parameters and is consistent with the Cassie–Baxter state, as every mathematical model currently available is consistent with the Wenzel theory.

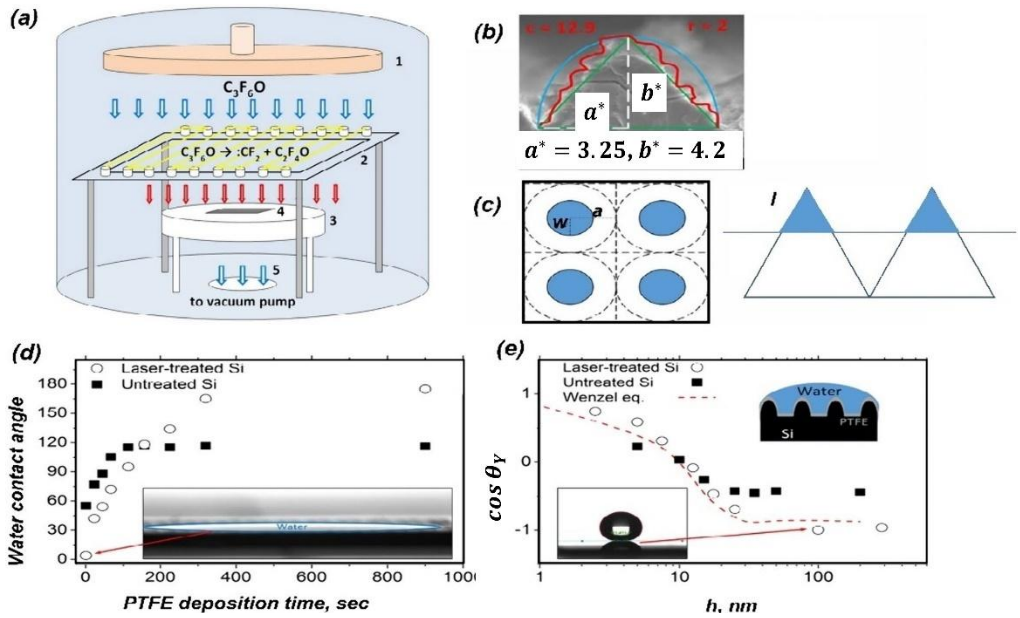

Fig. 3.5 (a) Experimental part with the following sub-assemblies: (1) uniform precursor gas flow, (2) a wire activator, (3) a substrate holder, (4) a silicon substrate, and (5) a vacuum pump; (b) SEM cross sectional picture of micro-structure; (c) pictorial representation of two shapes, a semi-ellipsoid and a cone, are utilized to calculate the roughness factor *r*; (d) dependence of the WCA of fluoropolymer deposition; and (e) cosine of the WCA depending on the fluoropolymer's thickness (reprinted with permission from the Journal of Physics D: Applied Physics, Copyright © 2018, IOP Science [153]).

Cheng et al. [154] developed a theoretical wetting model to calculate the contact angle (CA) for various surface geometries and wetting states. As shown in Fig. 3.6a, the energy of the drop on the surface is depicted. The authors assumed that the potential drop radius F could be expressed in terms of 'h_1' and V. To make the surface energy solely dependent on the WCA, a constant volume was assumed. Figure 3.6b illustrates an idealized scenario for rough surface texturing, where 'b_1' represents the cylinder top diameter, 'h_1' is the pillar height, and L_1 is the distance between pillars. Equation (3.12) shows that a flat surface has a specific surface energy.

$$E = \gamma^1 (A_c - \cos\theta_0 A_p) \quad (3.12)$$

where A_c and A_p signify the drop's cap and projection area. Young's contact angle and surface tension are denoted by θ_Y and γ^1.

The final calculation is derived from Eq. (3.13).

$$cos\theta_Y = (f_w'(r_w' - \varphi^1)+\varphi^1)C_1 - (1 - f_w')(1 - \varphi^1) \quad (3.13)$$

Where r_w', φ^1 and f_w' signify the following: the ratio of the roughness, the ratio of the solid–liquid area to the projection area, and the projection area fraction of the wetted surface that is covered by liquid.

Here,

$$C_1 = \cos\theta_Y + \cos\theta_E' - cos\theta_Y + \frac{1}{2}sin^2\theta(\cos\theta + 2) \quad (3.14)$$

where θ_E' is the equilibrium contact angle. Equation (3.14) can be used to determine the maximum or minimum angles for the Young's contact angle and known surface geometries. The surface energy profile can vary based on the pillar design and spacing. As shown in Fig. 3.6c, d, and e, the energy surface profile changes for different contact angles when θ = 60°, θ = 90°, and θ = 120°, with b_1 = 1 µm, h_1 = 2 µm, and L_1 = 3 µm. At θ = 90°, the authors discovered that CAH increased with increasing roughness for all values of the wetting ratio, f_w' owing to the presence of a larger contact area with the droplet. For all f_w' values, CAH decreased as the roughness increased at θ = 120°. This suggests that CAH is lower in Wenzel state. According to the modeling results, CAH increased as the wetting level increased. Additionally, CAH remained low for both low and high droplet contact angles, regardless of whether the sur face was hydrophobic or hydrophilic. To better understand the Cassie–Baxter state, further modeling improvements are required.

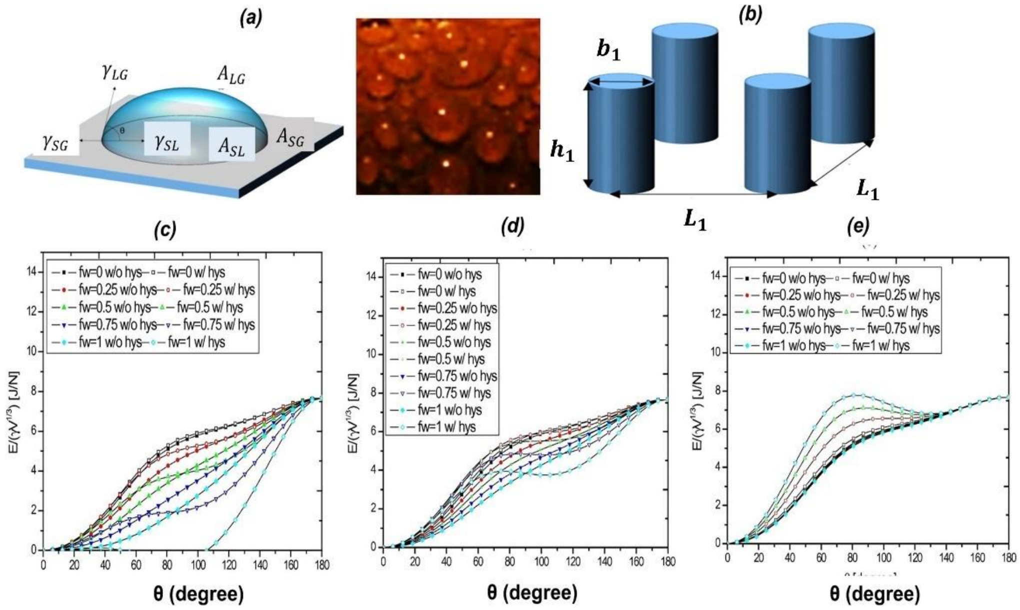

Fig. 3.6 (a) Illustration of three dimensions of the surface energy and water condensation on a sub-cooled copper surface; (b) an idealized depiction of surface roughness, with diameter equal to b_1, height equal to h_1, and separation distance equal to L_1; surface energy profiles (c), (d),

and (e), respectively, for $\theta = 60°$, $\theta = 90°$, and $\theta = 120°$, where $b_1 = 1$ μm, $h_1 =$ 2 μm, and $L_1 = 3$ μm (reprinted with permission from International Journal of Heat and Mass Transfer journal, Copyright © 2016, Elsevier [154])

Sudeepthi et al. [155] outlined the transitional wetting regime between the Wenzel and Cassie–Baxter theories for a nanostructured surface caused by acoustic waves. To create an acoustic wave effect in the experimental part, the device was fabricated by placing the electrodes of an inter digitated transducer (IDT) on a lithium niobate ($LiNbO_3$) substrate. The substrate was coated with silica nanoparticles with an average diameter of 30 nm and then heated for 60 min at 110 °C to improve the adherence of the coating. Figure 3.7a depicts the diagram of the experimental configuration, and Fig. 3.7b depicts the illustration of the droplet in the Cassie–Baxter state (prior to acoustic wave application) and Wenzel state (following acoustic wave application). A SEM image showing hierarchical micro-/nano roughness is presented in Fig. 3.7c. While nanoscale roughness results from aggregated nanoparticles, micro-scale roughness is caused by the size of individual particles. The calculated contact angle of 152º validates the superhydrophobic wetting regime. Figure 3.7d demonstrates the transition from the Cassie–Baxter to the Wenzel wetting regime under the influence of acoustic waves. This occurs because the liquid rests on tiny protrusions formed from nanoparticle clustering in the Cassie–Baxter state, which has a hierarchical structure of surface roughness. Conversely, the area fraction increases when the liquid in the Wenzel condition is entirely immersed in the hierarchical grooves. The Rayleigh angle, defined as the ratio of the drop’s sound velocity to the surface acoustic wave phase velocity in $LiNbO_3$, is formed when the acoustic waves are allowed to pass through the substrate–liquid interface. Figure 3.7e displays the transition from Cassie to Wenzel wetting for drops of varying volumes subjected to surface acoustic wave excitation at different frequencies and input powers. In Fig. 3.7f, the final contact angle of the drops is presented, reflecting a range of experimental data involving changes in drop volume, applied frequency, and input power. Equation (3.15) describes the acoustic wave energy (E_{ac}) transmitted to the drop.

$$E_{ac} \sim \frac{1}{2}\rho^{*}V^{*}(\omega A)^{2} \quad (3.15)$$

where the vibration frequency, volume, and amplitude are denoted by ω, V^{*}, and A, respectively. The droplet moves toward the Wenzel wetting regime due to the inertial force of the liquid that is propelled by vibration into the nanogrooves of the surface. This movement is only observable when the acoustic energy input exceeds a specified threshold, which is determined by the energy barrier (E_b), as shown in Eq. (3.16):

$$E_b \sim \frac{r_f}{x}\pi R_c^2(\gamma_{SL} - \gamma_{SV}) \quad (3.16)$$

where γ_{SL} and γ_{SV} denote the interfacial tensions between the solid and liquid–air wetting regimes, respectively, and 'x,' R_c^2 , and 'r_f' are the diameter of the particle, drop contact line radius, and average surface roughness, respectively. The study revealed that the transition in the Cassie–Baxter and Wenzel wetting equation occurs at E_{ac}~E_b, and since the droplet reaches a minimal energy state under the Wenzel condition, the shift is permanent, resulting in the droplet remaining in the Wenzel wetting regime even after the acoustic vibration has ceased.

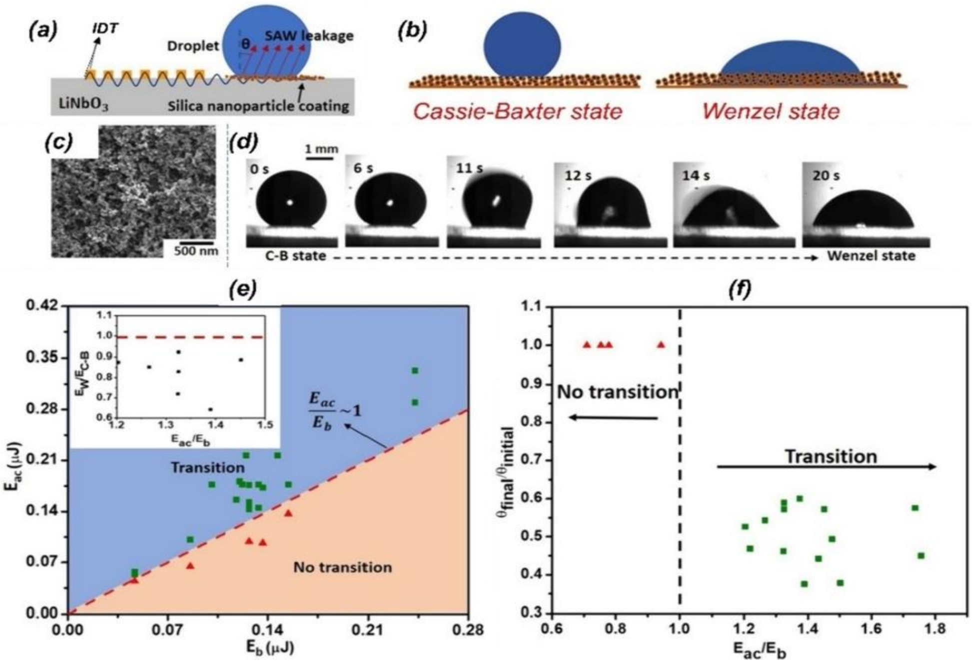

Fig. 3.7 (a) Pictorial illustration of the experimental setup; (b) picture of a droplet in the Cassie–Baxter state without application of acoustic wave and the Wenzel state with the application of acoustic wave; (c) SEM image of $LiNbO_3$ substrate with nanoparticle coating; (d) images showing the wetting transitional regime from Cassie–Baxter to Wenzel state; (e) wetting transitions from Cassie–Baxter to Wenzel state with the application of acoustic waves at various input powers and frequencies; and (f) WCA under different experimental circumstances where the applied frequency, drop volume, and input power are changed (reprinted with permission from Applied Physics Letters, Copyright © 2020, AIP Publishing [155]).

Marmur et al. [156] provided the methodological considerations for designing the superhydrophobic surface, which included the creation of two models based on different geometries. The flat model represented the two-dimensional roughness geometry using rectangular pillars with flat tops, while the second model system had semi-circular tops for the pillars. Figure 3.8a illustrates the variation in contact angles between the front and back of a droplet on an inclined plane. Meanwhile, Fig. 3.8b provides a visual comparison between the sliding (on the right side) and rolling of a droplet on the same inclined plane. In Fig. 3.8c, the illustration refers to the rolling condition with respect to the force of gravity, and Fig. 3.8d offers a simplified representation for small inclination angles. This model, known as the 'semi-circular' model, is depicted in Fig. 3.8e. In the Cassie–Baxter wetting regime, the liquid only touches the upper pillar corners and does not pass through the rough grooves. As a result, Eq. (3.17) connects the geometric radius contact angle, θ_g , to the drop base radius, 'q.'

$$q^{*^2} = S^* \frac{2sin^2_{\theta g}}{2\theta_g - sin2\theta_g} \tag{3.17}$$

where S and S^* are *2D* volume and dimensionless *2D* volume of the droplet. When the drop reached the most extreme equilibrium state, the rolling of the drop began. The mini mum Gibbs energy is related to an equilibrium state, whether stable or metastable, and is given by Eq. (3.18):

$$G = A^1{}_l\sigma_l + A^1{}_{sl}\sigma_{sl} + A^1{}_s\sigma_s \tag{3.18}$$

where σ denotes the interfacial tension, A^1 represents the *2D* interfacial area, and the subscripts 'sl,' 'l,' and 's' denote solid–liquid, liquid–air, and solid–air interfaces, respectively. Equation (3.19) represents the Gibbs energy (*G*) for a cylindrical (*2D*) drop in a dimensionless form.

$$G'' \equiv \frac{G}{p\sigma_l} = A^{1^*}_{sl} - A^{1^*}_{sl}cos\theta_Y + constant \tag{3.19}$$

where p denotes the distance between two pillars, and the interfacial areas for the Cassie–Baxter wetting regime are given by Eq. (3.20):

$$A1_{l}^{*} = 2R^{*}\theta_{g} + 2\alpha^{1}R^{*}sin\theta_{g}\ and\ A1_{sl}^{*} = 1(1-\alpha)R^{*}sin\theta_{g} \tag{3.20}$$

The percentage of the projected area composed of the inter facial liquid–air space in the grooves is indicated by α^{1}. As α^{1} increases, the liquid is exposed to air, and eventually, the solid surface disappears resulting in the absence of CAH. The dimensionless radius of the cylindrical drop is $R*$. Figure 3.8f shows the droplets in the most stable state and the magnitude of the barriers. The wetted area's influence on the metastable states of water droplets has been demonstrated. Future research should consider geometric shapes that are affected by multiple factors, including gravity and surface roughness.

In summary:

1. Implementation of new numerical techniques is required to simulate dropwise condensation for better wetting properties.

2. There is still much to learn about changes in dynamic behavior and droplet wetting states.

3. To maintain effective dropwise condensation for an extended period at a higher sub-cooling temperature, the surface wettability and micro-/nanostructure must be combined.

4. To estimate the heat transfer under various operating conditions, a unique wetting model should be developed.

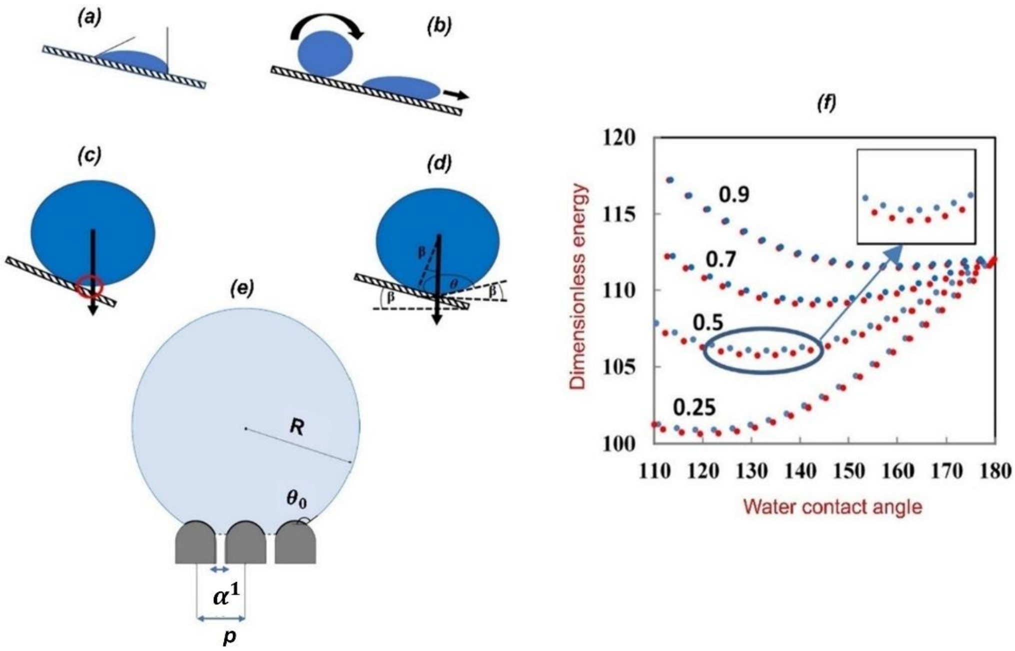

Fig. 3.8 (a) Picture of water contact angle on both the back and front sides of the inclined plane; (b) schematic picture of rolling and sliding droplet; (c) rolling conditions for water droplet gravity factor; (d) small inclination angles; (e) drawing of the semi-circular pillared structure; and (f) Gibbs energy and water contact angle for points of local maxima (blue) and minima (red) (reprinted with permission from the Journal of Colloid and Interface Science, Copyright © 2020, Elsevier [156]).

3.3. Discrepancies in transitional wetting regimes

It has been found that the wetting regime of a surface with grooves affects the flow of water drops across it [157]. When the height of the groove is less than 1.4 nm, the water drops flow into the diverging end of the groove. When the height of the groove is greater than the critical height, the wetting state of the initial drops determines its direction of migration. The Cassie–Baxter initial drops move in the direction of the converging side, while the Wenzel initial drops tend to move in the opposite direction. The opposing functions of the grooved surface and upper layers cause the drops to move in different directions.

It is believed that grooves with greater heights provide better hydrophobic conditions.

3.3.1. Kinetic energy and velocity

Cassie–Baxter and Wenzel wetting regimes are initiated due to high kinetic energy and impact velocity of water drops [158–160]. Due to the wetting transition, the liquid is prevented from flowing out of the roughness of surface and instead enters the space between the pillars, where it undergoes deposition, which is the process of droplets adhering to the solid surface. Hao et al. [141] developed two mathematical models to measure the flow of water droplets under various wetting states. These models were found to be in good agreement with the results of dynamic molecular simulation. Under the Cassie–Baxter state, a liquid droplet remains on the surface due to its low velocity, and the thermodynamic stability of the Wenzel state makes it difficult for the droplet to de-wet the Cassie–Baxter state once it is formed. As the droplet moves, its surface energy decreases more rapidly in higher grooves, indicating a greater force acting on the droplet. This is consistent with the fact that the velocity of the droplet increases as the groove height increases. Vrancken et al. [129] found discrepancies between the wetting transitions of silicon nanostructures and the true aspect ratio predicted by the classical model. When the surface tension of the liquid decreased below a certain value, the spontaneous wetting of the nanostructures began.

3.3.2. Size of water droplet and surface roughness

There are two metastable states for water droplets on sur faces with superhydrophobic properties. These states are the Wenzel state and the Cassie–Baxter state. In the Cassie–Baxter state, the droplet is suspended on the surface but does not wet the surface. In the Wenzel state, the droplet collapses into the micro-/nanostructures of the surface and wets the surface [161-162]. The property of a surface that is characterized by its irregularities is referred to as roughness, and it can be described in terms of convexity and a specific ratio of roughness, which is the ratio of the true surface area of a projection to the overall surface area [163]. If these requirements are not met, the liquid will fill the entire rough ness, preventing the air film from separating the liquid from the solid, resulting in a transition from the Cassie–Baxter to the Wenzel wetting regime. One of the most significant factors that causes the transition of the wetting regime from the Cassie–Baxter state to the Wenzel state is surface rough ness. As the surface roughness decreases, the static water droplet changes its wetting regime, which further affects the surface tension and interaction energy. However, a coating with a higher surface roughness is more prone to abrasive wear [164]. As the coating thickness increases, the width of the contact between the coated material and another surface decreases. This decrease in contact width can result in a reduction in surface roughness [165]. Thicker coatings can f ill in surface imperfections, making the surface smoother. In comparison with smooth surfaces, textured surfaces increase the rolling speed by 27% and lower the barrier to rolling viscous drops. Additionally, in the case of hard coatings, pretreatment such as grinding can improve scuffing resistance. This is due to the increased surface roughness, which improves non-wettability. Further research is required on the surface structural variations that can dramatically alter how droplets bounce to accomplish distinct roles. Therefore, it is essential to maintain an optimal surface roughness for the specific application and nature of the coating to enhance its performance.

3.3.3 Dynamics of droplet bouncing

Surface wettability is an important factor that influences droplet bounce behavior [166]. Numerous fields, including molecular dynamics, thermodynamics, heat transfer, and fluid dynamics, are involved in droplet bouncing dynamics. In the natural world, water droplets do not easily adhere to unique surfaces such as the epidermis of sharks or lotus leaves. Therefore, superhydrophobic coatings are now widely used in industry to shorten contact times. Numerous industries, including surface self-cleaning, fuel injection, micro-electromechanical systems (MEMS), and low-temperature refrigeration systems, use droplet bouncing dynamics. A pictorial representation of the droplet bouncing dynamics phenomena, and their applications is shown in Fig. 3.9. The bouncing behavior of a water droplet on a superhydrophobic surface depends on the droplet characteristics, air film, surface wettability, surface shape, etc. The financial losses resulting from icing issues on air-craft wing surfaces and wind turbine blades can be reduced by shortening the duration of water droplet contact with the surface. Droplet bouncing dynamics has also been employed in heat treatment and spray cooling and is useful in several fields. When a droplet collides with a surface, it can result in droplet bouncing, creating a water-repellent surface. The transition from a wetting to a non-wetting regime can occur through the bouncing dynamics of the impinging droplet and is facilitated by the large size of the water droplet. If a large droplet falls on smaller micro/nanofeatures, it can collapse into these structures due to the wetting transition. In the case of the non-bouncing and bouncing effects of the water droplet on the superhydrophobic surface, the total energy of the droplet exceeded the maximal gravitational potential energy, causing the droplet to bounce off the surface. When a droplet is not bouncing, the kinetic and surface energies compete for control of the free surface, leading to oscillations [168]. To meet the requirements of industrial applications, superwetting surfaces must have persistent wettability, but typical super wettability lacks durability, and a brief retention time is still an issue.

In summary:

(a) To meet the demands of numerous applications, the dynamic and wetting theory for nanodroplets must be improved.

(b) Basic wetting models can be used to accurately estimate the contact angle of any surface. However, it is unclear which hypothesis should be adopted and when.

(c) With the recent rapid advancements in micro-/nanomachining and nanotechnology, it is necessary to develop precise micro-/nanostructures.

(d) A comprehensive study that focuses on switching from the Cassie–Baxter wetting regime to the Wenzel wet ting regime associated with a solid–liquid or liquid–air interface is required.

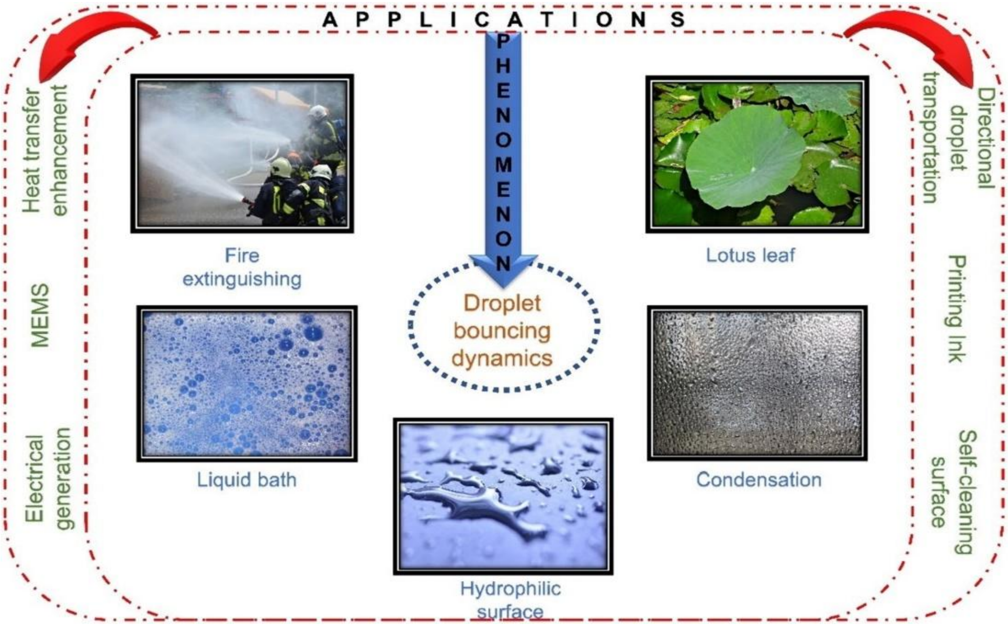

Fig. 3.9 Pictorial representation of droplet bouncing dynamics phenomena and applications (reproduced with permission from, Physics of fluids, Copyright © 2023, AIP Publishing).

3.4. Summary

This article explored the correlation between surface rough ness, the size of water droplets, and the two metastable states of water droplets on superhydrophobic surfaces. Additionally, the review article explored advanced functional mechanisms governing the dynamic behavior of droplets on superhydrophobic surfaces and examined the comparisons between theoretical and experimental findings across various transitional wetting regimes. Furthermore, the article highlighted how the high kinetic energy and impact velocity of the droplets trigger the Cassie–Baxter and Wenzel wetting regimes. Future research should focus on developing cost-effective methods to develop superhydrophobic surfaces for their widespread use. Furthermore, the research should also consider the significant environmental variables and the current challenges in implementing superhydrophobic surface in real-life applications.

CHAPTER 4. EXPERIMENTAL

4.1. RESEARCH METHODOLOGY

4.1.1. SINGLE POINT DIAMOND TURNING MACHNING (SPDT)

Single-point diamond turning (a multi-axis Precitech 700G ultra-precision machine tool) is a highly precise machining technique that is used to fabricate top-quality optical and mechanical components with sub-micrometre accuracy. Its ability to produce intricate shapes and good surface finishes makes it an essential tool in industries such as optics, aerospace, defence, and microelectronics. SPDT utilizes a diamond cutting tool to precisely remove material from the workpiece in a controlled manner. Unlike conventional machining methods that utilize multiple cutting edges, SPDT involves a single point of contact between the workpiece surface and the diamond tool, allowing for precise and fine machining. In SPDT, the workpiece is mounted on a spindle and rotated at high speeds as depicted in fig.4.1. A diamond cutting tool, often in the form of a single crystal diamond or a diamond-tipped tool, is brought into contact with the rotating workpiece. As the tool cuts into the material, it creates the desired shape or surface profile through a combination of cutting and abrasion. SPDT is commonly used in the fabrication of optical components such as lenses, mirrors, prisms, and diffractive optical elements (DOEs). It is also employed in the manufacture of precision mechanical parts, microfluidic devices, and semiconductor components. The technique is particularly valuable for components requiring high surface quality, tight tolerances, and complex geometries. SPDT offers several advantages over traditional machining methods including high precision, superior surface finish, and the capability to machine a wide variety of materials including metals, plastics, ceramics, and optical glasses. It can produce complex shapes with sub-micrometre accuracy, making it ideal for manufacturing components for advanced optical and mechanical systems. Despite its advantages, SPDT has limitations, including limited material removal rates compared to traditional machining methods. Additionally, the process requires careful control of cutting parameters, tool wear management, and surface quality monitoring to achieve desired results consistently. The SPDT instrument is depicted in fig. 4.1.

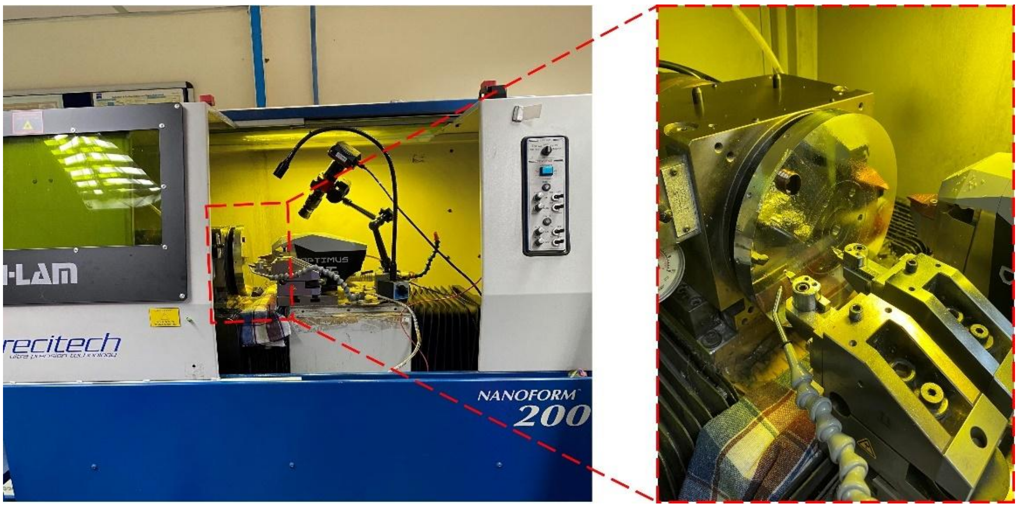

Fig. 4.1. The SPDT (a multi-axis Precitech 700G ultra-precision machine tool) instrument setup [Ref @ Integrated Manufacturing, Mechanical Design and Fab Facility (MDF)].

4.2. MATERIALS

The following materials were used for the fabrication of microstructures.

- Aluminium alloy disc (diameter ~ 15 mm and thickness ~ 3 mm)
- Ethylene tetrafluoroethylene (ETFE, diameter ~ 5 mm) from Daikin Chemicals, UK.

4.3. CHARACTERIZATIONS

4.3.1. FIELD EMISSION SCANNING ELECTRON MICROSCOPY (FESEM)

Field Emission Scanning Electron Microscopy (FESEM) (Carl Zeiss, Germany Model- Zeiss Gemini 300) is a highly advanced imaging technique that allows for detailed examination of materials' surface morphology and structure at high resolution. In FESEM, a focused electron beam scans the specimen surface, producing various signals, including backscattered electrons, secondary electrons, and X-rays. These signals are detected and processed to generate high-precision images. The resolution offered by FESEM is exceptionally high, typically reaching the nanometre scale, allowing researchers to analyse fine surface features, topography, and even chemical composition. FESEM has broad applications across numerous fields, including materials science, nanotechnology, biology, and semiconductor research, providing critical insights into the microstructure and properties of a wide range of materials. FESEM's underlying principle revolves around the interaction between a highly focused electron beam and the sample surface. This technique employs a field emission electron gun as its electron source, which produces a narrow, high-current-density beam. The emitted electrons are then accelerated by a series of electrostatic and magnetic lenses, which further refine and direct the beam toward the sample surface. When the electron beam interacts with the sample, it generates various signals, including secondary electrons, backscattered electrons, and X-rays. Secondary electrons offer insights into the sample's topography, whereas backscattered electrons, which are sensitive to variations in atomic number and density, provide compositional contrast. X-rays, on the other hand, are emitted when inner-shell electrons are dislodged from atoms in the sample, providing information about the sample's elemental composition. Detectors within the FESEM system capture these signals, which are then processed to generate high-resolution images of the sample surface. These images reveal the sample's topography, morphology, and composition at the nanoscale. The FESEM instrument is depicted in the fig. 4.2.

Fig. 4.2. The FESEM (Carl Zeiss, Germany Model- Zeiss Gemini 300) instrument setup [Ref. @ Institute Instrumentation Centre, IIT Roorkee].

4.3.2. DROP SHAPE ANALYZER (DSA)

The Drop Shape Analyzer (DSA25, Kruss) is an instrument designed for laboratory use that can analyse the shape and surface tension of liquid drops on solid surfaces. It works by capturing images of liquid droplets that have been deposited on a substrate and then utilizing advanced image processing algorithms to determine various parameters such as the contact angle, drop volume, and surface tension. The DSA has a wide range of applications in both research and industry, including the optimization of surface coatings and the study of wetting behavior on biomaterials. Its ability to make precise measurements and its versatile capabilities make it an invaluable tool for understanding interfacial phenomena and designing advanced materials with tailored surface properties. To measure the contact angle, a small volume of liquid is deposited onto the surface using a syringe or another dispensing apparatus. The liquid droplet then either spreads or contracts on the surface, influenced by the surface energy and the interactions between the liquid and the solid. High-resolution imaging equipment captures the droplet on the solid surface, revealing its contour and any relevant reference points. The contact angle is determined as the angle between the tangent to the droplet's surface and the solid surface at the contact point. This measurement is crucial for assessing the wetting behavior of the liquid on the solid surface: a contact angle close to 0° indicates complete wetting (high surface energy), while an angle near 180° signifies non-wetting or partial wetting (low surface energy). Additionally, DSA systems may provide further capabilities, such as drop volume measurement and dynamic contact angle analysis, including advancing and receding angles. These features render DSA a versatile and precise method for characterizing wetting properties and understanding liquid-solid interactions across various fields, including materials science, surface coatings, and biotechnology. The DSA instrument is depicted in the fig. 4.3.

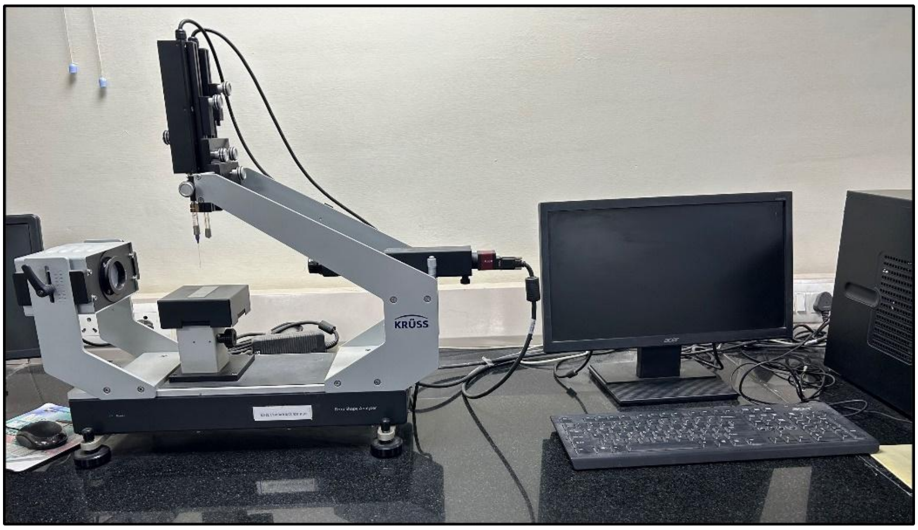

Fig. 4.3. The (DSA 25, Kruss) instrument setup [Ref. Central Instrumentation Center @ UPES].

4.3.3. COHERENCE CORRELATIONAL INTERFEROMETER (CCI)

Coherence correlational interferometers (CCI-6000, Taylor Hobson) are sophisticated optical instruments that are utilized in the fields of metrology and interferometry. These instruments are designed to measure the surface characteristics of optical components with an extremely high level of precision. The operation of these instruments is based on the principle of interference patterns. This is achieved by splitting a coherent light beam into two separate paths, which are then recombined after interacting with the surface under investigation. By analysing the interference patterns, the instrument can determine parameters such as surface roughness, flatness, and the thickness of transparent materials. The light source in the interferometer is typically a laser that emits a coherent light beam, which means that the light waves have a consistent phase relationship with each other over time. This coherence allows the interference patterns to be formed when the light waves interact with each other. One beam is directed towards the reference mirror, while the other is directed towards the surface under examination. The measurement beam reflects off the surface of the optical component and undergoes changes in phase and amplitude due to surface characteristics such as roughness or thickness. The two beams recombine using another beam splitter, resulting in an interference pattern characterized by alternating bright and dark fringes. A detector, such as a CCD camera, captures the interference pattern, and by analysing the pattern of interference fringes, the instrument can extract precise information about the surface characteristics of the optical component. The coherence length of the light source dictates the maximum optical path length difference over which interference can be effectively observed. This parameter significantly affects the instrument's capacity to resolve surface features with high precision. The CCI instrument is depicted in the fig. 4.4.

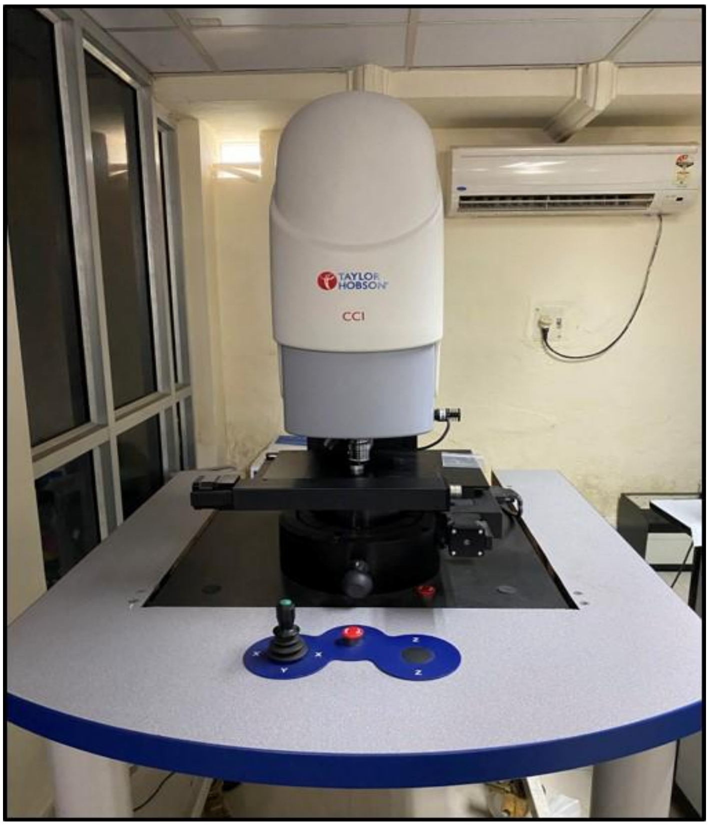

Fig. 4.4. The (CCI-6000, Taylor Hobson) instrument setup [Ref @ Integrated Manufacturing, Mechanical Design and Fab Facility (MDF)].

4.3.4. FOURIER TRANSFORM INFRARED SPECTROSCOPY (FTIR)

Fourier Transform Infrared Spectroscopy (Frontier FT-IR/FIR, Perkin Elmer) is a sophisticated characterization tool employed to identify and analyse the chemical composition of materials based on their interaction with infrared light. This technique operates on the principle that molecules absorb infrared radiation at specific frequencies corresponding to the vibrational modes of their chemical bonds. By measuring the absorption of infrared light across a spectrum of frequencies, FTIR provides a distinct chemical fingerprint of the sample. The infrared light is directed through the sample, and the transmitted or reflected light is collected by the FTIR spectrometer. A beam splitter divides the light into two paths: one path interacts with the sample, while the other is directed to a reference mirror. The beams are subsequently recombined, and their interference pattern is detected by a sensor. A Fourier transform algorithm is then applied to the detected signal, converting it into a spectrum that represents the sample's absorption as a function of frequency. FTIR is employed across various disciplines, including chemistry, pharmaceuticals, materials science, forensics, environmental science, and biochemistry. It is applicable to the analysis of solids, liquids, and gases, providing crucial information about molecular structure, functional groups, impurities, and chemical reactions. FTIR is noted for its advantages, such as rapid analysis, high sensitivity, and the capability to analyse samples in diverse physical states without extensive sample preparation. Additionally, it supports both qualitative and quantitative analysis, rendering it a versatile tool in both research and industry. Interpretation of FTIR spectra involves comparing observed absorption bands with reference spectra or databases to identify the functional groups and chemical compounds present in the sample. The FTIR instrument is depicted in the fig. 4.5.

Fig. 4.5. The (Frontier FT-IR/FIR, Perkin Elmer) instrument setup [Ref. Central Instrumentation Center @ UPES].

CHAPTER 5. ADVANCEMENT OF ANALYTICAL MODEL FOR HYDROPHOBIC RECTANGULAR PILLARED ARRAY ON AL-SURFACE AND ITS EXPERIMENTAL VALIDATION

5.1. ABSTRACT

Over the past few decades, self-cleaning surfaces have been significantly investigated due to their commercial applications in various fields. However, the researchers are still lagging in developing better mathematical models and fabricating hydrophobic surfaces for direct espousal in industry. In this study, a force-balanced system-based mathematical model is modified for a rectangular pillared array-based micro-structure and MATLAB simulations were used to validate it theoretically. The same pattern was developed on Al-surface using a single-point diamond turning (SPDT) machine experimentally. The experimental results were validated using coherence correlation interferometry (CCI), optical microscopy, drop shape analyser (DSA), and field emission scanning electron microscopy (FESEM). The experimentally estimated and theoretically predicted contact angles of the rectangular pillared array are found in close agreement. Further, the advancement in mathematical models and models-based surface manufacturing strategies can boost the research in this domain to develop robust self-cleaning hydrophobic surfaces.

5.2. HIGHLIGHTS

- A force-balance mathematical model is reformed for a rectangular pillared array structure.
- MATLAB simulations are used to validate it theoretically.
- Rectangular pillared array structure was developed on Al-surface using SPDT.
- The experimental results are validated using CCI, DSA and FESEM.

5.3. INTRODUCTION

The fundamental mechanism of hydrophobic or superhydrophobic surfaces has been the subject of numerous theoretical models in recent years, but it has been difficult to employ any of these models to support an experimental observation for real-world application. As a result of their ability to partially clean themselves, these surfaces have numerous uses in various domains such as anti-fogging [168], anti-corrosion [169-174], anti-icing [175], drag reduction, self-cleaning surfaces [176-178], etc. Numerous methods for preparing hydrophobic surfaces have been proposed till now. Bottom-up and top-down techniques are frequently used to create micro/nano textured surfaces including laser etching, lithography, electrochemical methods, and so on [179-182]. The need of generating nanoscale features on metallic or non-metallic surfaces forced the researchers to use highly precise techniques like single-point diamond turning (SPDT). The SPDT machining is the most efficient method for manufacturing technology patterned sur faces with high precision and accuracy. This technique can produce a smooth textured surface with controlled roughness of 2–10 nm. The SPDT can be used for metallic, non-metallic and polymers to design the desired patterns. Aluminium has been selected as the substrate material in the current study due to its low cost, lightweight, high thermal conductivity, and ease of availability. Aluminium is a hydrophilic material, and it has a water contact angle of 85.6°. Aluminium has a wide range of uses, particularly in the biomedical, modern engineering, civilian industries, automobile, aircraft, and transportation. However, in extreme environments, the use of aluminium is constrained by its vulnerability to corrosion and surface contaminations. It is preferable to improve aluminium surface qualities through surface modifications in order to avoid such issues. Creation of a hydrophobic surface on Al is a good alternative to avoid the corrosion of Al. Hydrophobic surfaces are a combination of micro/nano texturing features that support the formation of air pockets between the solid liquid interface and the water droplet. One of the key elements directly influencing a water droplet's wetting behaviour on a rough surface is surface geometry. The wetting properties are largely caused by two primary factors: the material's low surface energy and surface roughness. As a result, surface characteristics are attributed to a material's intrinsic properties, providing a more accurate interpretation of the structures. This concept is directly related to the wetting theories of the surfaces. Young's equation, which was appropriate for smooth and homogeneous surfaces, first provides the wetting theory. Then, Wenzel’s theory came into the picture. It was also effective for homogeneous surfaces but had some roughness components which had certain limitations. Ideally, it is almost impossible to manufacture a single surface that is entirely homogeneous and flawlessly smooth. Hence, there is always some degree of surface roughness exists. To disprove Wenzel's idea, the Cassie-Baxter equation which is only applicable to heterogeneous surfaces with surface roughness factor was introduced. Air pockets may cause the surface to become extremely hydrophobic. Water droplet forms a spherical shape and roll off the surface as a result of the droplet of liquid being unable to pass through the roughness between the cavities. Although it is simple to characterise the states of the classical Cassie-Baxter and Wenzel models for surfaces having ordered roughness, it is frequently challenging to determine the roughness and fractional surface values on such textured surfaces. The fundamental mechanism of these surfaces has been the subject of numerous theoretical models in recent years, but it has been difficult to employ any of these models to support an experimental observation for real-world application [170]. The various geometrical characteristics that can aid in understanding the fundamental ideas behind these surfaces are now being discovered by researchers. The reduction of drag on micro/nano structured surfaces, slip length on hydrophobic surfaces, liquid flow through microchannels, and force balance system on water droplets sitting on the micro/nano structures, and viscosity factors for various liquid flows are all being demonstrated by researchers. Sudeepthi et al. [155] developed a mathematical model to find the irreversible wet ting transitions between the Wenzel and Cassie-Baxter state on a nano structured surface. In the Cassie-Baxter state, the liquid sits on top micrometre scale protrusions that originate from the clustering of the nanoparticles. In contrast, the solid portion of the coating is completely covered by the liquid in the Wenzel state, increasing the area fraction. But, till date, the development of hydrophobic surfaces that can last up to a few years is still not achieved due to the lack of understanding of hydrophobic surfaces. Hence, every single parameter is equally important in contributing to the best wetting regime. Although there are several experimental investigations on water-repellent surfaces and similarly many theoretical models available for hydrophobic surfaces. However, very limited studies are available on developing a mathematical model for a hydrophobic surface and replicating that specific surface on a substrate practically. The modification of surface wettability on Al substrates offers significant potential for revolutionizing various industries, including electronics, aerospace, biomedical, and energy sectors. With the increasing demand for advanced materials with modified surface properties, it is crucial to understand and optimize hydrophobic patterns on Al sur faces to enhance performance and functionality. Achieving hydrophobicity on Al substrates can address challenges related to corrosion resistance, water repellence, and adhesion in diverse applications. The ability to modify sur face properties through theoretical wetting models allows for the design of materials with improved durability, reduced maintenance costs, and enhanced performance in harsh environments. For real life applications of hydrophobic sur faces, such types of research are imperative. Therefore, a force balanced system based mathematical model is modified for a rectangular pillared array structure and SPDT machining is used to manufacture the same structure on Al to vali date the theoretical results. This theoretical model not only enables a systematic understanding of the mechanisms that govern wetting behavior, but also functions as a predictive tool for designing surfaces with desired hydrophobic properties. This theoretical model plays a crucial role in guiding experimental research, providing insights into the complex relationship between surface morphology, chemistry, and environmental factors that influence wetting phenomena.

5.4. DEVELOPMENT OF A MATHEMATICAL MODEL

Force balance mathematical model [22] is modified to investigate the hydrophobic character of rectangular pillared array structure. The shape of a water droplet on a surface is influenced by several factors, such as water's surface tension, the material's surface energy, and the interaction between the water and the surface. Textured surfaces, depending on their dimensions and spacing, can affect how a droplet spreads or contracts. The ability of a water droplet to assume a spherical shape on a textured surface depends on the specific properties of the surface texture. If the texture encourages anisotropic wetting and the energy barrier for the droplet to spread along one axis is lower than in other directions, the droplet may take on a more elongated or flattened shape along that axis. Conversely, if the texture is fine and doesn't significantly disrupt the cohesive forces of the water, the droplet may still tend to be roughly spherical, but with modifications due to the texture. The contact angle is typically measured from the solid surface in the direction of the liquid phase. It is the angle between the solid surface and the tangent line to the liquid droplet or meniscus at the three-phase contact point (solid–liquid–air). Pillared textures can influence contact angle and droplet behavior by providing additional surface area and trapping air pockets. Theoretical models often consider the balance of interfacial energies, including the surface energy of the solid and liquid phases. Fig. 5.1 depicts several forces operating on a water droplet under equilibrium conditions to balance water weight. The three reaction forces, which are characterized as reaction force by the textured surface, surface tension caused by the drop, and the peripheral surface tension, balance the weight of the water droplet.

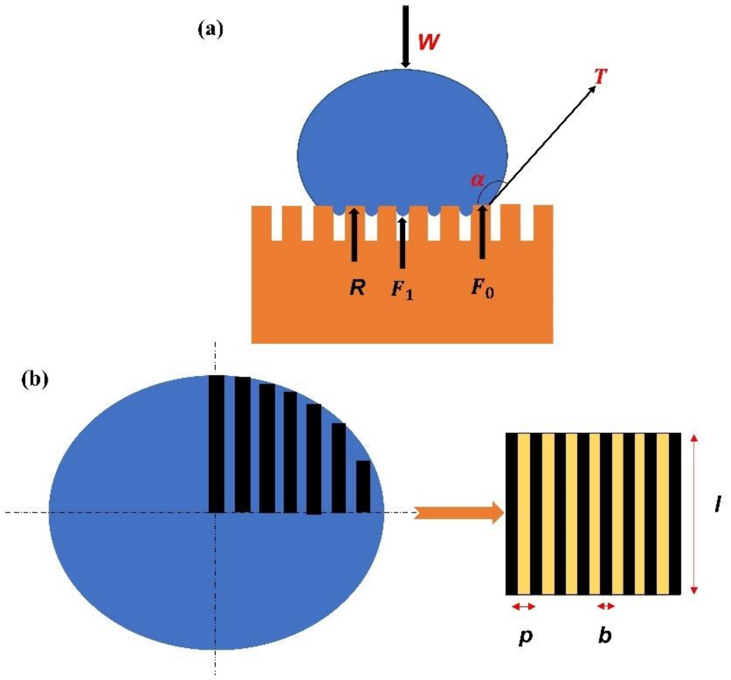

Fig. 5.1. (a) Schematics of different forces influencing a water droplet at equilibrium conditions to balance water weight determined by the force balance system; (b) representation of an array of structures with rectangular pillars.

The relation between the geometrical parameters and water contact angle were determined by evaluating these equations. Assume that water droplets adhere to the surface. The contact angle is influenced by surface tension and geometrical parameters. Let (l) be the length of the pillar and (b) be the width of the geometrical shape pillars. The pillars are assumed to be evenly distributed on the surface. Gravity's influence is ignored along the radial direction. The droplet's radius does not change before or after it lands on the surface. The following force-balance equation can be used to calculate the water droplet's weight:

$$W = R + F_0 + F_1 \tag{5.1}$$

where, W denotes the weight of water drop, R denotes the reaction force by the rectangular pillars, F_0 denotes the surface tension at the periphery and F_1 denotes the surface tension due to water drop.

The following equation is used to determine weight of water droplet:

$$W = \frac{4}{3}\pi R_0^3 \rho g \tag{5.2}$$

Where ρ denotes the density and g denotes the acceleration due gravity.

Reaction forces due to rectangular pillars can be calculated as:

$$R = (h + y)(l.b)\frac{\pi R_1^2 \rho g}{\left(\sqrt{l.b}+p\right)^2} \tag{5.3}$$

The water droplet's periphery's surface tension for rectangular pillars is given by:

$$F_0 = 2\pi R_0 cos^2\theta \tag{5.4}$$

The line of contact between the water droplet and the pillars tops generates a force called surface tension for rectangular pillars that can be calculated as:

$$F_1 = \frac{4aT\pi R_1^2}{\left(\sqrt{l.b}+p\right)^2} \sin\varphi \tag{5.5}$$

Using equations (5.2), (5.3), (5.4), and (5.5)**,** we can reduce the force balance model for the rectangular pillars as:

$$\left(\frac{4}{3}\pi R_0^3\right)\rho g = \left[R_0 \sin\theta + R_0 - \frac{1}{12}\left(R_0 \cos\theta + \sqrt{l.b} + p\right)\left(R_0 \cos\theta + 2\sqrt{l.b} + 2p\right)\right]\frac{l.b.\pi R_0^2 cos^2\theta.\rho.g}{\left(\sqrt{l.b}+p\right)^2} + \frac{\pi R_0^2 cos^2\theta}{\left(\sqrt{l.b}+p\right)^2} \times 4\sqrt{l.b}.T \sin\left[\cos^{-1}\frac{p}{\left[\left(\frac{p}{2}\right)^2+\left\{\frac{1}{2V}\left[\left(\frac{p}{2}\right)^2-V^2\right]^2\right\}^{\frac{1}{2}}\right]}\right] + 2\pi R_0 T cos^2\theta \tag{5.6}$$

In equation (5.6), θ denote the contact angle, p denote the gap between two rectangular pillars, T denote the surface tension.

Taking the parameter p common from the right side of the above equation, the following expression can be obtained:

$$\left(\frac{4}{3}\pi R_0^3\right)\rho g = \left[R_0 sin\theta + R_0 - \frac{p^2}{12}\left(\frac{R_0 cos\theta}{p} + \frac{\sqrt{l.b}}{p} + 1\right)\left(\frac{R_0 cos\theta}{p} + \frac{2\sqrt{l.b}}{p} + 2\right)\right]\frac{l.b.\pi}{p^2}\frac{R_0^2 cos^2\theta}{\left(\frac{\sqrt{l.b}}{p}+1\right)^2}.\rho g +$$

$$\frac{\pi R_0^2 cos^2\theta}{p^2\left(\frac{\sqrt{l.b}}{p}+1\right)^2}.4\sqrt{l.b}.t.\sin\left[\cos^{-1}\left\{\frac{p}{2\left[\left(\frac{p}{2}\right)^2+\left\{\frac{1}{2V}\left[\left(\frac{p}{2}\right)^2-V^2\right]^2\right\}^{\frac{1}{2}}\right]}\right\}\right] + 2\pi R_0 T cos^2\theta$$

(5.7)

For the simplification, assume $\sin\theta = x,\ \cos\theta = \sqrt{(1-x^2)}$, $A = \frac{\sqrt{lb}}{p}$ and $B = \frac{p}{2}$ to obtain the following expression:

$$\frac{4R_0^3.\rho.g}{3} = \left[R_0 x + R_0 - \frac{p^2}{12}\left(\frac{R_0(1-x^2)}{p^2} + \frac{3(A+1)R_0\sqrt{1-x^2}}{p} + 2(A+1)^2\right)\right].\frac{A^2R_0^2(1-x^2)\rho g}{(A+1)^2} +$$

$$\frac{R_0^2(1-x^2)}{p^2(A+1)^2}.4\sqrt{l.b}.Tsin[\cos^{-1}\left\{\frac{p}{2\sqrt{(B)^2+\left[\frac{1}{2V}\{(B)^2-V^2\}^2\right]}}\right\} + 2R_0T(1-x^2)$$

(5.8)

Now, we can find x from the following expression:

$$x = \left[\frac{4}{3}\frac{(A+1)^2}{A^2(1-x^2)} - 1 + \frac{B^2}{3R_0}\left(\frac{R_0(1-x^2)}{p^2} + \frac{3(A+1)R_0\sqrt{1-x^2}}{p} + \frac{3(A+1)R_0\sqrt{1-x^2}}{p} + 2(A+1)^2\right)\right] - \frac{(A+1)^2}{A^2R_0}\frac{1}{B^2\rho g}\sqrt{l.b}.T\sin[\cos^{-1}\left\{\frac{B}{\sqrt{(B)^2+\left[\frac{1}{2V}\{(B)^2-V^2\}^2\right]}}\right\} - \frac{2T}{R_0\rho g}.\frac{(A+1)^2}{A^2} \tag{5.9}$$

Finally, we can calculate the contact angle θ as:

$$\theta = \ sin^{-1}\left[\frac{4}{3}\frac{(A+1)^2}{A^2(1-x^2)} - 1 + \frac{B^2}{3R_0}\left(\frac{R_0(1-x^2)}{p^2} + \frac{3(A+1)R_0\sqrt{1-x^2}}{p} + \frac{3(A+1)R_0\sqrt{1-x^2}}{p} + 2(A+1)^2\right)\right] - \frac{(A+1)^2}{A^2R_0}\frac{1}{B^2\rho g}\sqrt{l.b}.T\sin[\cos^{-1}\left\{\frac{B}{\sqrt{(B)^2+\left[\frac{1}{2V}\{(B)^2-V^2\}^2\right]}}\right\} - \frac{2T}{R_0\rho g}.\frac{(A+1)^2}{A^2} \tag{5.10}$$

For calculation of θ, the following values were considered:

$a = \sqrt{l.b} = 60 \times 10^{-6}$ m, $R_0 = 0.003$ m, $p = 85 \times 10^{-6}$ m, $g = 9.8$ m/s^2, $V = 0.001$ m and $\rho = 997$ kg/m^3

The graphical results for the contact angle versus parameter a/p were obtained with the help of MATLAB software.

5.5. EXPERIMENTAL

The micro-rectangular pillared array surface was created using SPDT machining, one of the well-known production methods that can create sub-micron to nano level structures with great accuracy. Fig 5.2 represents the schematic view of the fabrication of a rectangular pillared textured surface dimensional tolerances that refers to the allowable deviation from the intended dimensions or specifications of a machined component. It represents the degree of accuracy and precision that can be achieved during the diamond turning process.

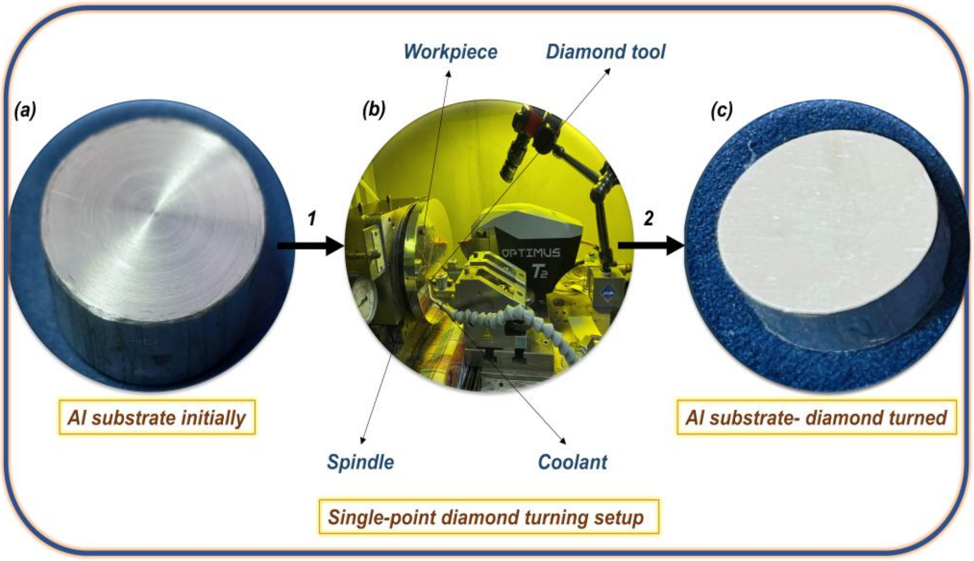

Fig. 5.2. Schematic view of the systematic fabrication of a rectangular pillared textured surface using SPDT machine.

5.5.1. MATERIALS AND SPECIFICATIONS

Aluminium (Al) was used as the work piece material in this study to produce micro textured hydrophobic surfaces. Aluminium discs with dimensions of 15 mm in diameter and 3 mm in thickness were used.

5.5.2. FABRICATION OF MICRO-RECTANGULAR PILLARED ARRAYED SURFACE ON AL

The wedge was entirely removed from the Al work piece on both sides using a diamond tool (Fig. 5.2a). The mirror finished surface was prepared for the following stage, which involves fabricating micron-sized rectangular pillared structures (Fig. 5.2c). After that, the surfaces were cleaned thoroughly in an ultrasonic bath to get rid of any leftover residue or machining chips. The work piece was held in a vacuum chuck to ensure a secure and stress-free grip as well as to stop undesired chips from adhering to the work piece. Table 5.1 displays the parameters of SPDT machining to develop the desired micro-rectangular pillared arrayed surface on Al. These variables were picked based on those that were utilised in the theoretical modelling. As shown in Fig. 5.2b, SPDT is utilised to project ordered micro features onto Al. To ensure a good surface finish during the machining process, the work piece was offset such that its face was aligned with the vertical axis. This prevented heat generated at the cutting zone from the machining process from damaging the tool and the work piece. Clairsol 330 was employed as a coolant. The test was carried out under a constant cooling environment. Under ambient conditions, pillars with a rectangular shape were created on the work piece.

Table 5.1. The parameters of SPDT machining to develop micro-rectangular pillared arrayed surface on Al.

Specifications	Machining parameters
Diamond tool	Single crystal
Nose radius	0.2 mm
Rake angle	0º
Speed of spindle	1000 rpm
Tool feed rate	1 µm/rev
Clearance angle	10º
Depth of cut	5 µm
Pitch of rectangular pillared structure	35.04 µm

Height of rectangular pillared structure	28.84 µm
Width of rectangular pillared structure	47 µm

5.5.3. CHARACTERIZATIONS

Coherence Correlation Interferometer (CCI), a white light interferometer (CCI-6000, Taylor Hobson) was used to characterize the surface topographies of the rectangular pillared structures at different magnifications. Field emission scanning electron microscopy (FESEM, Carl Zeiss Germany, model: Zeiss Gemini 300) was utilized to examine the rectangular pillared array structures fabricated on the Al surface. FESEM tests were carried out at an accelerating voltage of 10.0 kV. An optical microscope (Nikon Eclipse MA200) was used to investigate the surface topographies. A contact angle goniometer or drop shape analyser (DSA25, Kruss) was used to determine the water contact angle. The droplet volume was set at 5 µl for all water contact angle measurements and deionized water was used.

5.6. RESULTS AND DISCUSSIONS

Fig. 5.3 displays optical microscopic pictures of the single scale textured Al surface at various magnifications, including 5X, 10X, and 20X. The surface of Al seems exception ally smooth with consistent surface roughness due to the diamond turning single texturing (Fig. 5.3).

Fig 5.3. Illustrations for optical microscopy at various magnifications (a) 5X, (b) 10X, (c) 20X.

Al-sample area of approximately 8 × 8 mm was scanned using CCI. The CCI was used to extract the 2D cross sectional profile and 3D topology of the textured surface. Fig 5.4a–c illustrates the measured 3D and 2D profiles of the fabricated rectangular pillars, respectively. Figure 5.4b depicts the burr formation on rectangular pillars. A burr means rough edges or ridges on a metal. Generally, the burr formation happens during cutting operations on metals. It is common during SPDT machining of metal samples such as Al (in current study). The height (28.84 μm), width (47 μm) and inter-pillar spacing (35.04 μm) of rectangular pillars was measured using a 3D profile of the textured surface.

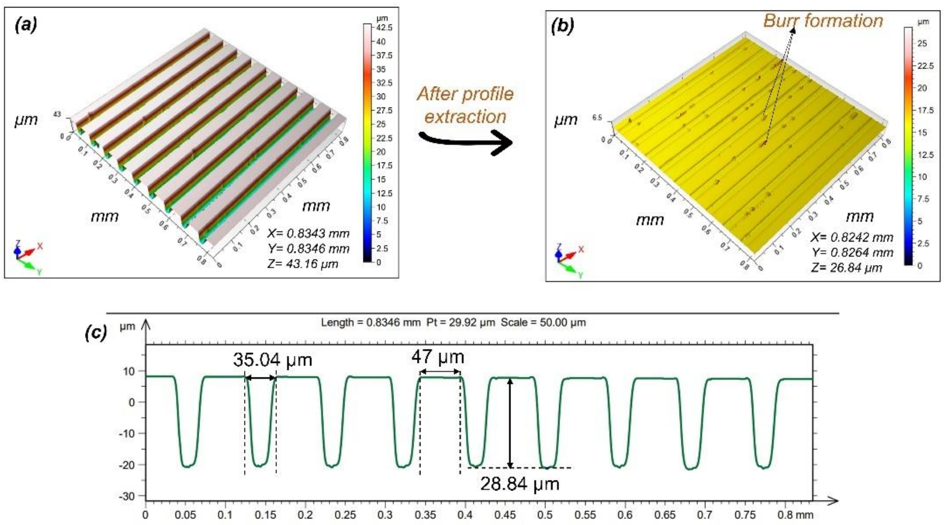

Fig. 5.4. Identification of surface topographies: (a) Magnified 3-D view of the rectangular pillars, (b) 3-D surface topology after the profile extraction and (c) Extracted 2-D profile of the rectangular pillars.

Fig 5.5 depicts the FESEM images of rectangular pillared textured surfaces at 200 X, and 1000 X. The individual micro-rectangular pillars on the Al have a slightly tapered shape, which presumably originates from the chip formation during machining. However, the micro-rectangular pillars are found quite smooth, stable, and periodically patterned, providing the first-level roughness with consider able structural uniformity (Fig. 5.5a). Even though the surface is thoroughly cleaned in an ultrasonic bath before FESEM characterization, burr formation can be seen at some sites highlighted by dotted circles (Fig. 5.5b), which may be caused by cutting action during the fabrication process. The burr formation is negligible and can be minimized further by modifying SPDT process parameters. The width (47 µm) and inter-pillar spacing (35.04 µm) of rectangular pillars was further verified using FESEM and found in disagreement with the results of CCI. Our analysis of the image using ImageJ software revealed that the width of the rectangular pillars is (16.19 µm) and the inter-pillar spacing is (14.02 µm).

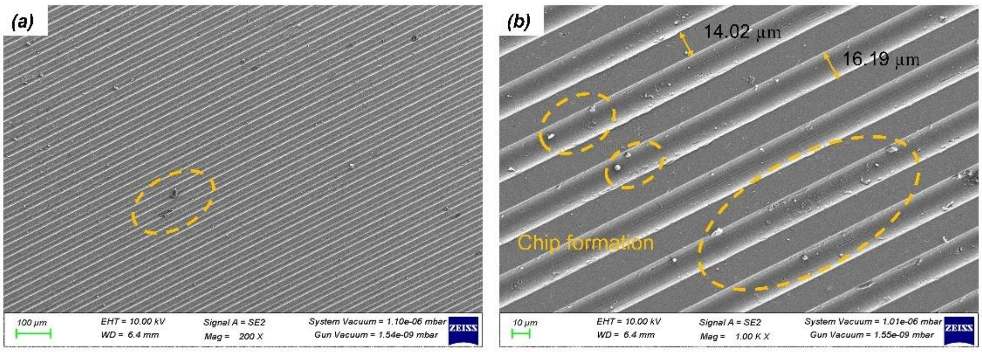

Fig 5.5. FESEM images of rectangular pillared textured surfaces at various magnifications (a) 100 µm at 200 X, (b) 10 µm at 1 KX.

Fig. 5.6a shows the water contact angle of 85.6° on the Al substrate and Fig. 5.6b shows the water contact angle of 123.7° ± 3° on the particular point of the textured surface. Moreover, Fig. 5.6c depicts the top view of a water droplet sitting on the textured Al substrate. Figure 5.6d shows the side view of the water droplet that indicates the water drop let is not immersed inside the rectangular pillars, but it is sitting on the micro protrusions of Al substrate. The low water contact angle on non-textured Al indicates its hydrophilic character; however, the higher contact angle on the textured Al reveals the hydrophobic nature of it. Thus, the wetting regime shifts from hydrophilic to hydrophobic one. The contact angle obtained in Fig. 5.6b aligns with the theoretical expectations for the Cassie-Baxter regime, which is characterized by reduced wetting. This phenomenon occurs when a liquid droplet sits on a rough or patterned surface, and instead of completely wetting the surface, it partially traps air pockets between the liquid and solid interface. The result indicates that the observed patterned surface represents areas where the Cassie-Baxter wetting state predominates, as higher contact angles are indicative of reduced wet ting. Therefore, this study supports the contact angle model that strengthens the theoretical basis for the application of hydrophobic patterns on Al substrates. As a result, the single scale texturing has produced the hydrophobic properties of the textured Al. Furthermore, adding double texturing to the substrate can improve contact angle and it can even lead to the formation of a superhydrophobic surface.

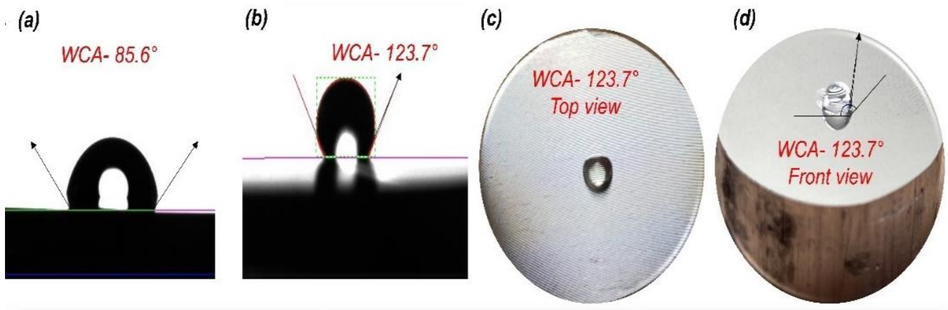

Fig. 5.6. A visual representation of the contact angle with the water: (a) water contact angle (85.6°) on bare aluminium (b) employing a drop shape analyser to determine the water contact angle (123.7°) on textured aluminium, (c) water droplet sitting on a single textured surface, (d) illustration of the water contact angle at 123.7° on a particular one point of the textured surface.

5.7. DIFFERENCE BETWEEN THEORETICAL AND EXPERIMENTAL FINDINGS

Generally, the scaling factor (a/p = 1) gives the maximum water contact angle for the desired size to spacing factor. This implies that maintaining a balanced relationship between substrate size and spacing can optimize the hydrophobic properties of the surface. In the existing work, the scaling ratio (a/p = 1) for the rectangular pillared structures is considered. The Roy et al. [183] model with a square pillared textured surface provided the initial validation of the mathematical model. An experiment using a single textured surface with single point diamond turning machining at (l = 47 µm and p = 35.04 µm) revealed an average CA of 123.7° ± 3° of the textured surfaces, somewhat near to the projected value of 136.6°. The difference between the experimental results and the value predicted by the theoretical model anticipated is -9.44%. A negative percentage error of -9.44% signifies that the experimental value is lower than the theoretical value by 9.44%. The discrepancy between the two values could stem from various factors, such as experimental errors, deficiencies in the theoretical model, or external influences that were not taken into account during the experiment. Recognizing this error allows for the assessment of the experimental procedures' reliability and the theoretical model's accuracy, leading to further refinement in both areas. Here, aspect ratio is the reason. Our aspect ratio for the experimental work was close to 1.48, and it has been demonstrated in the literature that an aspect ratio of 1.0 can result in the highest water contact angle. The single-level textured surface is another factor. Because the maximum contact angle is provided by a combination of micro and nano texturing structures. This demonstrates the differences between theoretical and experimental results. Figure 5.7a depicts a graphical representation of water contact angle and aspect ratio for different values of ‘p’ while ‘a’ is fixed. Figure 5.7b depicts a graph for different values of ‘a’ while ‘p’ is fixed. Figure 5.7c represents a graph highlighting the difference between the theoretical and experimental results. The machining parameters have a significant impact on the difference between experimental and theoretical findings. The lowering in the water contact angle is caused by the presence of burr formation in conjunction with the rectangular pillared array. In a rectangular pillared array with three dimensional high-frequency vibrating modes, the water droplet expands in the feed direction, which reduces the wettability performance of the textured surface and causes the variation. Moreover, the tool feed rate is a significant aspect, since it influences the radius of the machined groove profile, which decreases as the feed rate is increased. The rise in feed rate causes the increase in cutting force, which in turn causes a burr effect on the textured surface. An additional important factor that leads to discrepancies is precipitates. If the stress value does not exceed the stress limit, the precipitates may be pushed by the diamond tool and move in the direction of the cutting. In this situation, the machined surface develops deeper pits and scratch marks. The surface of the precipitate becomes cracked and uneven when it is manipulated with a diamond tool, which further reduces the water contact angle. A thorough analysis that focuses on fabricating complex structures using SPDT machining is required. Directly creating nanostructures on the substrate's surface via SPDT machining is difficult. To fulfil the wetting regime, tool optimisation is required since depth of cut, and tool feed rate are crucial factors. Geometrical characteristics, such as the width, pitch, and height of the structures, are crucial in self-cleaning applications since they are related to the water contact angle.

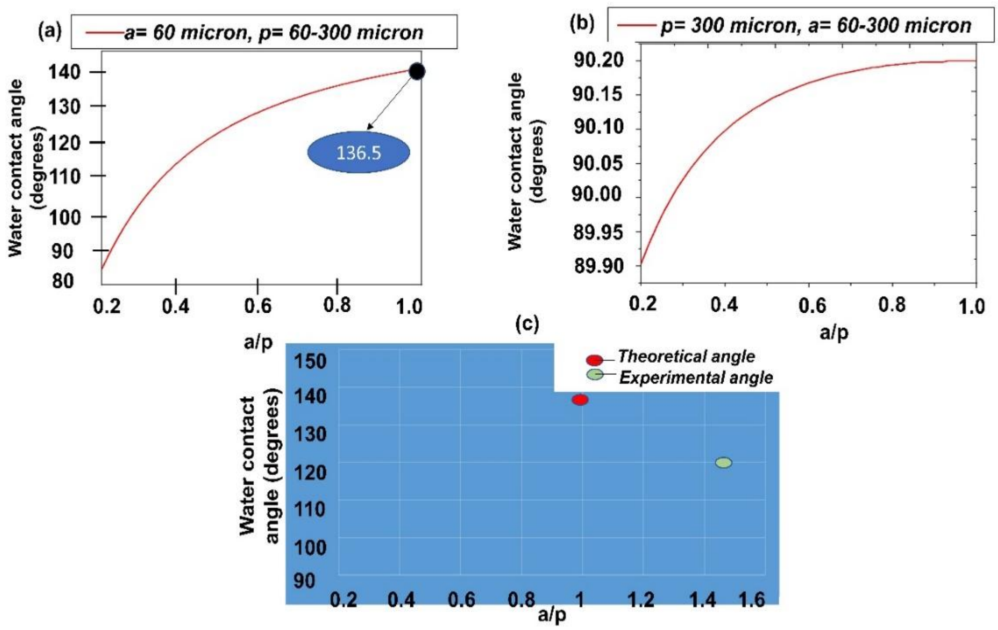

Fig. 5.7. For the simulated results, a graphical representation of water contact angle and aspect ratio (a) for 'a' is fixed and 'p' tends to fluctuate; (b) for 'p' is fixed and 'a' tends to vary; and (c) a graphical display highlighting the discrepancy between theoretical and experimental results.

5.8. Comparative study on mathematical modelling:

Below is a comparative study presented in the form of mathematical equation, illustrating the significance of aspect ratio and pillar size in achieving favourable results in terms of water contact angle:

An array of structures with square pillars and cylindrical pillars are shown in fig. 5.8 (a) and 5.8 (b).

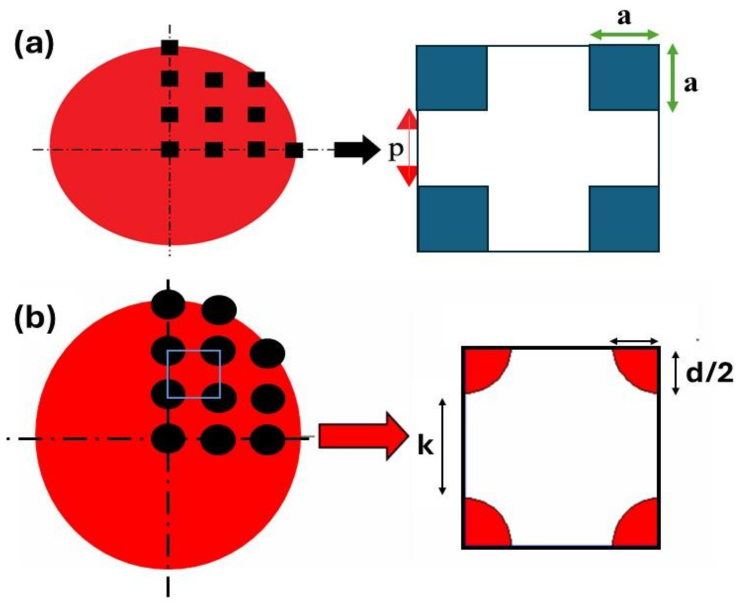

Fig. 5.8. Array of structures (a) for square pillars; (b) for cylindrical pillars.

Equation 5.6 serves as the reference for square-pillared structures:

$$\left(\frac{4}{3}\pi R_0^3\right)\rho g = \left[R_0 sin\theta + R_0 - \frac{p^2}{12}\left(\frac{R_0 cos\theta}{p} + \frac{a}{p} + 1\right)\left(\frac{R_0 cos\theta}{p} + \frac{2a}{p} + 2\right)\right]\frac{a^2.\pi}{p^2}\frac{R_0^2 cos^2\theta}{\left(\frac{a}{p}+1\right)^2}.\rho g + \frac{\pi R_0^2 cos^2\theta}{p^2\left(\frac{a}{p}+1\right)^2}.4a.t.\sin\left[\cos^{-1}\left\{\frac{p}{2\left[\left(\frac{p}{2}\right)^2+\left\{\frac{1}{2V}\left[\left(\frac{p}{2}\right)^2-V^2\right]^2\right\}^{\frac{1}{2}}\right]}\right.\right] + 2\pi R_0 T cos^2\theta \quad (5.11)$$

For the simplification, assume $\sin\theta = x,\ \cos\theta = \sqrt{(1-x^2)}$, $A = \frac{a}{p}$ and $B = \frac{p}{2}$ to obtain the following expression:

$$\frac{4R_0^3.\rho.g}{3} = \Bigg[R_0 x + R_0 - \frac{p^2}{12}\Bigg(\frac{R_0(1-x^2)}{p^2} + \frac{3(A+1)R_0\sqrt{1-x^2}}{p} + 2(A+1)^2\Bigg)\Bigg].\frac{A^2R_0^2(1-x^2)\rho g}{(A+1)^2} + \frac{R_0^2(1-x^2)}{p^2(A+1)^2}.4a.Tsin[\cos^{-1}\left\{\frac{p}{2\sqrt{(B)^2+[\frac{1}{2V}\{(B)^2-V^2\}^2]}}\right\} + 2R_0T(1-x^2) \quad (5.12)$$

Upon solving the aforementioned expression, we obtain the subsequent expression:

$$x = \Bigg[\frac{4}{3}\frac{(A+1)^2}{A^2(1-x^2)} - 1 + \frac{B^2}{3R_0}\Bigg(\frac{R_0(1-x^2)}{p^2} + \frac{3(A+1)R_0\sqrt{1-x^2}}{p} + \frac{3(A+1)R_0\sqrt{1-x^2}}{p} + 2(A+1)^2\Bigg)\Bigg] - \frac{(A+1)^2}{A^2R_0}\frac{1}{B^2\rho g}a.T\sin[\cos^{-1}\left\{\frac{B}{\sqrt{(B)^2+\left[\frac{1}{2V}\{(B)^2-V^2\}^2\right]}}\right\} - \frac{2T}{R_0\rho g}.\frac{(A+1)^2}{A^2} \quad (5.13)$$

Finally, the contact angle θ can be computed for square pillared structures as:

$$\theta = sin^{-1}\left[\frac{4}{3}\frac{(A+1)^2}{A^2\sqrt{1-x^2}} - 1 + \frac{B^2}{3R_0}\left(\frac{R_0\sqrt{1-x^2}}{p^2} + \frac{3(A+1)R_0(1-x^2)}{p} + \frac{3(A+1)R_0(1-x^2)}{p} + 2(A+1)^2\right)\right] - \frac{(A+1)^2}{A^2R_0}\frac{1}{B^2\rho g}.a.T\sin[\cos^{-1}\left\{\frac{B}{\sqrt{(B)^2 + \left[\frac{1}{2V}\{(B)^2 - V^2\}^2\right]}}\right\} - \frac{2T}{R_0\rho g}.\frac{(A+1)^2}{A^2}$$

(5.14)

The following values were taken into account for the computation of θ:

$a = 15.07 \times 10^{-6}$ m, $R_0 = 0.003$ m, $p = 14.80 \times 10^{-6}$ m, $g = 9.8$ m/s^2, $V = 0.001$ m and $\rho = 997$ kg/m^3, g= 9.8 m/s^2, A= a/p = 1.01 = aspect ratio, B= p/2 = 7.4

Similarly, equation 5.6 serves as the reference for cylindrical pillared structures:

$$\left(\frac{4}{3}\pi R_0^3\right)\rho g = \left[R_0 sin\theta + R_0 - \frac{p^2}{12}\left(\frac{R_0 cos\theta}{p} + \frac{d}{2} + k\right)\left(\frac{R_0 cos\theta}{p} + \frac{2a}{p} + 2\right)\right]\frac{a^2.\pi}{p^2}\frac{R_0^2cos^2\theta}{\left(\frac{a}{p}+1\right)^2}.\rho g + \frac{\pi R_0^2 cos^2\theta}{p^2\left(\frac{d/2}{p}+1\right)^2}.4a.t.\sin\left[\cos^{-1}\left\{\frac{p}{2\left[\left(\frac{p}{2}\right)^2 + \left\{\frac{1}{2V}\left[\left(\frac{p}{2}\right)^2 - V^2\right]^2\right\}^{\frac{1}{2}}\right]}\right\}\right] + 2\pi R_0 T cos^2\theta \quad (5.15)$$

Assume $\sin\theta = x$, $\cos\theta = \sqrt{(1-x^2)}$, $A = \frac{d}{2k}$ and $B = \frac{k}{2}$ to obtain the following expression:

Finally, the contact angle θ can be computed for cylindrical pillared structures as:

$$\theta = sin^{-1}\left[\frac{4}{3}\frac{(\frac{d}{2k}+1)^2}{(\frac{d}{2k})^2\sqrt{1-x^2}} - 1 + \frac{\frac{k^2}{2}}{3R_0}\left(\frac{R_0\sqrt{1-x^2}}{k^2} + \frac{3(\frac{d}{2k}+1)R_0(1-x^2)}{k} + \frac{3(\frac{d}{2k}+1)R_0(1-x^2)}{k} + 2(\frac{d}{2k}+1)^2\right)\right] - \frac{\left(\frac{d}{2k}+1\right)^2}{A^2R_0}\frac{1}{\frac{k^2}{2}\rho g}.\frac{d}{2}.T\sin[\cos^{-1}\left\{\frac{\frac{k}{2}}{\sqrt{\left(\frac{k}{2}\right)^2+\left[\frac{1}{2V}\left\{\left(\frac{k}{2}\right)^2-V^2\right\}^2\right]}}\right\} - \frac{2T}{R_0\rho g}.\frac{(\frac{d}{2k}+1)^2}{(\frac{d}{2k})^2} \quad (5.16)$$

The following values were taken into account for the computation of θ:

$d/2 = 10\times10^{-6}$ m, $R_0 = 0.003$ m, $k = 10\times10^{-6}$ m, $g = 9.8$ m/s^2, $V = 0.001$ m and $\rho = 997$ kg/m^3, g= 9.8 m/s^2 , A= a/k= d/2k= 1.0×10^{-6} m = aspect ratio, B= k/2 = 5×10^{-6} m

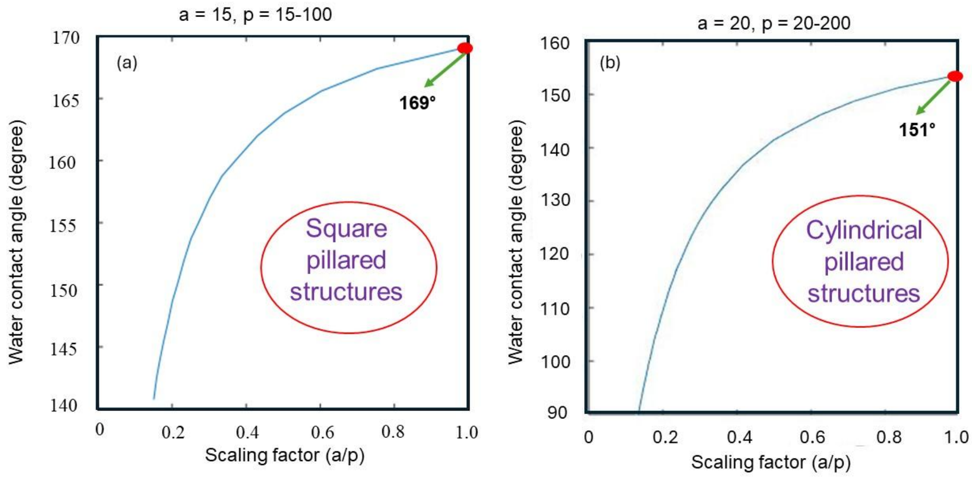

Fig. 5.9. A graphical depiction of the water contact angle and aspect ratio for "a" is fixed for the simulated results, whereas "p" tends to vary for (a) square pillared structures and (b) cylindrical pillared structures.

Table 5.2. Detailed mathematical modelling comparison between the earlier work and current study.

Ref.	Shape	Method Used	Concept	Pillar size (µm)	Spacing between pillar (µm)	Aspect ratio	Theoretically predicted water contact angle
Earlier work [22]	Square shaped pillars	Force balance method on water droplet	Behavior of water drops on a square shape pillared array surface to understand the surface's wetting regime.	60	85	0.71	132.8^0
				120	120	1	126.7^0
				185	320	0.58	94.68^0
				50	50	1	143.6^0
				25	25	1	154.1^0
Current study				15.07	14.80	1.01	168.5^0

[183]	Diamond shaped pillars	Force balance method on water droplet	Behavior of water droplets on a diamond shape-pillared array surface.	45	45	1	166.24^0
Earlier work [184]	Cylindrical shaped pillars	Force balance method on water droplet	Behavior of water droplets cylindrical shape-pillared array surface.	50 100 200	50 100 200	1 1 1	138.60^0 123.5^0 104.8^0
Current study				10	10	1	152.5^0

Current study	Rectangular shaped pillars	Force balance method on water droplet	Behavior of water droplets rectangular shape-pillared array surface.	47	35.04	1.34	136.6^0

The size and aspect ratio of pillars significantly influences the surface's wetting properties. Pillars with an optimal aspect ratio produce a rougher surface, enhancing hydrophobicity and increasing contact angles. The arrangement and dimensions of the pillars can trap air pockets beneath a water droplet, leading to the Cassie-Baxter state, where the droplet has minimal contact with the solid surface, maintaining a higher contact angle. The shape of surface microstructures significantly influences the wetting behavior of textured surfaces. Square pillars exhibit a higher contact angle (CA) than cylindrical pillars due to differences in air entrapment, solid-liquid contact area, and contact line pinning as shown in fig 5.9. In the Cassie-Baxter state, square pillars trap more air, reducing liquid contact, while cylindrical pillars allow greater liquid infiltration. Additionally, the sharp edges of square pillars enhance contact line pinning, preventing droplet spreading, whereas the smooth curvature of cylindrical pillars facilitates wetting. Also, the geometry of the pillars affects the droplet's stability, and an optimal pillar size and aspect ratio ensures the droplet remains stable with a higher contact angle, reducing the likelihood of spreading or collapsing. An aspect ratio of 1 is optimal, achieving a balanced width-to-spacing ratio and ideal surface roughness. The balance between height and width optimizes surface roughness, air trapping, and energy barriers. This balance enhances hydrophobicity, resulting in higher water contact angles. At this ratio, pillars effectively trap air pockets beneath the droplet, reducing solid contact and promoting the Cassie-Baxter state. Uniform and consistent energy barriers at an aspect ratio of 1 maintain the droplet's spherical shape, preventing it from spreading and lowering the contact angle. This ratio provides a symmetrical and stable platform, ensuring droplet stability and contributing to a higher contact angle. These factors make square pillars more effective in achieving higher hydrophobicity

5.9. Adhesion Force Analysis for Different Surface Textures:

The adhesion force of a water droplet on a textured surface is influenced by the contact angle and contact diameter. In this study, the adhesion force was computed for different surface textures, including rectangular, square, and cylindrical pillar structures. The adhesion force ('F') is determined using the following equation:

$$F= \gamma_{LV}.d.(1+\cos\theta) \tag{5.17}$$

where γ_{LV} is the surface tension of water (72.8 N/m), d is the contact diameter (10.2 mm), and θ is the contact angle for each surface type.

Table 5.3 The calculated adhesion forces for different surface textures are as follows:

Surface Type	Contact Angle (θ)	Adhesion Force (Nm)
Rectangular (Experimental)	123.7°	330.55
Rectangular (Theoretical)	136.6°	203.03
Square	169°	13.64
Cylindrical	151°	93.10

Higher adhesion force for experimental rectangular pillars: The discrepancy between experimental (330.55 Nm) and theoretical (203.03 Nm) values suggests that surface imperfections, burr formation, or deviations in aspect ratio may have increased the solid-liquid contact area. Lower adhesion force for square pillars: The square pillars exhibit the lowest adhesion force of 13.64 Nm due to enhanced air entrapment, reducing the solid-liquid interface and making the surface more hydrophobic. Moderate adhesion force for cylindrical pillars:

The cylindrical pillars have an adhesion force of 93.10 Nm, which is higher than square but lower than rectangular, indicating that their continuous curvature allows more liquid penetration than square but less than rectangular pillars. Effect of contact angle: Surfaces with a higher contact angle exhibit a lower adhesion force, which is desirable for self-cleaning applications as droplets roll off more easily. The study confirms that surface texture significantly impacts droplet adhesion. Square pillars offer superior hydrophobicity with minimal adhesion, while rectangular pillars, particularly in experimental cases, demonstrate higher adhesion due to increased wettability. These findings emphasize the importance of optimizing surface geometry for applications such as self-cleaning, anti-icing, and drag reduction coatings.

Further research could involve experimental validation of adhesion forces using force measurement techniques to refine theoretical models and improve surface design strategies.

5.10. CONCLUSIONS

Force balanced system based mathematical model is modified for rectangular pillared array based micro-structure to anticipate the relationship between the water contact angle and other geometrical parameters that influence the wettability conditions. The theoretical model suggested a water con tact angle of 136.6° whereas, the average experimental water contact angle of 123.7° ± 3° was achieved on the textured Al substrate. Compared to hydrophilic non-textured Al, the textured Al exhibited the hydrophobic character. The variation in theoretical and experimental water contact angles of textured Al surface is caused by machining issues like depth of cut, tool feed rate and other factors. Such type of research can motivate the researchers towards better understanding of the scientific principles behind the wetting mechanisms of textured surfaces, which are imperative to develop economical, real-world self-cleaning materials.

CHAPTER 6. MICRO-TEXTURED ETFE FOR SELF-CLEANING APPLICATIONS

6.1. ABSTRACT

In recent years, self-cleaning surfaces have garnered significant attention for their wide-ranging applications. Ethylene tetrafluoroethylene (ETFE) has emerged as an alternative material for covering solar panels instead of traditional glass coverings. However, bare ETFE lacks inherent self-cleaning properties, which restricts its applications in the self-cleaning phenomenon. Herein, we utilized a novel single-point diamond turning (SPDT) machining technique to create a micro-textured surface on ETFE. The micro-textured ETFE surface exhibited a water contact angle of 141.2°, indicating a high degree of self-cleaning ability. We used a variety of characterization tool to evaluate the resulting surface and its wetting characteristics, including field-emission scanning electron microscopy (FESEM), drop shape analysis (DSA), x-ray diffraction (XRD), a self-cleaning test, Fourier-Transform Infrared Spectroscopy (FTIR) and UV-Visible spectrophotometer test. Moreover, the micro and nano-texturing applied to ETFE can further enhance the surface properties. These modified surfaces hold great promise for diverse industrial applications where self-cleaning properties are highly desirable.

6.2. HIGHLIGHTS

1. The micro-texturing of ETFE has improved the material's surface qualities.
2. The experimental results are validated using FESEM, DSA, XRD, and FTIR.
3. Textured ETFE surfaces exhibit resistance to the accumulation of dirt.

6.3. INTRODUCTION

The development of advanced materials with remarkable surface properties has gained significant attention in various fields ranging from aerospace engineering to biomedical applications. Ethylene tetrafluoroethylene (ETFE) is a versatile fluoropolymer that has attracted significant attention in various industries owing to its exceptional mechanical, chemical, and thermal properties [185-186]. ETFE has been extensively studied owing to its unique surface properties, specifically its ability to exhibit hydrophobic behavior [187]. Superhydrophobic surfaces possess the distinct property of repelling water droplets with a high contact angle of 150°. These surfaces have attracted considerable interest for a wide range of applications, including antifouling coatings, anti-icing surfaces, and energy-efficient heat exchangers. Superhydrophobic surface's self-cleaning process lies in the dual-action process of water droplet rolling and contaminant removal [188-192]. When water droplets meet the surface, they form nearly spherical shapes and roll off effortlessly, carrying away dust, dirt, and other pollutants. Low adhesion between water and the superhydrophobic surface facilitates this rolling effect, resulting in a self-cleaning effect that reduces the need for manual cleaning or the use of harsh chemical cleaning agents [193].

ETFE is an ideal material for applications in which structural integrity and self-cleaning qualities are desired owing to its exceptional durability, lightweight design, and high resistance to environmental degradation [194-196]. Owing to their outstanding combination of mechanical characteristics and transparency, researchers are currently focusing on utilizing ETFE as a superhydrophobic material. Furthermore, owing to its transparency, it can be used on the exterior of buildings and architecture, where self-cleaning surfaces may provide considerable maintenance advantages [197].

However, the inherent smoothness of ETFE surfaces limits their potential for certain applications that require enhanced functionalities such as improved friction, optical properties, and superhydrophobicity [198]. To overcome this limitation, micro-texturing of ETFE surfaces using advanced manufacturing techniques such as SPDT machining. This machining is a precise and controlled manufacturing technique that utilizes a diamond-tipped tool to remove material from a workpiece with sub-micrometre accuracy [199]. This is a critical technology in the field of precision optics, allowing for the manufacturing of top-quality optical components that are utilized in a range of industries, including sensors, mirrors, and microelectromechanical systems (MEMS) as well as components for aerospace and defence applications [200-202]. SPDT is widely recognized for its remarkable precision, allowing it to manufacture components with demanding tolerances at the submicron and even nanometre level. This process not only produces exceptional surface finishes, but it also minimizes the need for additional polishing or finishing steps. SPDT can be used on a variety of materials, such as metals, plastics, and certain types of glass. Its ability to machine complex and freeform geometries makes it an attractive alternative to other manufacturing methods. Furthermore, SPDT's direct machining capabilities can significantly reduce the lead time for producing optical components compared to conventional methods. SPDT is especially useful for working with softer materials, but some fabrication challenges occur when working with hard and brittle materials. Also, the use of diamond tools can result in wear over time, which can negatively impact the quality of the machined surfaces. Additionally, achieving high precision can be a time-consuming process, especially when dealing with large and intricate components. In recent years, SPDT machining has been adapted for the micro-texturing of polymers, including ETFE, to create tailored surface topographies, enabling the enhancement of specific surface properties.

This study aimed to explore the use of ETFE for self-cleaning purposes, specifically focusing on its hydrophobic properties.

This paper aims to explore micro-texturing ETFE via SPDT machining and its impact on surface properties. Additionally, the paper will investigate the effect of different micro-texture designs on specific surface properties, and wettability. The enhanced surface properties achieved through SPDT machining could lead to improved performance in areas such as microfluidics, optical devices, biomimetic surfaces, and self-cleaning coatings.

In conclusion, micro-texturing of ETFE via Single Point Diamond Turning machining offers a novel approach to overcome the limitations of smooth ETFE surfaces. By tailoring the micro-texture design and parameters, researchers can explore the full potential of ETFE in various industries, opening new possibilities for advanced materials and technologies.

6.4. EXPERIMENTAL DETAILS

6.4.1. MATERIAL

ETFE (ethylene tetrafluoroethylene) from Daikin Chemicals, UK was utilized in this investigation. The specimens had a diameter of 5 mm. The ETFE substrate underwent a cleaning process, first in an ultrasonic cleaner with acetone, followed by a rinse with deionized water.

6.4.2. Single-point diamond turning (SPDT) machining setup:

To fabricate precisely ordered microstructures on the surface of the ETFE, a single-point diamond turning machining (a multi-axis Precitech 700G ultra-precision machine tool) technique was employed. The experimental setup for the SPDT machining technique is shown in Fig. 6.1. The diamond tools were strategically positioned on a rotary axis mounted above a linear axis, which provided the necessary feed for the machining process. To ensure a high-quality surface finish during machining, the workpiece was aligned so that its face matched the vertical axis. Notably, a diamond tool featuring a cutting nose radius of 0.1 mm was employed. This tool is attached to an actuator that controls its movement with precision. As the diamond tool encounters the rotating workpiece, material is removed through a process of abrasion. The level of precision achieved in this process allows for the creation of optical surfaces with nanometre-level accuracy. A camera was attached to the machining setup to ensure that the fabrication process was proceeding without any interruptions.

6.4.3. Fabrication of microstructures on ETFE surface:

Schematic illustration of SPDT machining technique is shown in Fig. 6.2. Initially, bare ETFE was chosen as the fabrication material, as depicted in Fig. 6.2(a). The wedge was removed out of the ETFE surface using a high-quality diamond tool on both sides as shown in Fig. 6.2(b). The machining process began with the first cut, aligning the sample with the spindle, creating single-scale texturing as shown in Fig. 6.2(c). Afterward, an additional cut was made by rotating the sample by 90°, as depicted in Fig. 6.2(d), resulting in double-scale texturing on the workpiece, as illustrated in Fig. 6.2(e). Fig. 6.2 (f) presents an enlarged three-dimensional view of the micro-pillared structures that are fabricated on ETFE surface. Table 6.1 presents the specifications for the fabrication process, which includes the dimensions and arrangement of microstructures, as well as the details of the machining process. Clairsol-300 served as the coolant, maintaining a consistent cooling environment throughout the machining process. Following this, an ultrasonic bath was employed in a thorough cleaning process to eliminate any remaining residue or debris resulting from the machining. The measurement of the water contact angle on the textured ETFE surface is depicted in Fig. 6.2(g).

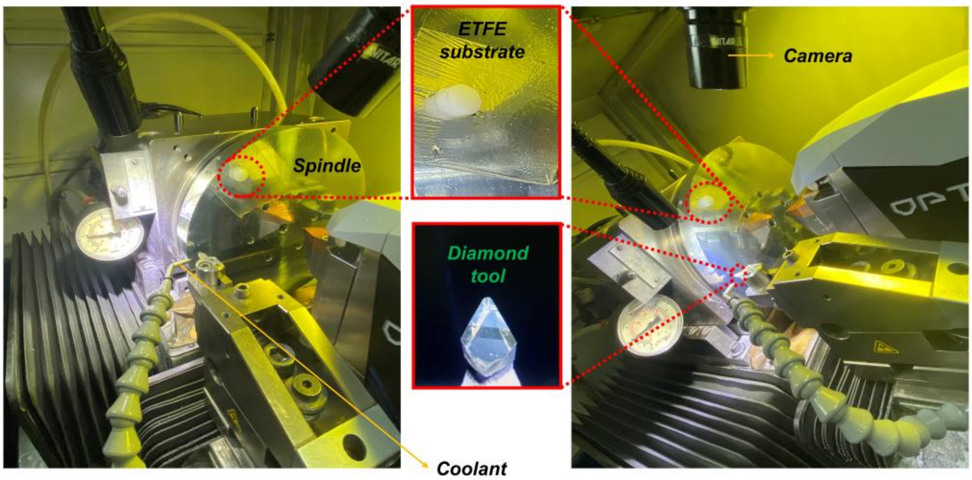

Fig. 6.1. The experimental setup for the SPDT machining technique.

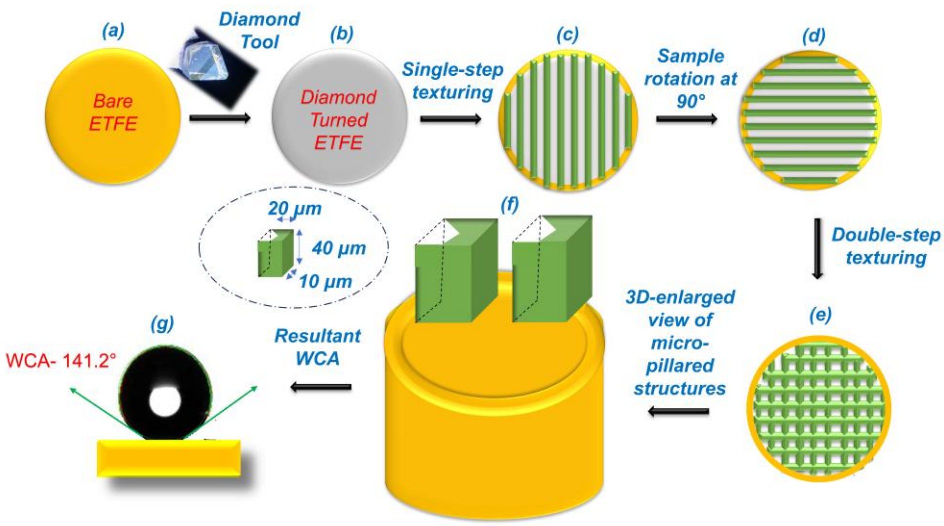

Fig. 6.2. Schematic illustration of SPDT machining technique.

Table 6.1 Specifications for fabrication and machining setup.

S.No.	Specifications	Machining parameters
1.	Diamond tool	Single crystal
2.	Nose radius	0.2 mm

3.	Rake angle	0º
4.	Spindle speed	1500 rpm
5.	Tool feed rate	1.5 µm/rev
6.	Clearance angle	10 º
7.	Depth of cut	5 µm
8.	Pitch of microstructure	10 µm
9.	Height of microstructure	40 µm
10.	Width of microstructure	20 µm

6.4. CHARACTERIZATIONS

Field emission scanning electron microscope (FESEM, Zeiss, Gemini, Carl Zeiss) analysis was used to examine surface morphology and microstructure of the machined ETFE film, offering high-resolution images to visualize any defects, grooves, or irregularities induced by the SPDT process. The Drop Shape Analyzer (DSA 25; Kruss GmbH, Germany) was employed to measure the surface energy and contact angle of the ETFE film, providing insights into its wettability and surface hydrophobicity. A self-cleaning test was conducted on an ETFE surface using a water syringe, after sprinkling fine powder on it. This test provides useful information about the ETFE material's ability to repel and shed contaminants, making it a valuable evaluation for applications where a clean surface is essential. FTIR spectroscopy (Spectrum-two instrument from Perkin Elmer (2012) and operating within a temperature range of 5-25°C, serves as a highly useful tool for examining both plain and textured ETFE materials. This technique provides in-depth information on their chemical makeup, molecular structures, and surface characteristics. An ETFE sample measuring 2mm by 2mm and a maximum of 1 inch was utilized for the testing process.

6.5. RESULTS AND DISCUSSION

The microstructure and surface morphology of the micro-textured ETFE fluoropolymer at various magnifications are shown in Fig. 6.3(a). Fig. 6.3(b,c) depicts the bulged area for the micro-textured ETFE surface. The results showed that the micro-textured surface displayed smooth and well-defined structures with minimal signs of defects or irregularities. The absence of surface imperfections such as scratches or grooves indicates the high precision and accuracy of the SPDT machining process. The FESEM images also demonstrated that machining did not cause any significant damage to the overall structure of the ETFE fluoropolymer, indicating the preservation of material integrity during the machining process.

Fig. 6.3(d) displays a WCA of 96.4° on the untreated ETFE substrate, while Fig. 6.3(e) demonstrates a higher WCA of 141.2° on the micro-textured ETFE surface. The results revealed that the micro-textured surface exhibited excellent surface properties facilitating low adhesion of liquids. Plastic deformation can alter the density of defects, including dislocations and grain boundaries, while introducing residual stresses that influence the material's surface energy. Even without micropillar formation, plastic deformation can generate nanoscale roughness, impacting wettability through the Wenzel or Cassie-Baxter models. In ETFE, SPDT can induce molecular reorientation, exposing fluorine-rich regions that further decrease surface energy due to fluorine's inherently low surface energy. If SPDT smooths the surface and reduces nanoscale roughness, the contact area between the liquid and solid diminishes, further lowering surface energy. Additionally, SPDT may create micropillars, promoting a Cassie-Baxter state where trapped air pockets significantly increase the contact angle beyond the effects of surface energy changes alone. While micropillars primarily influence roughness, surface energy modifications due to plastic deformation may also contribute to wettability changes. As, micro textures trap air pockets beneath the droplet, forming a composite interface of solid, liquid, and air which decreases the solid-liquid contact area and increases the apparent contact angle, making it easier for the droplet to roll off at lower tilt angles. According to the Wenzel model, surface roughness amplifies the inherent wettability of the material. Whereas, In the Cassie-Baxter state, the droplet sits on top of the microstructure, further enhancing hydrophobicity. The improved wetting behavior of the micro-textured surface can be attributed to the smooth and defect-free surfaces achieved through SPDT machining. This transition signifies a change from a less hydrophobic to a significantly more hydrophobic wetting regime. It suggests that there is a potential to improve the contact angle by optimizing the tool components. The result validates that this machining technique is suitable for producing high-quality micro-textured ETFE fluoropolymer without disturbing its molecular structures.

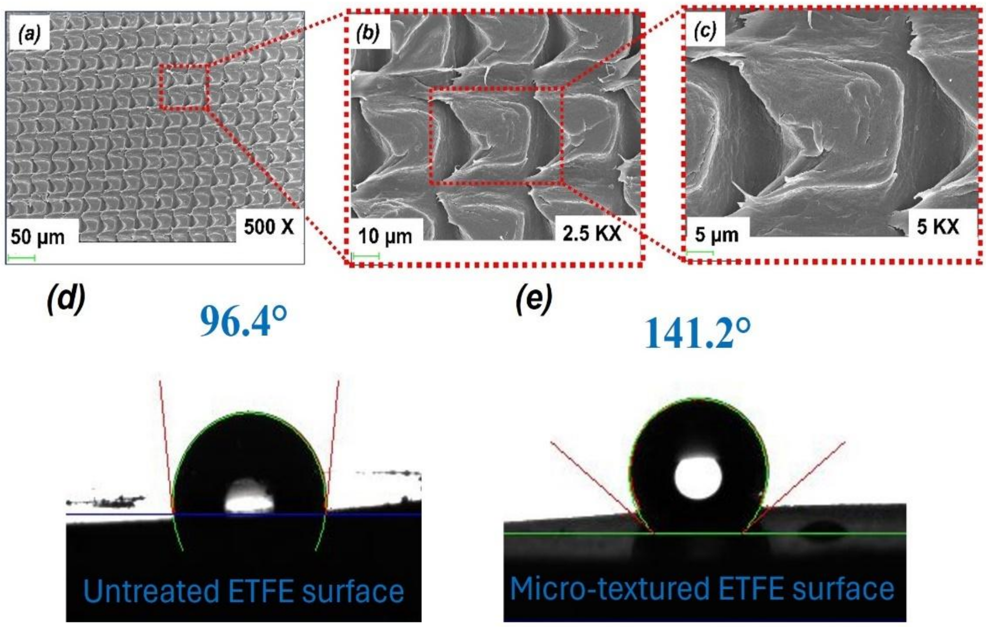

Fig. 6.3. FESEM images (a) at 50 µm, (b,c) bulged area; Water contact angle: (d) for the untreated ETFE surface, (e) for the micro-textured ETFE surface,

Fig. 6.4 illustrates the self-cleaning behavior of a micro-textured ETFE surface compared to an untreated ETFE surface. In this experiment, fine dust powder was sprinkled onto both surfaces, as shown in Fig. 6.4(a) and 6.4(c). When water droplets were placed on the soiled surfaces, the untextured ETFE did not show any self-cleaning behavior, as the droplets stick on the surface, as depicted in Fig. 6.4(b). However, the micro-textured ETFE surface displayed self-cleaning behavior as the droplets rolled off, removing the fine dust particles, and resulting in a nearly completely clean surface, as shown in Fig. 6.4(d). Therefore, the self-cleaning performance is determined by assessing how effectively the water removes or repels the fine powder from the ETFE material. This experiment provides insightful information about the dynamic interplay between water and ETFE, advancing our knowledge of the material's self-cleaning capabilities in practical settings.

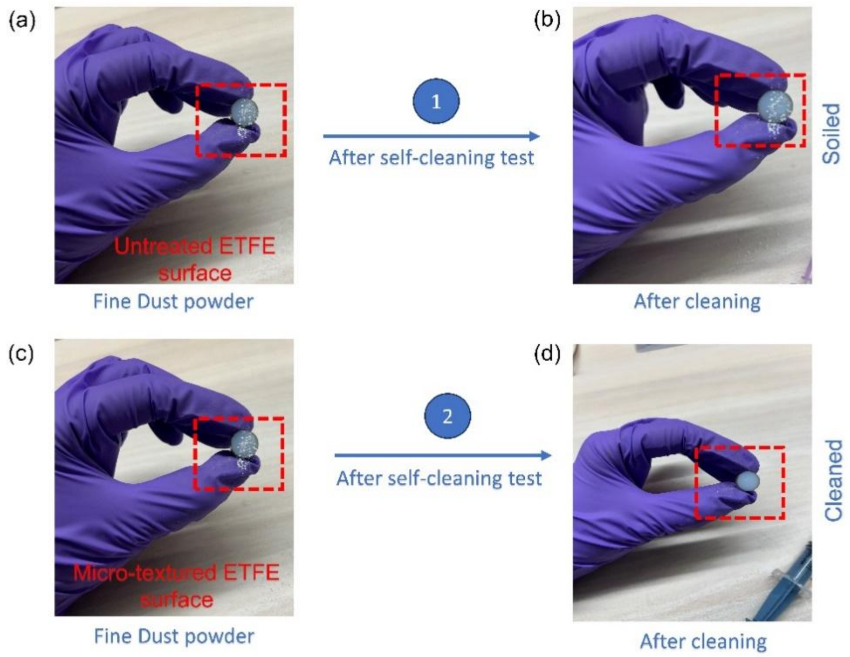

Fig. 6.4. Self-cleaning test: (a) an untreated ETFE surface was tested with fine dust powder, (b) dust powder remained on the surface after the test, (c) fine dust powder sprinkled on micro-textured ETFE surfaces, (d) after the test, water droplets rolled off, taking the dust powder with them.

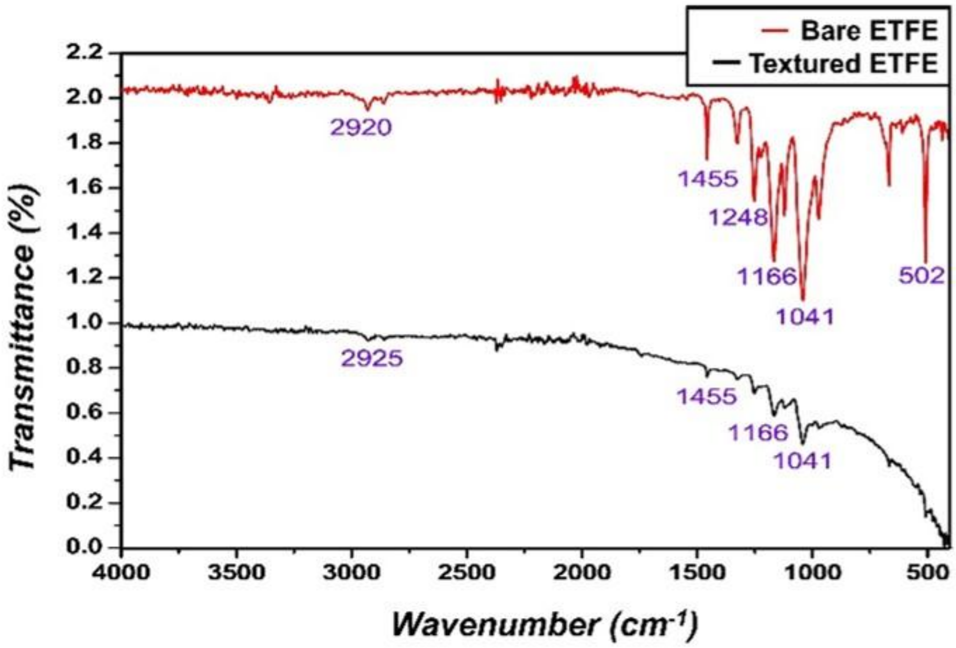

Fig. 6.5. FTIR spectrum of bare and textured ETFE sample.

The FTIR spectrum of both bare and textured ETFE is shown in the Fig. 6.5. The FTIR spectra of bare and textured ETFE surfaces are generally expected to be similar in terms of chemical composition but may show subtle differences due to surface modifications caused by texturing. As, ETFE is chemically inert, meaning its fundamental molecular structure C–C and C–F bonds remain unchanged after texturing. Texturing can locally alter polymer chain orientation, leading to slight shifts in peak intensities. Both bare and textured ETFE exhibit C-H stretching vibrations in the range of 2800-3000 cm^{-1}, although these peaks may be relatively weak due to the dominance of fluorine atoms in the polymer backbone [201]. The peak around 1100-1300 cm^{-1} corresponds to the stretching vibrations of carbon-fluorine C-F bonds in both cases, which distinguishes ETFE from other common polymers. Weak peaks around 1400-1500 cm^{-1} indicate C-H and C-C bending vibrations in both cases [202]. However, there is no difference in the chemical composition and molecular structural properties between bare and textured ETFE, indicating that the textured ETFE surface offers insights into the molecular bonds and arrangements present in the bare ETFE material.

6.6. Conclusions

In our study, we utilized single-point diamond turning machining to fabricate a uniform array of microstructures on the surface of ETFE. This engineered surface exhibited exceptional qualities, including a well-defined surface morphology, self-cleaning capabilities, and suitable thermal properties, making it ideal for use in self-cleaning energy systems. By altering the ETFE surface, we achieved a WCA of approximately 141°, which is a good result that was only achieved through micro texturing. Our results have the potential to advance the design of diverse hierarchical patterns and enhance surface wettability, furthering the field of materials engineering. Future research should focus on combining both micro/nano texturing techniques on the ETFE surface.

CHAPTER 7: CONCLUSIONS AND FUTURE SCOPE

7.1. CONCLUSIONS

- A mathematical model utilizing a force-balanced system was applied to rectangular pillared array microstructures, and MATLAB simulations were performed to investigate the relationship between the water contact angle and various geometric parameters affecting wettability.
- The theoretical model forecasted a water contact angle of 136.6°, whereas the textured aluminium substrate displayed an average experimental contact angle of 123.7° ± 3°. In contrast to the hydrophilic, non-textured aluminium, the textured aluminium exhibited hydrophobic characteristics. The discrepancies between the theoretical and experimental contact angles on the textured aluminium surface are attributed to machining variables, including tool feed rate, depth of cut, and other related factors.
- Advanced functional mechanisms were examined to elucidate the dynamic behavior of droplets on superhydrophobic surfaces. The study compared theoretical predictions with experimental observations across different transitional wetting regimes, demonstrating that the Cassie-Baxter and Wenzel wetting states are induced by the high kinetic energy and impact velocity of the droplets.
- The study has been carried out on the relationship between water droplet size, volume, and surface roughness on textured surfaces, as well as their two metastable states.
- We employed single-point diamond turning machining to create a uniform array of microstructures on the surface of ETFE. This engineered surface demonstrated outstanding characteristics, including a precisely defined surface morphology, self-cleaning abilities, and wetting conditions. Bare ETFE possesses a water contact angle of 96.4°

while through surface modification of ETFE, we attained a water contact angle of around 141° using a single step texturing. This transition signifies a change from a less hydrophobic to a significantly more hydrophobic wetting regime. It suggests that there is a potential to improve the contact angle by optimizing the tool components.

7.2. FUTURE SCOPE

- Future studies should concentrate on improving the structural design and fabrication of complex micro/nanostructures on ETFE surfaces using cutting-edge mathematical modelling techniques. In this optimization process, parameters such as dimensions, structural shapes, and arrangement of micro/nanostructures could be refined to increase the efficiency of self-cleaning.
- Future research could investigate the feasibility and practicality of applying self-cleaning ETFE surfaces with hierarchical structures that are guided by mathematical models in various real-world settings. This could involve working with industry partners to incorporate these self-cleaning properties into a range of applications, such as architectural, automotive surfaces, or solar panels.
- The evaluation of the mechanical strength, chemical stability, and weather resistance of micro-textured ETFE surfaces can be studied in future. This would ensure their performance in various environmental conditions.
- Future research could explore the fabrication of nanostructures using single-point diamond turning machining, as this holds significant promise for advancing optical industries.
- The integration of self-cleaning ETFE polymer with emerging technologies such as artificial intelligence (AI) could lead to innovative applications. Further research could delve into the potential of using

these surfaces in conjunction with sensors and actuators to create autonomous cleaning systems, or how AI algorithms can enhance cleaning approaches by making use of real-time environmental data.

- Exploring other conventional machining setups, such as electron beam lithography, in addition to single-point diamond turning machining, could yield promising results for the fabrication of complex structures.

REFERENCES

[1] Hooda, A., Goyat, M. S., Pandey, J. K., Kumar, A., & Gupta, R. (2020). A review on fundamentals, constraints and fabrication techniques of superhydrophobic coatings. *Progress in Organic Coatings*, *142*, 105557. https://doi.org/10.1016/j.porgcoat.2020.105557

[2] Manoharan, K., & Bhattacharya, S. (2019). Superhydrophobic surfaces review: Functional application, fabrication techniques and limitations. *Journal of Micromanufacturing*, *2*(1), 59-78. https://doi.org/10.1177/2516598419836345

[3] Erbil, H. Y. (2020). Practical applications of superhydrophobic materials and coatings: problems and perspectives. *Langmuir*, *36*(10), 2493-2509. https://doi.org/10.1021/acs.langmuir.9b03908

[4] M. Paven, L. Mammen, D. Vollmer, Challenges and Opportunities of Super hydrophobic/superamphiphobic Coatings in Real Applications, 2016, https:// doi.org/10.1039/9781782622192-00209.

[5] Hooda, A., Goyat, M. S., Kumar, A., & Gupta, R. (2018). A facile approach to develop modified nano-silica embedded polystyrene based transparent superhydrophobic coating. *Materials Letters*, *233*, 340-343. https://doi.org/ 10.1016/j.matlet.2018.09.043.

[6] Barz, J., Haupt, M., Oehr, C., Hirth, T., & Grimmer, P. (2019). Stability and water wetting behavior of superhydrophobic polyurethane films created by hot embossing and plasma etching and coating. *Plasma Processes and Polymers*, *16*(6), 1800214. https:// doi.org/10.1002/ppap.201800214.

[7] Shamshiri, M., Jafari, R., & Momen, G. (2021). Potential use of smart coatings for icephobic applications: A review. *Surface and Coatings Technology*, *424*, 127656. https://doi.org/10.1016/j.surfcoat.2021.127656.

[8] Ferrari, M., Benedetti, A., Santini, E., Ravera, F., Liggieri, L., Guzman, E., & Cirisano, F. (2015). Biofouling control by superhydrophobic surfaces in shallow euphotic seawater. *Colloids and Surfaces A: Physicochemical and Engineering Aspects*, *480*, 369-375. https://doi.org/10.1016/j.colsurfa.2014.11.009.

[9] Liravi, M., Pakzad, H., Moosavi, A., & Nouri-Borujerdi, A. (2020). A comprehensive review on recent advances in superhydrophobic surfaces and their applications for drag reduction. *Progress in Organic Coatings*, *140*, 105537. https://doi.org/10.1016/j.porgcoat.2019.105537.

[10] Tang, M. K., Huang, X. J., Guo, Z., Yu, J. G., Li, X. W., & Zhang, Q. X. (2015). Fabrication of robust and stable superhydrophobic surface by a convenient, low-cost and efficient laser marking approach. *Colloids and Surfaces A: Physicochemical and Engineering Aspects*, *484*, 449-456. https://doi.org/ 10.1016/j.colsurfa.2015.08.029.

[11] Saji, V. S. (2020). Wax-based artificial superhydrophobic surfaces and coatings. *Colloids and Surfaces A: Physicochemical and Engineering Aspects*, *602*, 125132. https://doi.org/10.1016/j.colsurfa.2020.125132.

[12] Archer, R. J., Becher-Nienhaus, B., Dunderdale, G. J., & Hozumi, A. (2020). Recent progress and future directions of multifunctional (super) wetting smooth/structured surfaces and coatings. *Advanced Functional Materials*, *30*(26), 1907772. https://doi.org/ 10.1002/adfm.201907772.

[13] Ensikat, H. J., Ditsche-Kuru, P., Neinhuis, C., & Barthlott, W. (2011). Superhydrophobicity in perfection: the outstanding properties of the lotus leaf. *Beilstein journal of nanotechnology*, *2*(1), 152-161. https://doi.org/10.3762/bjnano.2.19.

[14] Han, D., & Moon, S. Y. (2015). Development of superhydrophobic surface on glass substrate by multi-step atmospheric pressure plasma treatment. *Thin Solid Films*, *587*, 34-38. https://doi.org/10.1016/j.tsf.2014.11.069.

[15] Abdulhussein, A. T., Kannarpady, G. K., Wright, A. B., Ghosh, A., & Biris, A. S. (2016). Current trend in fabrication of complex morphologically tunable superhydrophobic nano scale surfaces. *Applied Surface Science*, *384*, 311-332. https://doi.org/ 10.1016/j.apsusc.2016.04.186.

[16] Parvate, S., Dixit, P., & Chattopadhyay, S. (2020). Superhydrophobic surfaces: insights from theory and experiment. *The Journal of Physical Chemistry B*, *124*(8), 1323-1360. https://doi.org/10.1021/acs.jpcb.9b08567.

[17] Singh, S., Kango, S., Sharma, N., & Verma, R. (2021). Recent advances in the mechanical durability of superamphiphobic surfaces: A review. *Proceedings of the Institution of Mechanical Engineers, Part J: Journal of Engineering Tribology*, *235*(11), 2474-2499. https://doi.org/10.1177/ 13506501211004313.

[18] Gu, Y., Zhang, W., Mou, J., Zheng, S., Jiang, L., Sun, Z., & Wang, E. (2017). Research progress of biomimetic superhydrophobic surface characteristics, fabrication, and application. *Advances in Mechanical Engineering*, *9*(12), 1687814017746859. https://doi.org/10.1177/ 1687814017746859.

[19] Lima, A. C., & Mano, J. F. (2015). Micro-/nano-structured superhydrophobic surfaces in the biomedical field: part I: basic concepts and biomimetic approaches. *Nanomedicine*, *10*(1), 103-119. https://doi.org/10.2217/nnm.14.174.

[20] He, Q., He, W., Zhang, F., Zhao, Y., Li, L., Yang, X., & Zhang, F. (2022). Research progress of self-cleaning, anti-icing, and aging test technology of

composite insulators. *Coatings*, *12*(8), 1224. https://doi.org/10.3390/coatings12081224

[21] Park, S., Kim, J., & Park, C. H. (2015). Superhydrophobic textiles: review of theoretical definitions, fabrication and functional evaluation. *Journal of Engineered Fibers and Fabrics*, *10*(4), 155892501501000401. https://doi.org/10.1177/155892501501000401.

[22] Roy, T., Sabharwal, T. P., Kumar, M., Ranjan, P., & Balasubramaniam, R. (2020). Mathematical modelling of superhydrophobic surfaces for determining the correlation between water contact angle and geometrical parameters. *Precision Engineering*, *61*, 55-64. https://doi.org/10.1016/j.precisioneng.2019.10.005.

[23] Mortazavi, V., & Khonsari, M. M. (2017). On the degradation of superhydrophobic surfaces: A review. *Wear*, *372*, 145-157. https://doi.org/ 10.1016/j.wear.2016.11.009.

[24] Ghunem, R. A., Cherney, E. A., Farzaneh, M., Momen, G., Illias, H. A., Malagon, G. A. M., ... & Yin, F. (2022). Development and application of superhydrophobic outdoor insulation: A review. *IEEE Transactions on Dielectrics and Electrical Insulation*, *29*(4), 1392-1399. https://doi.org/10.1109/TDEI.2022.3183671.

[25] Ji, H., Chen, G., Yang, J., Hu, J., Song, H., & Zhao, Y. (2013). A simple approach to fabricate stable superhydrophobic glass surfaces. *Applied surface science*, *266*, 105-109. https://doi.org/10.1016/j.apsusc.2012.11.103.

[26] Trdan, U., Hočevar, M., & Gregorčič, P. (2017). Transition from superhydrophilic to superhydrophobic state of laser textured stainless steel surface and its effect on corrosion resistance. *Corrosion science*, *123*, 21-26. https://doi.org/ 10.1016/j.corsci.2017.04.005.

[27] Vahabi, H., Wang, W., Popat, K. C., Kwon, G., Holland, T. B., & Kota, A. K. (2017). Metallic superhydrophobic surfaces via thermal sensitization. *Applied Physics Letters*, *110*(25). https://doi.org/10.1063/1.4989577.

[28] Fu, Y., Soldera, M., Wang, W., Voisiat, B., & Lasagni, A. F. (2019). Picosecond laser interference patterning of periodical micro-architectures on metallic molds for hot embossing. *Materials*, *12*(20), 3409. https://doi.org/10.3390/ma12203409.

[29] Masato, D., Piccolo, L., Lucchetta, G., & Sorgato, M. (2022). Texturing Technologies for Plastics Injection Molding: A Review. *Micromachines*, *13*(8), 1211. https://doi.org/10.3390/mi13081211

[30] Muehlberger, M. (2022). Nanoimprinting of biomimetic nanostructures. *Nanomanufacturing*, *2*(1), 17-40. https://doi.org/10.3390/

[31] Le Brouster, R., Giboz, J., Nourdine, A., Tenchine, L., Dubelley, F., & Mele, P. (2022). Complementary approaches for enhancing polystyrene hydrophobicity: additives development and replication of micro/nanotextures. *Micromachines*, *13*(3), 467. https://doi.org/10.3390/mi13030467.

[32] Jucius, D., Lazauskas, A., Grigaliūnas, V., Guobienė, A., & Puodžiukynas, L. (2020). Hot embossing of micro-pyramids into thermoset thiol-ene film. *Polymers*, *12*(10), 2291. https://doi.org/10.3390/polym12102291.

[33] Guan, B., Pai, J. H., Cherrill, M., Michalatos, B., & Priest, C. (2022). Injection moulding of micropillar arrays: a comparison of poly (methyl methacrylate) and cyclic olefin copolymer. *Microsystem Technologies*, *28*(9), 2083-2091.https://doi.org/10.1007/s00542 022-05350-4.

[34] Minegishi, S., Ueda, N., Saito, M., Lee, J., & Fujima, T. (2022). Highly Water-Repellent and Anti-Reflective Glass Based on a Hierarchical

Nanoporous Layer. *Coatings*, *12*(7), 961. https://doi.org/10.3390/coatings12070961

[35] Liu, R., Cao, L., Liu, D., Wang, L., Saeed, S., & Wang, Z. (2023). Laser Interference Lithography—A Method for the Fabrication of Controlled Periodic Structures. *Nanomaterials*, *13*(12), 1818. https://doi.org/10.3390/ mi13071077.

[36] Nagappan, S., & Ha, C. S. (2015). Emerging trends in superhydrophobic surface based magnetic materials: fabrications and their potential applications. *Journal of Materials Chemistry A*, *3*(7), 3224-3251. https://doi.org/10.1039/C4TA05078A

[37] Qing, Y., Long, C., An, K., Hu, C., & Liu, C. (2019). Sandpaper as template for a robust superhydrophobic surface with self-cleaning and anti-snow/icing performances. *Journal of colloid and interface science*, *548*, 224-232. https://doi.org/10.1016/j.jcis.2019.04.040.

[38] Cohen, N., Dotan, A., Dodiuk, H., & Kenig, S. (2016). Superhydrophobic coatings and their durability. *Materials and Manufacturing Processes*, *31*(9), 1143-1155. https://doi.org/ 10.1080/10426914.2015.1090600.

[39] Jeevahan, J., Chandrasekaran, M., Britto Joseph, G., Durairaj, R. B., & Mageshwaran, G. J. J. O. C. T. (2018). Superhydrophobic surfaces: a review on fundamentals, applications, and challenges. *Journal of Coatings Technology and Research*, *15*, 231-250. https://doi.org/10.1007/ s11998-017-0011-x.

[40] Elvira, K. S., Gielen, F., Tsai, S. S., & Nightingale, A. M. (2022). Materials and methods for droplet microfluidic device fabrication. *Lab on a Chip*, *22*(5), 859-875. https:// doi.org/10.1039/d1lc00836f.

[41] Trinh, K. T. L., Thai, D. A., & Lee, N. Y. (2022). Bonding strategies for thermoplastics applicable for bioanalysis and diagnostics. *Micromachines*, *13*(9), 1503. https://doi.org/10.3390/mi13091503

[42] Chen, Y. (2015). Applications of nanoimprint lithography/hot embossing: a review. *Applied Physics A*, *121*, 451-465. https://doi.org/10.1007/ s00339-015-9071-x.

[43] Gao, J., Deng, Y., Peng, L., Yi, P., & Lin, Z. (2021). Water-repellent hierarchical microstructured PTFE films via micro powder hot embossing. *Journal of Materials Processing Technology*, *297*, 117261. https://doi.org/10.1016/j.jmatprotec.2021.117261.

[44] Scott, S. M., & Ali, Z. (2021). Fabrication methods for microfluidic devices: An overview. *Micromachines*, *12*(3), 319. https://doi.org/10.3390/mi12030319.

[45] Sun, J., Zhuang, J., Liu, Y., Xu, H., Horne, J., Wujcik, E. K., ... & Guo, Z. (2019). Development and application of hot embossing in polymer processing: a review. *ES Materials & Manufacturing*, *6*(12), 3-17. https://doi.org/10.30919/esmm5f605.

[46] Patil, D., Sharma, A., Aravindan, S., & Rao, P. V. (2019). Development of hot embossing setup and fabrication of ordered nanostructures on large area of polymer surface for antibiofouling application. *Micro & Nano Letters*, *14*(2), 191-195. https://doi.org/10.1049/mnl.2018.5462.

[47] Liu, X., Li, K., Shen, J., & Gong, F. (2021). Hot embossing of moth eye-like nanostructure array on transparent glass with enhanced antireflection for solar cells. *Ceramics International*, *47*(13), 18367-18375. https://doi.org/10.1016/j.ceramint.2021.03.159.

[48] Zhang, C., Liang, F., Zhang, W., Liu, H., Ge, M., Zhang, Y., ... & Tang, Y. (2020). Constructing mechanochemical durable and self-healing superhydrophobic surfaces. *ACS omega*, *5*(2), 986-994. https://doi.org/ 10.1021/acsomega.9b03912.

[49] Deshmukh, S. S., & Goswami, A. (2022). Current innovations in roller embossing—A comprehensive review. *Microsystem Technologies*, *28*(5), 1077-1114. https://doi.org/ 10.1007/s00542-022-05265-0.

[50] da Silva, Í. G., Lucas, E. F., & Advincula, R. (2021). Highly efficient oil/water and brine separations: superhydrophobic hybrid isobornyl methacrylate coatings. *Separation and Purification Technology*, *278*, 119365. https://doi.org/10.1016/

[51] Barbero, D. R., Saifullah, M. S., Hoffmann, P., Mathieu, H. J., Anderson, D., Jones, G. A., ... & Steiner, U. (2007). High-resolution nanoimprinting with a robust and reusable polymer mold. *Advanced Functional Materials*, *17*(14), 2419-2425. https://doi.org/10.1002/adfm.200600710.

[52] Kodihalli Shivaprakash, N., Zhang, J., Nahum, T., Barry, C., Truong, Q., & Mead, J. (2019). Roll-to-roll hot embossing of high aspect ratio micro pillars for superhydrophobic applications. *International Polymer Processing*, *34*(5), 502-512. https://doi.org/10.3139/217.3815

[53] Sun, J., Li, H., Huang, Y., Zheng, X., Liu, Y., Zhuang, J., & Wu, D. (2019). Simple and affordable way to achieve polymeric superhydrophobic surfaces with biomimetic hierarchical roughness. *ACS omega*, *4*(2), 2750-2757. https:// doi.org/10.1021/acsomega.8b03138.

[54] Roslizar, A., Dottermusch, S., Vüllers, F., Kavalenka, M. N., Guttmann, M., Schneider, M., ... & Klampaftis, E. (2019). Self-cleaning performance of superhydrophobic hot-embossed fluoropolymer films for photovoltaic modules. *Solar Energy Materials and Solar Cells*, *189*, 188-196. https://doi.org/10.1016/j.solmat.2018.09.017.

[55] Li, Y., Gao, H., Ma, Y., & Chen, D. (2020). Facile fabrication of biomimetic water pinning microstructures on polyethylene surfaces with robust

superhydrophobic wetting state. *Journal of Bionic Engineering*, *17*(4), 644-651. https://doi.org/10.1007/ s42235-020-0052-1.

[56] Sun, Q., Yang, Z., Hu, C., Li, C., Yan, G., & Wang, Z. (2020). Facile preparation of superhydrophobic PVDF microporous membranes with excellent anti-fouling ability for vacuum membrane distillation. *Journal of Membrane Science*, *605*, 118106. https://doi.org/10.1016/j.memsci.2020.118106.

[57] Sun, Q., Yang, Z., Wang, Z., & Wu, L. (2022). Anti-fouling performance investigation of micron-submicron hierarchical structure PVDF membranes in water-in-oil emulsion separation. *Journal of Environmental Chemical Engineering*, *10*(3), 107497. https:// doi.org/10.1016/j.jece.2022.107497.

[58] Kalimuldina, G., Turdakyn, N., Abay, I., Medeubayev, A., Nurpeissova, A., Adair, D., & Bakenov, Z. (2020). A review of piezoelectric PVDF film by electrospinning and its applications. *Sensors*, *20*(18), 5214. https://doi.org/10.3390/ s20185214.

[59] Liu, X., Mo, R., Li, K., Shen, J., Ma, J., & Gong, F. (2021). Manufacturing of 3D microlens array mold on bulk metallic glass by self-aligned multi-ball hot embossing. *International Journal of Precision Engineering and Manufacturing-Green Technology*, *8*, 1209-1223. https:// doi.org/10.1007/s40684-020-00266-8.

[60] Shen, J., Liang, J., Lin, X., Lin, H., Yu, J., & Yang, Z. (2020). Recent progress in polymer-based building materials. *International Journal of Polymer Science*, *2020*(1), 8838160. https://doi.org/10.1155/ 2020/8838160.

[61] Palacios-Cuesta, M., Vasiev, I., Gadegaard, N., Rodriguez-Hernandez, J., & García, O. (2014). Direct micrometer patterning and functionalization of polymer blend surfaces by using hot embossing. *European polymer journal*, *59*, 333-340. https://doi.org/10.1016/j.eurpolymj.2014.07.020

[62] Moon, I. Y., Kim, B. H., Lee, H. W., Oh, Y. S., Kim, J. H., & Kang, S. H. (2020). Superhydrophobic polymer surface with hierarchical patterns fabricated in hot imprinting process. *International Journal of Precision Engineering and Manufacturing-Green Technology*, *7*, 493-503. https://doi.org/10.1007/s40684-019-00094-5.

[63] Toosi, S. F., Moradi, S., Ebrahimi, M., & Hatzikiriakos, S. G. (2016). Microfabrication of polymeric surfaces with extreme wettability using hot embossing. *Applied surface science*, *378*, 426-434. https://doi.org/10.1016/j.apsusc.2016.03.116.

[64] Gong, D., Long, J., Fan, P., Jiang, D., Zhang, H., & Zhong, M. (2015). Thermal stability of micro–nano structures and superhydrophobicity of polytetrafluoroethylene films formed by hot embossing via a picosecond laser ablated template. *Applied Surface Science*, *331*, 437-443. https://doi.org/10.1016/j.apsusc.2015.01.102.

[65] Chen, Y., Gao, X. R., Huang, H. D., Xu, L., Ji, X., Zhong, G. J., ... & Li, Z. M. (2021). Superhydrophobic, self-cleaning, and robust properties of oriented polylactide imparted by surface structuring. *ACS Sustainable Chemistry & Engineering*, *9*(18), 6296-6304. https://doi.org/10.1021/acssuschemeng.1c00026.

[66] Gore, P. M., & Kandasubramanian, B. (2018). Heterogeneous wettable cotton based superhydrophobic Janus biofabric engineered with PLA/functionalized-organoclay microfibers for efficient oil–water separation. *Journal of Materials Chemistry A*, *6*(17), 7457-7479. https://doi.org/10.1039/c7ta11260b.

[67] Casalini, T., Rossi, F., Castrovinci, A., & Perale, G. (2019). A perspective on polylactic acid-based polymers use for nanoparticles synthesis and

applications. *Frontiers in bioengineering and biotechnology*, *7*, 259. https://doi.org/10.3389/

[68] Lee, S. E., Lim, H. G., Lee, S. S., Choi, D. G., Lee, D., & Hong, S. U. (2013). Embossed superhydrophobic polymer surfaces with topological variances. *Macromolecular Research*, *21*, 916-920. https://doi.org/10.1007/s13233-013-1107-5.

[69] Li, K., Hernandez-Castro, J. A., Turcotte, K., Morton, K., & Veres, T. (2020, July). Superhydrophobic thermoplastic surfaces with hierarchical micro-nanostructures fabricated by hot-embossing. In *2020 IEEE 20th International Conference on Nanotechnology (IEEE-Nano)* (pp. 81-84). IEEE. https://doi.org/10.1109/NANO47656.2020.9183514.

[70] Hooda, A., Goyat, M. S., Gupta, R., Prateek, M., Agrawal, M., & Biswas, A. (2017). Synthesis of nano-textured polystyrene/ZnO coatings with excellent transparency and superhydrophobicity. *Materials Chemistry and Physics*, *193*, 447-452. https://doi.org/ 10.1016/j.matchemphys.2017.03.011.

[71] Zhang, D., Qian, H., Wang, L., & Li, X. (2016). Comparison of barrier properties for a superhydrophobic epoxy coating under different simulated corrosion environments. *Corrosion science*, *103*, 230-241. https://doi.org/10.1016/j.corsci.2015.11.023.

[72] Zhang, M., Sun, J., Wang, Y., Yu, M., Liu, F., Ding, G., ... & Liu, L. (2021). Preparation of stable and durable superhydrophobic surface on Zr-based bulk metallic glass. *Colloids and Surfaces A: Physicochemical and Engineering Aspects*, *631*, 127654. https:// doi.org/10.1016/j.colsurfa.2021.127654.

[73] Gong, X., & He, S. (2020). Highly durable superhydrophobic polydimethylsiloxane/silica nanocomposite surfaces with good self-cleaning ability. *ACS omega*, *5*(8), 4100-4108. https://doi.org/10.1021/acsomega.9b03775.

[74] Wang, Z., Li, Y., Huan, D., Xiao, J., & Li, Y. (2021). The fabrication of superhydrophobic GF/PEEK composites with integrated structure and function by prepreg modifying and hot-pressing process. *Polymer-Plastics Technology and Materials*, *60*(12), 1357-1367. https://doi.org/10.1080/25740881.2021.1904981.

[75] Zhou, M., Xiong, X., Jiang, B., & Weng, C. (2018). Fabrication of high aspect ratio nanopillars and micro/nano combined structures with hydrophobic surface characteristics by injection molding. *Applied Surface Science*, *427*, 854-860. https://doi.org/10.1016/j.apsusc.2017.08.003.

[76] Jucius, D., Grigaliūnas, V., Mikolajūnas, M., Guobienė, A., Kopustinskas, V., Gudonytė, A., & Narmontas, P. (2011). Hot embossing of PTFE: Towards superhydrophobic surfaces. *Applied Surface Science*, *257*(6), 2353-2360. https:// doi.org/10.1016/j.apsusc.2010.09.102.

[77] Wu, B., Peng, C., Li, W., Yuan, Z., & Sheng, L. (2016, November). Chopped carbon fiber reinforced CeO2/PMMA/PVDF superhydrophobic composite coating with enhanced abrasion durability. In *2016 International Conference on Innovative Material Science and Technology (IMST 2016)* (pp. 1-9). Atlantis Press. https://doi.org/10.2991/imst-16.2016.1.

[78] Yuan, R., Wu, S., Yu, P., Wang, B., Mu, L., Zhang, X., ... & Zhu, J. (2016). Superamphiphobic and electroactive nanocomposite toward self-cleaning, antiwear, and anticorrosion coatings. *ACS applied materials & interfaces*, *8*(19), 12481-12493. https://doi.org/10.1021/acsami.6b03961.

[79] Wang, X., Liu, Y., Cheng, H., & Ouyang, X. (2022). Surface wettability for skin-interfaced sensors and devices. *Advanced functional materials*, *32*(27), 2200260. https://doi.org/10.1002/adfm.202200260.

[80] Barz, J., & Umlauf, G. (2022). Roll-to-roll structuring and PECVD coating of polymer foils: Enhancement of hydrophobicity for various

applications. *Vakuum in Forschung und Praxis*, *34*(4), 31-35. https://doi.org/10.1002/ vipr.202200787.

[81] Zhang, L., Tan, Z., Zhang, C., Tang, J., Yao, C., You, X., & Hao, B. (2022). Research on metal corrosion resistant bioinspired special wetting surface based on laser texturing technology: A Review. *Micromachines*, *13*(9), 1431. https:// doi.org/10.3390/mi13091431.

[82] Peng, L., Deng, Y., Yi, P., & Lai, X. (2013). Micro hot embossing of thermoplastic polymers: a review. *Journal of Micromechanics and Microengineering*, *24*(1), 013001. https://doi.org/10.1088/ 0960-1317/24/1/013001.

[83] Maghsoudi, K., Vazirinasab, E., Momen, G., & Jafari, R. (2020). Advances in the fabrication of superhydrophobic polymeric surfaces by polymer molding processes. *Industrial & Engineering Chemistry Research*, *59*(20), 9343-9363. https://doi.org/10.1021/acs.iecr.0c00508.

[84] Deshmukh, S. S., & Goswami, A. (2020). Hot Embossing of polymers–A review. *Materials Today: Proceedings*, *26*, 405-414. https://doi.org/10.1016/j.matpr.2019.12.067

[85] Oopath, S. V., Baji, A., & Abtahi, M. (2022). Biomimetic Rose Petal Structures Obtained Using UV-Nanoimprint Lithography. Polymers 2022, 14, 3303. https:// doi.org/10.3390/polym14163303.

[86] Zuo, Z., Liao, R., Zhao, X., Song, X., Qiao, Z., Guo, C., ... & Yuan, Y. (2017). Anti-frosting performance of superhydrophobic surface with ZnO nanorods. *Applied Thermal Engineering*, *110*, 39-48. https://doi.org/10.1016/j.applthermaleng.2016.08.145.

[87] Zhang, Q., Jin, B., Wang, B., Fu, Y., Zhan, X., & Chen, F. (2017). Fabrication of a highly stable superhydrophobic surface with dual-scale

structure and its antifrosting properties. *Industrial & Engineering Chemistry Research*, *56*(10), 2754-2763. https://doi.org/10.1021/acs.iecr.6b04650.

[88] Zhang, P., & Lv, F. Y. (2015). A review of the recent advances in superhydrophobic surfaces and the emerging energy-related applications. *Energy*, *82*, 1068-1087. https://doi.org/10.1016/j.energy.2015.01.061.

[89] Wen, G., Guo, Z., & Liu, W. (2017). Biomimetic polymeric superhydrophobic surfaces and nanostructures: from fabrication to applications. *Nanoscale*, *9*(10), 3338-3366. https://doi.org/10.1039/C7NR00096K.

[90] Li, J., Wei, Y., Huang, Z., Wang, F., Yan, X., & Wu, Z. (2017). Electrohydrodynamic behavior of water droplets on a horizontal super hydrophobic surface and its self-cleaning application. *Applied Surface Science*, *403*, 133-140. https://doi.org/10.1016/j.apsusc.2017.01.141.

[91] Zhi, J. H., Zhang, L. Z., Yan, Y., & Zhu, J. (2017). Mechanical durability of superhydrophobic surfaces: The role of surface modification technologies. *Applied Surface Science*, *392*, 286-296. https://doi.org/10.1016/j.apsusc.2016.09.049.

[92] Wang, H., Dong, S., & Wang, Z. (2018). One-step fabrication of superhydrophobic surface on beryllium copper alloys and corrosion protection application. *Colloids and Surfaces A: Physicochemical and Engineering Aspects*, *556*, 291-298. https://doi.org/10.1016/j.colsurfa.2018.08.044.

[93] Vazirinasab, E., Jafari, R., & Momen, G. (2018). Application of superhydrophobic coatings as a corrosion barrier: A review. *Surface and Coatings Technology*, *341*, 40-56. https://doi.org/10.1016/j.surfcoat.2017.11.053.

[94] Wang, G., Liu, S., Wei, S., Liu, Y., Lian, J., & Jiang, Q. (2016). Robust superhydrophobic surface on Al substrate with durability, corrosion resistance and ice-phobicity. *Scientific reports*, *6*(1), 20933. https://doi.org/10.1038/srep20933.

[95] Tong, W., Xiong, D., Wang, N., Yan, C., & Tian, T. (2018). Green and timesaving fabrication of a superhydrophobic surface and its application to anti-icing, self-cleaning and oil-water separation. *Surface and Coatings Technology*, *352*, 609-618. https://doi.org/10.1016/j.surfcoat.2018.08.035.

[96] Fang, G., & Amirfazli, A. (2014). Understanding the anti-icing behavior of superhydrophobic surfaces. *Surface Innovations*, *2*(2), 94-102. https://doi.org/10.1680/ si.13.00046.

[97] Baiyi, C., Jianhui, Q., Eiichi, S., Nobuhiro, K., Ruilu, L., & Huixia, F. (2016). Robust and Superhydrophobic Surface Modification by a "Paint+ Adhesive" Method: Applications in Self-Cleaning after Oil Contamination and Oil–Water Separation. https://doi.org/10.1021/acsami.6b04108.

[98] Si, Y., & Guo, Z. (2015). Superhydrophobic nanocoatings: from materials to fabrications and to applications. *Nanoscale*, *7*(14), 5922-5946. https://doi.org/10.1039/c4nr07554d.

[99] Saji, V. S. (2021). Carbon nanostructure-based superhydrophobic surfaces and coatings. *Nanotechnology Reviews*, *10*(1), 518-571. https://doi.org/10.1515/ntrev 2021-0039.

[100] Rastegari, A., & Akhavan, R. (2015). On the mechanism of turbulent drag reduction with super-hydrophobic surfaces. *Journal of Fluid Mechanics*, *773*, R4. https:// doi.org/10.1017/jfm.2015.266.

[101] Li, Z., Marlena, J., Pranantyo, D., Nguyen, B. L., & Yap, C. H. (2019). A porous superhydrophobic surface with active air plastron control for drag

reduction and fluid impalement resistance. *Journal of Materials Chemistry A*, *7*(27), 16387-16396. https://doi.org/10.1039/c9ta02745a.

[102] Du, P., Wen, J., Zhang, Z., Song, D., Ouahsine, A., & Hu, H. (2017). Maintenance of air layer and drag reduction on superhydrophobic surface. *Ocean Engineering*, *130*, 328-335. https://doi.org/10.1016/j.oceaneng.2016.11.028.

[103] Das, S., Kumar, S., Samal, S. K., Mohanty, S., & Nayak, S. K. (2018). A review on superhydrophobic polymer nanocoatings: recent development and applications. *Industrial & Engineering Chemistry Research*, *57*(8), 2727-2745. https://doi.org/10.1021/acs.iecr.7b04887.

[104] Varshney, P., Lomga, J., Gupta, P. K., Mohapatra, S. S., & Kumar, A. (2018). Durable and regenerable superhydrophobic coatings for aluminium surfaces with excellent self-cleaning and anti-fogging properties. *Tribology International*, *119*, 38-44. https://doi.org/10.1016/j.triboint.2017.10.033.

[105] Wang, L., Lu, J., Wang, M., Zhang, B., Hou, Y., Liu, G., ... & Liu, J. (2019). Anti-fogging performances of liquid metal surface modified by ZnO nano-petals. *Journal of the Taiwan Institute of Chemical Engineers*, *95*, 65-70. https://doi.org/10.1016/j.jtice.2018.09.039.

[106] Falde, E. J., Yohe, S. T., Colson, Y. L., & Grinstaff, M. W. (2016). Superhydrophobic materials for biomedical applications. *Biomaterials*, *104*, 87-103. https://doi.org/ 10.1016/j.biomaterials.2016.06.050.

[107] Lima, A. C., & Mano, J. F. (2015). Micro/nano-structured superhydrophobic surfaces in the biomedical field: part II: applications overview. *Nanomedicine*, *10*(2), 271-297. https://doi.org/10.2217/nnm.14.175

[108] Chenab, K. K., Sohrabi, B., & Rahmanzadeh, A. (2019). Superhydrophobicity: advanced biological and biomedical

applications. *Biomaterials science*, *7*(8), 3110-3137. https://doi.org/10.1039/c9bm00558g.

[109] Liu, M., Hou, Y., Li, J., Tie, L., Peng, Y., & Guo, Z. (2017). Inorganic adhesives for robust, self-healing, superhydrophobic surfaces. *Journal of Materials Chemistry A*, *5*(36), 19297-19305. https://doi.org/10.1039/c7ta06001g.

[110] Vüllers, F., Gomard, G., Preinfalk, J. B., Klampaftis, E., Worgull, M., Richards, B., ... & Kavalenka, M. N. (2016). Bioinspired superhydrophobic highly transmissive films for optical applications. *Small*, *12*(44), 6144-6152. https://doi.org/ 10.1002/smll.201601443.

[111] Patil, D., Sharma, A., Aravindan, S., & Rao, P. V. (2019). Development of hot embossing setup and fabrication of ordered nanostructures on large area of polymer surface for antibiofouling application. *Micro & Nano Letters*, *14*(2), 191-195. https://doi.org/ 10.1049/mnl.2018.5462.

[112] Chandralekha, N. R., Shanthi, J., Cathelene Antonette, L., & Anoop, K. K. (2024). Improved Efficiency of Solar Cell using Silane based SnO2 Thin Films with Self-Cleaning and Antifogging Properties. *Silicon*, *16*(12), 5121-5134. https://doi.org/10.3390/coatings11050493.

[113] Li, J., Xu, J., Lian, Z., Yu, Z., & Yu, H. (2020). Fabrication of antireflection surfaces with superhydrophobic property for titanium alloy by nanosecond laser irradiation. *Optics & Laser Technology*, *126*, 106129. https://doi.org/10.1016/j.optlastec.2020.106129.

[114] Qiu, H., Feng, K., Gapeeva, A., Meurisch, K., Kaps, S., Li, X., ... & Baum, M. (2022). Functional polymer materials for modern marine biofouling control. *Progress in Polymer Science*, *127*, 101516. https://doi.org/ 10.1016/j.progpolymsci.2022.101516.

[115] Jafari, R., Cloutier, C., Allahdini, A., & Momen, G. (2019). Recent progress and challenges with 3D printing of patterned hydrophobic and superhydrophobic surfaces. *The International Journal of Advanced Manufacturing Technology*, *103*, 1225-1238. https://doi.org/10.1007/ s00170-019-036304.

[116] Cherupurakal, N., Mozumder, M. S., Mourad, A. H. I., & Lalwani, S. (2021). Recent advances in superhydrophobic polymers for antireflective self-cleaning solar panels. *Renewable and Sustainable Energy Reviews*, *151*, 111538. https://doi.org/10.1016/j.rser.2021.111538.

[117] Oliveira, R. D., Mouquinho, A., Centeno, P., Alexandre, M., Haque, S., Martins, R., ... & Mendes, M. J. (2021). Colloidal lithography for photovoltaics: An attractive route for light management. *Nanomaterials*, *11*(7), 1665. https:// doi.org/10.3390/nano11071665.

[118] Bayer, I. S. (2017). On the durability and wear resistance of transparent superhydrophobic coatings. *Coatings*, *7*(1), 12. https://doi.org/10.3390/ coatings7010012.

[119] Nguyen-Tri, P., Tran, H. N., Plamondon, C. O., Tuduri, L., Vo, D. V. N., Nanda, S., ... & Bajpai, A. K. (2019). Recent progress in the preparation, properties and applications of superhydrophobic nano-based coatings and surfaces: A review. *Progress in organic coatings*, *132*, 235-256. https://doi.org/ 10.1016/j.porgcoat.2019.03.042.

[120] Chen, K., Zhou, S., & Wu, L. (2014). Facile fabrication of self-repairing superhydrophobic coatings. *Chemical Communications*, *50*(80), 11891-11894.

https://doi.org/10.1039/C3CC49251F

[121] Sharma, J., Bhandari, A., Khatri, N., Jangra, S., Goyat, M. S., & Mishra, Y. K. (2024). A brief review of transitional wetting regimes for superhydrophobic surfaces. *Journal of the Brazilian Society of Mechanical*

Sciences and Engineering, *46*(5), 273. https://doi.org/10.1007/s40430-024-04844-8

[122] Jaishree, S., Bhandari, A., Khatri, N., Singh, B., Jangra, S., Husain, A., ... & Goyat, M. S. (2024). Advancement of Analytical Model for Hydrophobic Rectangular Pillared Array on Al-Surface and Its Experimental Validation. *International Journal of Precision Engineering and Manufacturing*, *25*(5), 947-958. https://doi.org/10.1007/s12541-024-00969-x

[123] Sharma, J., Bhandari, A., Jangra, S., & Goyat, M. S. (2024). Sol–gel derived highly hydrophobic Polystyrene/SiO2 spray coatings on polished stainless steel and textured aluminium substrates. *Transactions of the IMF*, *102*(2), 77-82. https://doi.org/10.1080/00202967.2024.2315777.

[124] Park, S., Kim, J., & Park, C. H. (2015). Superhydrophobic textiles: review of theoretical definitions, fabrication and functional evaluation. *Journal of Engineered Fibers and Fabrics*, *10*(4), 155892501501000401. https://doi.org/10.1177/155892501501000401

[125] Wang, Z., Shen, Y., Tao, J., Liu, S., Jiang, J., Xu, Y., ... & Li, H. (2023). An integrated superhydrophobic anti/de-icing film heater with low energy consumption: Interpenetration behavior of components based on wet-film spraying method. *Applied Thermal Engineering*, *223*, 120028. https://doi.org/10.1016/j. applthermaleng.2023.120028

[126] Maghsoudi, K., Vazirinasab, E., Momen, G., & Jafari, R. (2020). Advances in the fabrication of superhydrophobic polymeric surfaces by polymer molding processes. *Industrial & Engineering Chemistry Research*, *59*(20), 9343-9363. https://doi.org/10.1021/acs.iecr.0c00508

[127] Bhandari, A., Khatri, N., Mishra, Y. K., & Goyat, M. S. (2023). Superhydrophobic coatings by the hot embossing approach: recent

developments and state-of-art applications. *Materials Today Chemistry*, *30*, 101553. https://doi. org/10.1016/j.mtchem.2023.101553

[128] Roslizar, A., Dottermusch, S., Vüllers, F., Kavalenka, M. N., Guttmann, M., Schneider, M., ... & Klampaftis, E. (2019). Self-cleaning performance of superhydrophobic hot-embossed fluoropolymer films for photovoltaic modules. *Solar Energy Materials and Solar Cells*, *189*, 188-196. https://doi.org/10.1016/j.solmat.2018.09.017

[129] Zi, Y., Ding, J., Song, J., Humphreys, G., Peng, Y., Li, C., ... & Guo, W. (2018). Grain yield, starch content and activities of key enzymes of waxy and non-waxy wheat (Triticum aestivum L.). *Scientific reports*, *8*(1), 4548. https://doi. org/ 10. 1038/ s41598-018-30057-w

[130] He, S., Zhu, Z., Zhang, B., & Tian, Y. (2023). Wetting thresholds for long-lasting superwettability: from intrinsic wetting boundary to critical roughness value. *Chemical Engineering Journal*, *454*, 140058. https:// doi.org/10.1016/j.cej.2022.140058

[131] Liu, Y., Du, Y., Fei, G., Zhou, T., & Zhao, C. (2023). Effects of surface wettability on bubble departure and critical heat flux: A parametric study based on 3-D dynamic force analysis model. *International Journal of Thermal Sciences*, *186*, 108149. https://doi.org/ 10. 1016/j.ijthermals ci. 2023. 108149

[132] Raj, R., Enright, R., Zhu, Y., Adera, S., & Wang, E. N. (2012). Unified model for contact angle hysteresis on heterogeneous and superhydrophobic surfaces. *Langmuir*, *28*(45), 15777-15788. https://doi. org/ 10. 1021/ la303070s

[133] Shahraz, A., Borhan, A., & Fichthorn, K. A. (2012). A theory for the morphological dependence of wetting on a physically patterned solid surface. *Langmuir*, *28*(40), 14227-14237. https:// doi. org/ 10. 1021/ la302 6304

[134] Bai, Y., Zhang, H., Shao, Y., Zhang, H., & Zhu, J. (2021). Recent progresses of superhydrophobic coatings in different application fields: An overview. *Coatings*, *11*(2), 116. https://doi.org/10.3390/coatings11020116

[135] Li, Y., Gao, H., Ma, Y., & Chen, D. (2020). Erratum to: Facile Fabrication of Biomimetic Water Pinning Microstructures on Polyethylene Surfaces with Robust Superhydrophobic Wetting State. *Journal of Bionic Engineering*, *17*, 1084-1084. https://doi.org/10.1007/s42235-020-0052-1

[136] Yang, Z., Zhu, C., Zheng, N., Le, D., & Zhou, J. (2018). Superhydrophobic surface preparation and wettability transition of titanium alloy with micro/nano hierarchical texture. *Materials*, *11*(11), 2210. https://doi.org/10.3390/ma11112210

[137] A. Jawad, Q., S. Zinad, D., Dawood Salim, R., A Al-Amiery, A., Sumer Gaaz, T., Takriff, M. S., & H. Kadhum, A. A. (2019). Synthesis, characterization, and corrosion inhibition potential of novel thiosemicarbazone on mild steel in sulfuric acid environment. *Coatings*, *9*(11), 729. https:// doi.org/ 10. 3390/ coati ngs9060362

[138] Jiang, G., Hu, J., & Chen, L. (2020). Preparation of a flexible superhydrophobic surface and its wetting mechanism based on fractal theory. *Langmuir*, *36*(29), 8435-8443. https:// doi. org/ 10. 1021/ acs.langmuir.0c00823

[139] Fei, L., He, Z., LaCoste, J. D., Nguyen, T. H., & Sun, Y. (2020). A mini review on superhydrophobic and transparent surfaces. *The Chemical Record*, *20*(11), 1257-1268. https://doi.org/10.1002/tcr.202000075

[140] Yang, J., Wang, R., Long, F., Zhang, X., Liu, J., Hu, W., & Liu, L. (2021). New perspectives on structural parameters and hydrophobic model inspired by a superhydrophobic Cu cone-flower coating. *Materials & Design*, *206*, 109827. https:// doi.org/10.1016/j.matdes.2021.109827

[141] Hao, S., Xie, Z., Yang, W., Zhang, L., Wang, W., Kou, J., ... & Fan, J. (2023). Wetting-State-Induced turning of water droplet moving direction on the surface. *ACS nano*, *17*(3), 2182-2189. https://doi.org/10.1021/acsnano.2c08383

[142] Cai, Y., Chang, W., Luo, X., Sousa, A. M., Lau, K. H. A., & Qin, Y. (2018). Superhydrophobic structures on 316L stainless steel surfaces machined by nanosecond pulsed laser. *Precision Engineering*, *52*, 266-275. https:// doi. org/ 10. 1016/j. precisione ng.2018.01.004

[143] Li, X. M., Reinhoudt, D., & Crego-Calama, M. (2007). What do we need for a superhydrophobic surface? A review on the recent progress in the preparation of superhydrophobic surfaces. *Chemical Society Reviews*, *36*(8), 1350-1368. https://doi.org/10.1039/b602486f

[144] Jiaqiang, E., Jin, Y., Deng, Y., Zuo, W., Zhao, X., Han, D., ... & Zhang, Z. (2018). Wetting models and working mechanisms of typical surfaces existing in nature and their application on superhydrophobic surfaces: a review. *Adv. Mater. Interfaces*, *5*, 1701052. https://doi.org/10.1002/admi.201701052

[145] Evans, R., Stewart, M. C., & Wilding, N. B. (2019). A unified description of hydrophilic and superhydrophobic surfaces in terms of the wetting and drying transitions of liquids. *Proceedings of the National Academy of Sciences*, *116*(48), 23901-23908. https://doi.org/10.1073/pnas.1913587116

[146] Yong, H., Li, Z., Huang, X., Wang, K., Zhou, Y. N., Li, Q., ... & Zhou, D. (2022). Superhydrophobic materials: Versatility and translational applications. *Advanced Materials Interfaces*, *9*(30), 2200435. https://doi.org/10.1002/admi.202200435

[147] Peng, J., Wu, L., Zhang, H., Wang, B., Si, Y., Jin, S., & Zhu, H. (2022). Research progress on eco-friendly superhydrophobic materials in environment, energy and biology. *Chemical Communications*, *58*(80), 11201-11219. https:// doi. org/ 10. 1039/d2cc03899d

[148] Yilgör, E., Söz, C. K., & Yilgör, I. (2018). Wetting behavior of superhydrophobic poly (methyl methacrylate). *Progress in Organic Coatings*, *125*, 530-536. https://doi.org/10.1016/j.porgcoat.2018.07.018

[149] Grewal, H. S., Cho, I. J., Oh, J. E., & Yoon, E. S. (2014). Effect of topography on the wetting of nanoscale patterns: experimental and modeling studies. *Nanoscale*, *6*(24), 15321-15332. https://doi.org/10.1039/C4NR04069D

[150] Konar, M., Roy, B., & Govindaraju, T. (2020). Molecular architectonics-guided fabrication of superhydrophobic and self-cleaning materials. *Advanced Materials Interfaces*, *7*(11), 2000246. https://doi.org/10.1002/admi.202000246

[151] Behera, S. K., Kumar P, A., Dogra, N., Nosonovsky, M., & Rohatgi, P. (2019). Effect of microstructure on contact angle and corrosion of ductile iron: Iron–graphite composite. *Langmuir*, *35*(49), 16120-16129. https://doi. org/ 10. 1021/acs.langmuir.9b02395

[152] Majhy, B., Singh, V. P., & Sen, A. K. (2020). Understanding wetting dynamics and stability of aqueous droplet over superhydrophilic spot surrounded by superhydrophobic surface. *Journal of colloid and interface science*, *565*, 582-591. https://doi.org/10.1016/j.jcis.2020.01.056

[153] Starinskiy, S. V., Bulgakov, A. V., Gatapova, E. Y., Shukhov, Y. G., Sulyaeva, V. S., Timoshenko, N. I., & Safonov, A. I. (2018). Transition from superhydrophilic to superhydrophobic of silicon wafer by a combination of laser treatment and fluoropolymer deposition. *Journal of Physics D: Applied Physics*, *51*(25), 255307. https://doi.org/10.1088/1361-6463/ aac641

[154] Cheng, K., Naccarato, B., Kim, K. J., & Kumar, A. (2016). Theoretical consideration of contact angle hysteresis using surface-energy-minimization methods. *International Journal of Heat and Mass Transfer*, *102*, 154-161. https://doi.org/10.1016/j.ijheatmasstransfer.2016.06.014

[155] Sudeepthi, A., Yeo, L., & Sen, A. K. (2020). Cassie–Wenzel wetting transition on nanostructured superhydrophobic surfaces induced by surface acoustic waves. *Applied Physics Letters*, *116*(9). https://doi.org/10.1063/1.5145282

[156] Marmur, A., & Kojevnikova, S. (2020). Super-hydrophobic surfaces: Methodological considerations for physical design. *Journal of colloid and interface science*, *568*, 148-154. https:// doi. org/ 10. 1016/j. jcis. 2020. 02.040

[157] Tenjimbayashi, M., Samitsu, S., & Naito, M. (2019). Simultaneous detection and repair of wetting defects in superhydrophobic coatings via Cassie–Wenzel transitions of liquid marbles. *Advanced Functional Materials*, *29*(26), 1900688. https://doi.org/10.1002/adfm.201900688

[158] Li, H., Yan, T., Fichthorn, K. A., & Yu, S. (2018). Dynamic contact angles and mechanisms of motion of water droplets moving on nanopillared superhydrophobic surfaces: a molecular dynamics simulation study. *Langmuir*, *34*(34), 9917-9926. https://doi.org/10.1021/acs.langmuir.8b01324

[159] Wu, Q., Gao, A., Tao, F., & Yang, P. (2018). Understanding Biomolecular Crystallization on Amyloid-Like Superhydrophobic Biointerface. *Advanced Materials Interfaces*, *5*(6), 1701065. https:// doi.org/10.1002/admi.201701065

[160] Roy, R., Weibel, J. A., & Garimella, S. V. (2018). Re-entrant cavities enhance resilience to the Cassie-to-Wenzel state transition on superhydrophobic surfaces during electrowetting. *Langmuir*, *34*(43), 12787-12793. https://doi.org/10.1021/acs.langmuir.8b02675

[161] Zhang, B. X., Cai, Z. H., Ding, Q., Zhu, K. Q., Yang, Y. R., & Wang, X. D. (2023). Bouncing dynamics of nanodroplets impacting superhydrophobic surfaces: The coupling influence of wetting transitions and scale

effects. *Colloids and Surfaces A: Physicochemical and Engineering Aspects*, *657*, 130579. https:// doi. org/ 10. 1016/j.colsurfa.2022.130579

[162] Style, R. W., & Dufresne, E. R. (2012). Static wetting on deformable substrates, from liquids to soft solids. *Soft Matter*, *8*(27), 7177-7184. https://doi.org/10.1039/c2sm25540e

[163] Hensel, R., Helbig, R., Aland, S., Braun, H. G., Voigt, A., Neinhuis, C., & Werner, C. (2013). Wetting resistance at its topographical limit: the benefit of mushroom and serif T structures. *Langmuir*, *29*(4), 1100-1112. https:// doi. org/ 10. 1021/ la304 179b

[164] Borgaonkar, A. V., & Syed, I. (2020). Effect of coatings on rolling contact fatigue and tribological parameters of rolling/sliding contacts under dry/lubricated conditions: a review. *Sādhanā*, *45*, 1-16. https://doi.org/10.1007/s12046-020-1266-y

[165] V. Borgaonkar, A., & Syed, I. (2022). Effect of coating material properties on the lubrication performance of rolling contacts under TEHL regime. *Australian Journal of Mechanical Engineering*, *20*(2), 352-359. https://doi.org/10. 1080/14484846.2019.1710018

[166] Bange, P. G., & Bhardwaj, R. (2016). Computational study of bouncing and non-bouncing droplets impacting on superhydrophobic surfaces. *Theoretical and Computational Fluid Dynamics*, *30*, 211-235. https:// doi. org/ 10.1007/s00162-015-0376-3

[167] Wang, H., Lu, H., & Zhao, W. (2023). A review of droplet bouncing behaviors on superhydrophobic surfaces: Theory, methods, and applications. *Physics of Fluids*, *35*(2). https://doi.org/10.1063/5.0136692

[168] Cheng, C. T., Zhang, G., & To, S. (2016). Wetting characteristics of bare micro-patterned cyclic olefin copolymer surfaces fabricated by ultra-precision

raster milling. *RSC advances*, *6*(2), 1562-1570. https://doi.org/10.1039/c5ra20809b

[169] Dwivedi, S., Dixit, A. R., Das, A. K., & Nag, A. (2023). A novel additive texturing of stainless steel 316L through binder jetting additive manufacturing. *International Journal of Precision Engineering and Manufacturing-Green Technology*, *10*(6), 1605-1613. https://doi.org/10.1007/s40684-023-00508-5

[170] Evans, R., Stewart, M. C., & Wilding, N. B. (2019). A unified description of hydrophilic and superhydrophobic surfaces in terms of the wetting and drying transitions of liquids. *Proceedings of the National Academy of Sciences*, *116*(48), 23901-23908. https://doi. org/ 10. 1073/pnas. 19135 87116

[171] Feng, J., Tuominen, M. T., & Rothstein, J. P. (2011). Hierarchical superhydrophobic surfaces fabricated by dual-scale electron-beam-lithography with well-ordered secondary nanostructures. *Advanced Functional Materials*, *21*(19), 3715-3722. https://doi. org/10.1002/adfm.201100665

[172] Jeon, Y., Nagappan, S., Li, X. H., Lee, J. H., Shi, L., Yuan, S., ... & Ha, C. S. (2021). Highly transparent, robust hydrophobic, and amphiphilic organic–inorganic hybrid coatings for antifogging and antibacterial applications. *ACS Applied Materials & Interfaces*, *13*(5), 6615-6630. https:// doi. org/ 10. 1021/ acsami. 0c20401

[173] Jerin, W. R., Park, S. J., & Moon, S. K. (2023). A design optimization framework for 3D printed lattice structures. *International Journal of Precision Engineering and Manufacturing-Smart Technology*, *1*(2), 145-156.

[174] Kang, Y., Jang, G., Kim, G. E., Kwon, S., Lee, M. G., & Jeon, Y. (2022). Design of high-durability superhydrophobic microsurface structures. *International Journal of Precision Engineering and Manufacturing*, *23*(8), 929-942. https://doi.org/10.1007/s12541-022-00661-y

[175] Kim, M. G., Kim, Y. M., & Han, S. Y. (2022). Mechanical reliability prediction of foldable displays using subcritical crack growth in siloxane-based cover window by two-point bending test. *International Journal of Precision Engineering and Manufacturing*, *23*(11), 1301-1313. https://doi.org/10.1007/s12541-022-00702-6

[176] Kim, T., Yun, T. H., Yim, C., & Kim, J. (2023). Fabrication of short circuit-preventing electrodes with a self-assembled monolayer on flashlight-sintered porous copper nanofilms. *International Journal of Precision Engineering and Manufacturing*, *24*(1), 43-52. https://doi.org/10.1007/s12541-022-00728-w

[177] Laghari, R. A., He, N., Jamil, M., Hussain, M. I., Gupta, M. K., & Krolczyk, G. M. (2023). A state-of-the-art review on recently developed sustainable and green cooling/lubrication technologies in machining metal matrix composites (MMCs). *International Journal of Precision Engineering and Manufacturing-Green Technology*, *10*(6), 1637-1660. https://doi.org/10.1007/s40684-023-00521-8

[178] Lee, J., Chua, P. C., Chen, L., Ng, P. H. N., Kim, Y., Wu, Q., ... & Moon, S. K. (2023). Key enabling technologies for smart factory in automotive industry: status and applications. *International Journal of Precision Engineering and Manufacturing-Smart Technology*, *1*(1), 93-105. https://doi.org/10.57062/ijpem-st.2022.0017

[179] Mittal, A., Verma, S., Iqbal, S. M., Gupta, R., Goyat, M. S., Kaur, K., & Nippani, S. K. (2018). A short review on challenges in fabrication of oil repellent surfaces. *IJRAR-International Journal of Research and Analytical Reviews (IJRAR)*, *5*(4), 862-866. http://www.ijrar.org/papers/IJRAR1944328

[180] Paven, M., Mammen, L., & Vollmer, D. (2016). Challenges and opportunities of superhydrophobic/superamphiphobic coatings in real applications. https://doi.org/10.1039/9781782622192-00209

[181] Rajiv, S., Kumaran, S., & Sathish, M. (2019). Long-term-durable anti-icing superhydrophobic composite coatings. *Journal of applied polymer science*, *136*(7), 47059. https:// doi. org/ 10. 1002/ app.47059

[182] Rodič, P., Kapun, B., & Milošev, I. (2022). Superhydrophobic aluminium surface to enhance corrosion resistance and obtain self-cleaning and anti-icing ability. *Molecules*, *27*(3), 1099. https:// doi. org/ 10.3390/molecules27031099

[183] Prasad, K. K., Roy, T., Goud, M. M., Karar, V., & Mishra, V. (2021). Diamond turned hierarchically textured surface for inducing water repellency: analytical model and experimental investigations. *International Journal of Mechanical Sciences*, *193*, 106140. https://doi.org/10.1016/j.ijmecsci.2020.106140

[184] Dharmadhikari, S., Nikam, M., Mastud, S., & Bulbule, N. (2024). Mathematical modeling of wettability of textured surface consisting cylindrical micro pillars. *International Journal on Interactive Design and Manufacturing (IJIDeM)*, 1-18. https://doi.org/10.1007/s12008-023-01645-6

[185] Li, Q., & Zanelli, A. (2021). A review on fabrication and applications of textile envelope integrated flexible photovoltaic systems. *Renewable and Sustainable Energy Reviews*, *139*, 110678. https://doi.org/10.1016/j.rser.2020.110678Get rights and content

[186] Cardoso, V. F., Correia, D. M., Ribeiro, C., Fernandes, M. M., & Lanceros-Méndez, S. (2018). Fluorinated polymers as smart materials for

advanced biomedical applications. *Polymers*, *10*(2), 161. https://doi.org/10.3390/polym10020161

[187] Shamshiri, M., Jafari, R., & Momen, G. (2021). Potential use of smart coatings for icephobic applications: A review. *Surface and Coatings Technology*, *424*, 127656. https://doi.org/10.1016/j.surfcoat.2021.127656

[188] Hu, J., Chen, W., Zhao, B., & Yang, D. (2017). Buildings with ETFE foils: A review on material properties, architectural performance and structural behavior. *Construction and Building Materials*, *131*, 411-422. https://doi.org/10.1016/j.conbuildmat.2016.11.062

[189] Yuan, Y., Yu, X., Yang, X., Xiao, Y., Xiang, B., & Wang, Y. (2017). Bionic building energy efficiency and bionic green architecture: A review. *Renewable and sustainable energy reviews*, *74*, 771-787. https://doi.org/10.1016/j.rser.2017.03.004

[190] Grygiel, P., Tarłowski, J., Prześniak-Welenc, M., Łapiński, M., Łubiński, J., Mielewczyk-Gryń, A., ... & Kwiatek, M. (2021). Prototype design and development of low-load-roof photovoltaic modules for applications in on-grid systems. *Solar Energy Materials and Solar Cells*, *233*, 111384. https://doi.org/10.1016/j.solmat.2021.111384

[191] Karasu, B., Oytaç, Z., Ergani, E., & Buluç, A. (2020). Solar glass panels: a review. *Avrupa Bilim ve Teknoloji Dergisi*, (20), 548-565. https://doi.org/10.31590/ejosat.746056

[192] Handrea-Dragan, M., & Botiz, I. (2021). Multifunctional structured platforms: from patterning of polymer-based films to their subsequent filling with various nanomaterials. *Polymers*, *13*(3), 445. https://doi.org/10.3390/polym13030445

[193] Cabezudo, N., Sun, J., Andi, B., Ding, F., Wang, D., Chang, W., ... & Xu, B. B. (2019). Enhancement of surface wettability via micro-and

nanostructures by single point diamond turning. *Nanotechnology and Precision Engineering*, *2*(1), 8-14. https://doi.org/10.1016/j.npe.2019.03.008

[194] Hatefi, S., & Abou-El-Hossein, K. (2022). Review of magnetic-assisted single-point diamond turning for ultra-high-precision optical component manufacturing. *The International Journal of Advanced Manufacturing Technology*, *120*(3), 1591-1607. https://doi.org/10.1007/s00170-022-08791-3

[195] Cheng, C. T., Zhang, G., & To, S. (2016). Wetting characteristics of bare micro-patterned cyclic olefin copolymer surfaces fabricated by ultra-precision raster milling. *RSC advances*, *6*(2), 1562-1570. https://doi.org/10.1039/C5RA20809B

[196] Dwivedi, S., Dixit, A. R., Das, A. K., & Nag, A. (2023). A novel additive texturing of stainless steel 316L through binder jetting additive manufacturing. *International Journal of Precision Engineering and Manufacturing-Green Technology*, *10*(6), 1605-1613. https://doi.org/10.1007/s40684-023-00508-5

[197] Chan, C. Y., Li, L. H., Lee, W. B., & Wong, H. C. (2016). Use of nano-droplet-enriched cutting fluid (NDCF) in ultra-precision machining. *The International Journal of Advanced Manufacturing Technology*, *84*, 2047-2054. https://doi.org/10.1007/s00170-015-7861-0

[198] Vrancken, N., Li, J., Sergeant, S., Vereecke, G., Doumen, G., Holsteyns, F., ... & Xu, X. (2018). In-situ ATR-FTIR for dynamic analysis of superhydrophobic breakdown on nanostructured silicon surfaces. *Scientific reports*, *8*(1), 11637. https://doi.org/10.1038/s41598-018-30057-w

[199] Satria, M., & Saleh, T. A. (2023). Synthesis of Superhydrophobic/Superoleophilic stearic acid and Polymer-modified magnetic polyurethane for Oil-Water Separation: Effect of polymeric

nature. *Journal of Colloid and Interface Science*, *629*, 522-534. https://doi.org/10.1016/j.jcis.2022.08.180

[200] Mainini, A. G., Poli, T., Paolini, R., Zinzi, M., & Vercesi, L. (2014). Transparent multilayer ETFE panels for building envelope: thermal transmittance evaluation and assessment of optical and solar performance decay due to soiling. *Energy Procedia*, *48*, 1302-1310. https://doi.org/10.1016/j.egypro.2014.02.147

[201] Dimitriadou, E. A., & Shea, A. (2015). Experimental Assessment and Thermal Characterization of Ethylene TetraFluoroEthylene ETFE Foil. *AJTE*, *2*, 25-38. https://doi:10.30958/ajte.2-1-2

[202] Cremers, J., & Marx, H. (2016). Comparative study of a new IR-absorbing film to improve solar shading and thermal comfort for ETFE structures. *Procedia Engineering*, *155*, 113-120. https://doi:10.1016/j.proeng.2016.08.012

PUBLICATIONS

1. **Jaishree**, A. Bhandari, N. Khatri, Y.K. Mishra, M.S. Goyat, Superhydrophobic coatings by the hot embossing approach: recent developments and state-of-art applications, Materials Today Chemistry, Volume 30, 2023, 101553, ISSN 2468-5194, https://doi.org/10.1016/j.mtchem.2023.101553.
2. **Sharma, J.,** Bhandari, A., Khatri, N. *et al.* A brief review of transitional wetting regimes for superhydrophobic surfaces. *J Braz. Soc. Mech. Sci. Eng.* **46**, 273 (2024), (https://doi.org/10.1007/s40430-024-04844-8).
3. **Jaishree,** S., Bhandari, A., Khatri, N. *et al.* Advancement of Analytical Model for Hydrophobic Rectangular Pillared Array on Al-Surface and Its Experimental Validation. *Int. J. Precis. Eng. Manuf.* **25**, 947–958 (2024), (https://doi.org/10.1007/s12541-024-00969-x).

Papers presented in International/National Conferences:

1. **Jaishree**, M.S. Goyat, Anupam Bhandari, "Role of various factors in Single Point Diamond Turning Machining (SPDT) to manufacture superhydrophobic surfaces" at the "International Online Conference on Nanomaterials (ICN-2022)" held at Mahatma Gandhi University, Kottayam, Kerala, India during 12th -14th, August 2022.
2. **Jaishree**, M.S. Goyat, Anupam Bhandari, "Fabrication of micro/nano-sized hierarchical patterns on Cu to create large-scale arrayed superhydrophobic surfaces using ultraprecision machining" at the "International Young Researchers Conclave 2023" held at UPES during January 19-20, 2023.
3. **Jaishree**, M.S. Goyat, Anupam Bhandari, "Micro-textured ETFE for self-cleaning applications" at the "International Young Researchers Conclave 2024" held at UPES during February 28-29, 2024.

Jaishree .

DEVELOPMENT OF MATHEMATICAL MODEL-ASSISTED MICRO/NANO-HIERARCHICAL STRUCTURES ON ETFE FILMS ...

Quick Submit

Quick Submit

University of Petroleum & Energy Studies

Document Details

Submission ID

trn:oid:::1:3243520869

Submission Date

May 8, 2025, 3:24 PM GMT+5:30

Download Date

May 8, 2025, 3:36 PM GMT+5:30

File Name

Thesis-jaishree_for_plag_run.pdf

File Size

5.6 MB

180 Pages

35,881 Words

203,549 Characters

3% Overall Similarity

The combined total of all matches, including overlapping sources, for each database.

Filtered from the Report

- Bibliography
- Quoted Text
- Small Matches (less than 14 words)

Exclusions

- 4 Excluded Sources
- 1 Excluded Match

Match Groups

30 Not Cited or Quoted 2%
Matches with neither in-text citation nor quotation marks

6 Missing Quotations 0%
Matches that are still very similar to source material

0 Missing Citation 0%
Matches that have quotation marks, but no in-text citation

0 Cited and Quoted 0%
Matches with in-text citation present, but no quotation marks

Top Sources

1% Internet sources

1% Publications

1% Submitted works (Student Papers)

Integrity Flags

0 Integrity Flags for Review

No suspicious text manipulations found.

Our system's algorithms look deeply at a document for any inconsistencies that would set it apart from a normal submission. If we notice something strange, we flag it for you to review.

A Flag is not necessarily an indicator of a problem. However, we'd recommend you focus your attention there for further review.

Match Groups

- **30** Not Cited or Quoted 2%
  Matches with neither in-text citation nor quotation marks
- **6** Missing Quotations 0%
  Matches that are still very similar to source material
- **0** Missing Citation 0%
  Matches that have quotation marks, but no in-text citation
- **0** Cited and Quoted 0%
  Matches with in-text citation present, but no quotation marks

Top Sources

1% Internet sources
1% Publications
1% Submitted works (Student Papers)

Top Sources

The sources with the highest number of matches within the submission. Overlapping sources will not be displayed.

1	Internet	
portal.findresearcher.sdu.dk		<1%
2	Publication	
Yuan Chen, Xin-Rui Gao, Hua-Dong Huang, Ling Xu, Xu Ji, Gan-Ji Zhong, Hao Lin, Z...		<1%
3	Publication	
"Advanced Multifunctional Materials from Fibrous Structures", Springer Science a...		<1%
4	Internet	
www.mdpi.com		<1%
5	Student papers	
University of Newcastle		<1%
6	Publication	
Mortazavi, Vahid, and M.M. Khonsari. "On the degradation of superhydrophobic s...		<1%
7	Publication	
Yue Fan, Yao Tan, Yingying Dou, Shilin Huang, Xuelin Tian. "Reducing the contact ...		<1%
8	Internet	
d-nb.info		<1%
9	Publication	
Sujuan Wang, Senbin Xia, Hailong Wang, Ziqiang Yin, Zhanwen Sun. "Prediction o...		<1%
10	Internet	
repositorium.sdum.uminho.pt		<1%

11 Publication

Yadav Narendra Kumar Rajbahadur, Avinash Kumar, Sushant Negi, Simanchal Ka... <1%

12 Student papers

Washington University in St. Louis <1%

13 Publication

Zhiguang Guo, Fuchao Yang. "Surfaces and Interfaces of Biomimetic Superhydro... <1%

14 Publication

Eyal Bittoun, Abraham Marmur. "The Role of Multiscale Roughness in the Lotus Ef... <1%

15 Publication

J. Sharma, A. Bhandari, S. Jangra, M.S. Goyat. " Sol–gel derived highly hydrophobic... <1%

16 Internet

www.researchgate.net <1%

17 Publication

A. Sudeepthi, L. Yeo, A. K. Sen. "Cassie–Wenzel wetting transition on nanostructur... <1%

18 Student papers

College of Haringey, Enfield and North East London <1%

19 Publication

Gene Whyman, Edward Bormashenko. "How to Make the Cassie Wetting State St... <1%

20 Student papers

Hong Kong University of Science and Technology <1%

21 Student papers

La Trobe University <1%

22 Student papers

Queen's University of Belfast <1%

23 Publication

Xiaohua Liu, Ruodong Mo, Kangsen Li, Jun Shen, Jiang Ma, Feng Gong. "Manufact... <1%

24 Internet

dspace.bits-pilani.ac.in:8080 <1%

25 Publication

B. Majhy, V.P. Singh, A.K. Sen. "Understanding wetting dynamics and stability of a... <1%

26 Student papers

Indian Institute of Technology Bhilai <1%

27 Publication

Mangala Joshi. "Nanotechnology in Textiles - Advances and Developments in Poly... <1%

28 Publication

Shivaprakash, Nischay Kodihalli. "Roll-to-Roll Hot Embossing of Microstructures: ... <1%

29 Student papers

Somaiya Vidyavihar <1%

30 Student papers

Universiti Sains Malaysia <1%

31 Internet

thisvsthat.io <1%